



# Development and Study of the Level-1 Trigger System for the ATLAS Experiment at the Large Hadron Collider

Ichimiya, Ryo

---

(Degree)

博士 (理学)

(Date of Degree)

2006-03-25

(Date of Publication)

2012-08-27

(Resource Type)

doctoral thesis

(Report Number)

甲3695

(URL)

<https://hdl.handle.net/20.500.14094/D1003695>

※ 当コンテンツは神戸大学の学術成果です。無断複製・不正使用等を禁じます。著作権法で認められている範囲内で、適切にご利用ください。



博士論文  
Doctoral Dissertation

Development and Study of the Level-1 Trigger System for the  
ATLAS Experiment at the Large Hadron Collider

(LHC 加速器における ATLAS 実験用 Level-1 トリガシステムの開発及びその研究)

Ryo Ichimiya

February, 2006

Graduate School of  
Science and Technology  
Kobe University

## Abstract

The main objectives of the ATLAS Experiment at the Large Hadron Collider are to search for the Higgs boson(s), to verify the Standard Model, to measure Standard Model parameters more precisely and to explore the physics beyond the Standard Model in higher energy range of up to a few TeV. This experiment has to handle tremendous data flow, far more than any experiment have done ever. Therefore extremely powerful trigger system to reduce the event rate efficiently is essential. The ATLAS Trigger system consists of three trigger stages: Level-1 Trigger, Level-2 Trigger and Event Filter. In order to extract interesting physics results efficiently from high luminosity proton-proton interactions in high radiation environment, special architecture and devices are required in the Level-1 Trigger and data acquisition system (TDAQ).

The author developed two key devices for the TDAQ of the ATLAS Endcap muon Trigger system which use detectors called Thin Gap Chamber (TGC). This Trigger system was designed through a physics performance study with Monte Carlo simulation. Furthermore a trigger logic simulator has developed to check the correctness trigger logic system. Due to the space availability and timing consideration, the TGC front-end electronics will be placed on the TGC surface where the radiation level is high ( $\sim 210$  Gy for ten years). The high radiation level causes not only damage to the devices but also limitation of access for maintenance. This situation made the design work for the trigger electronics much more difficult.

We chose and developed Application Specific Integrated Circuit (ASIC) for the front-end core part of the TDAQ. The ASICs are manufactured using the latest technology to have inherently higher radiation tolerance level. It also has favorable characteristics of high-speed data processing, low power consumption, low cost (in mass production) and small area. A lot of efforts were made to develop the ASIC with high enough performance for the ATLAS Experiment.

The Endcap muon Trigger system has flexibility in setting threshold of transverse momentum level to classify incoming muons. This part of function is done at the Sector Logic, the final part of the Endcap muon Trigger system located in electronics hut. We chose to use the latest Field Programmable Gate Array (FPGA) for the Sector Logic. The Sector Logic needs to operate with low latency and needs to have flexibility in setting different threshold level. The author developed the algorithm and made the final prototype of the Sector Logic.

In order to confirm the radiation tolerance of the semiconductor devices used in the Endcap muon Trigger electronics system, we have executed  $\gamma$ -ray and proton beam irradiation tests for these devices.

The ATLAS TDAQ system has been developed and constructed. The ATLAS Experiment is scheduled to start taking data in 2007.

# Acknowledgement

I would like to thank my supervisor Prof. Hiroshi Takeda and Prof. Hisaya Kurashige for their support and guidance over the entire years. I also give my special thanks to Prof. Osamu Sasaki who continuously gave me valuable guidance and support. I would like to express special thanks to Mr. Masahiro Ikeno for technical suggestion and support at the electronics development. I would also like to address special thanks to Prof. Yasuo Arai for technical/theoretical suggestion and support in the development of the ASICs and in the semiconductor irradiation tests. I would like to express thanks to Dr. Hiroyuki Kano for technical support and advice in the ASIC development. I'm very grateful to Dr. Kentaro Mizouchi for co-works in the ASIC development and various discussions with me. I would like to thank to Mr. Takeshi Ogata for co-works for the Sector Logic development. I also would like to express special thanks to Mrs. Yumi Yokoyama for various support of our studies at our laboratory.

I would like to thank to Prof. Takahiko Kondo, Prof. Chikara Fukunaga, Prof. Hiroshi Sakamoto, Dr. Masaya Ishino, Prof. Mitsuaki Nozaki, Prof. Kiyotomo Kawagoe, Dr. Atsuhiko Ochi, Dr. Kazumi Hasuko, Prof. Tokio Kenneth Ohoka, Prof. Hiroyuki Iwasaki and Prof. Tomio Kobayashi for their support and advice.

I would like to give special thanks to Prof. Tohru Takeshita for giving a chance to enter this exciting world of experimental particle physics studies.

I would like to thank all colleagues at Kobe University, at the ATLAS TGC Electronics Group and at the ATLAS collaboration.

Finally, I would like to thank my parents and family for their continuous and tremendous support plus encouragement until now.

# Contents

<b>0</b>	<b>Introduction</b>	<b>9</b>
<b>1</b>	<b>The ATLAS Experiment</b>	<b>12</b>
1.1	The Large Hadron Collider . . . . .	12
1.1.1	The LHC Accelerator Complex . . . . .	12
1.1.2	The Bending (Dipole) Magnets in the LHC . . . . .	14
1.2	Physics at the ATLAS Experiment . . . . .	15
1.2.1	The Standard Model . . . . .	15
1.2.2	Physics Potential . . . . .	16
1.2.3	Higgs Boson . . . . .	17
1.3	The ATLAS Detector . . . . .	19
1.3.1	Overview . . . . .	19
1.3.2	Inner Detector . . . . .	20
1.3.3	Calorimetry . . . . .	20
1.3.3.1	Electromagnetic Calorimeter . . . . .	21
1.3.3.2	Hadronic Calorimeter . . . . .	21
1.3.4	Muon Spectrometer . . . . .	23
1.3.4.1	Monitored Drift Tube (MDT) . . . . .	24
1.3.4.2	Cathode Strip Chamber (CSC) . . . . .	24
1.3.4.3	Resistive Plate Chamber (PRC) . . . . .	25
1.3.4.4	Thin Gap Chamber (TGC) . . . . .	26
<b>2</b>	<b>The ATLAS Trigger/Data-Acquisition (TDAQ) System</b>	<b>28</b>
2.1	Level-1 (LVL1) Trigger Overview . . . . .	30
2.1.1	Muon Trigger . . . . .	31
2.2	Timing, Trigger and Control (TTC) distribution system . . . . .	32
<b>3</b>	<b>The Endcap Muon (TGC) Trigger System</b>	<b>33</b>
3.1	Layout and its Algorithm . . . . .	33
3.2	Implementation on the Electronics System . . . . .	34
3.3	Trigger Sector . . . . .	36

3.4	Latency . . . . .	38
<b>4</b>	<b>System Development Issues</b>	<b>40</b>
4.1	Technology selections for the system components . . . . .	40
4.2	Slave Board ASIC . . . . .	43
4.2.1	Overview . . . . .	43
4.2.2	Master-Slave Structure . . . . .	44
4.2.3	Block Diagram . . . . .	44
4.2.4	Input Block . . . . .	45
4.2.5	Low- $p_T$ trigger Block . . . . .	46
4.2.5.1	Coincidence Matrix for Doublets pair (DSB) . . . . .	47
4.2.5.2	Triplet Slave Board (TSB) . . . . .	50
4.2.5.3	EI/FI Slave Board (EFSB) . . . . .	53
4.2.6	Readout Block . . . . .	55
4.2.7	JTAG Block . . . . .	56
4.2.8	Implementation on the ASIC . . . . .	58
4.2.9	Validation . . . . .	58
4.3	Sector Logic . . . . .	61
4.3.1	Overview . . . . .	61
4.3.2	Design of the Sector Logic . . . . .	61
4.3.2.1	R- $\phi$ coincidence . . . . .	62
4.3.2.2	Track Selection Logic (Pre-Track Selector, Track Selector) . . . . .	63
4.3.2.3	Decoder . . . . .	63
4.3.2.4	Encoder . . . . .	69
4.3.3	The first prototype (Prototype-0) . . . . .	72
4.3.3.1	Specification . . . . .	72
4.3.3.2	Implementaion . . . . .	73
4.3.3.3	Validation . . . . .	74
4.3.3.4	Integration test with the MUCTPI . . . . .	74
4.3.3.5	Test beam at H8 beam line in CERN . . . . .	74
4.3.4	Final Design of whole Sector Logic system . . . . .	75
4.3.4.1	Final Design of Sector Logic board . . . . .	77
4.4	Radiation Tolerance . . . . .	80
4.4.1	Test for Total Ionization Dose (TID) . . . . .	80
4.4.1.1	TID Test Procedure . . . . .	80
4.4.1.2	Results of the TID tests . . . . .	81
4.4.2	Test for Single Event Effect (SEE) . . . . .	86
4.4.2.1	SEE Test Procedure . . . . .	87

4.4.2.2	SEE cross sections for individual chips . . . . .	88
4.4.3	Summary of the irradiation tests . . . . .	89
<b>5</b>	<b>Summary and Conclusions</b>	<b>90</b>
	<b>Reference</b>	<b>92</b>

# List of Figures

1.1	LHC and Injection Complex at CERN. . . . .	13
1.2	Schematic layout of the LHC. Beam 1 circulates clockwise and Beam 2 Counter-Clockwise. . . . .	13
1.3	Cross Section of LHC Tunnel with showing the LHC machine cross section. . .	15
1.4	Feynman-Diagrams for Higgs Boson Production. . . . .	18
1.5	Decay branching fraction of StandardModelHiggs. . . . .	18
1.6	The ATLAS detector overview. . . . .	20
1.7	Inner Detector. . . . .	21
1.8	Layout of the Calorimeters. . . . .	22
1.9	Total thickness (in radiation length) of the ATLAS EM calorimeter as a function of $\eta$ . . . . .	22
1.10	Amount of material (absorption length) in the ATLAS Calorimetry as a function of $\eta$ . . . . .	22
1.11	R-Z View of the ATLAS Muon Spectrometer. . . . .	24
1.12	The MDT (Monitored Drift Tube). . . . .	24
1.13	The CSC (Cathode Strip Tube). . . . .	25
1.14	The RPC (Resistive Plate Chamber). . . . .	25
1.15	TGC structure showing anode wires, graphite cathodes, G-10 layers, and read-out strip orthogonal to the wires. . . . .	26
1.16	Cross-section of a triplet (left) and of a doublet of TGCs (right). . . . .	27
2.1	Schematic diagram of the ATLAS Trigger and DAQ System. . . . .	29
2.2	ATLAS LVL1 Trigger System. . . . .	30
2.3	Layout of the ATLAS Muon Trigger Chambers. . . . .	31
3.1	The Longitudinal view of the TGC system. . . . .	33
3.2	Overview of the TGC LVL1 Trigger electronics system. . . . .	35
3.3	TGC electronics placement. . . . .	37

3.4	TGC LVL1 Trigger segmentation for an octant (one eights of pivot plane). One octant wheel is divided into six ENDCAP sectors and three FORWARD sectors. Bold lines in the figure indicate individual trigger sectors. They are further subdivided into trigger subsectors. . . . .	38
3.5	Wire-signal segmentation. Each small box represents a segment of 32 channels, corresponding to 4 subsectors. . . . .	39
4.1	Voting Logic implementation: Three D-type FlipFlops are used to implement 1bit Voting Register. Even if any one register value flipped, the data out keeps the initial value. . . . .	41
4.2	Device selection at the TGC electronics system. . . . .	42
4.3	Layout Mask pattern of SLB ASIC Version 6. This version is final design and mass-production has done with this design. . . . .	43
4.4	Normal Shift Register. . . . .	44
4.5	Master-Slave Shift Register. . . . .	44
4.6	Block Diagram of the SLB ASIC. . . . .	45
4.7	Double mask scheme implemented in the SLB ASIC, two masks are shown in the (red) solid squares. One is common for the Readout and the Matrix, and the other one is only for the trigger matrix. . . . .	46
4.8	Schematic of Delay Circuit of SLB ASIC Input block. At first, the input signal is latched either on Positive edge (D-FF) or Negative edge (DN-FF). Following delay shift register circuit is formed by the Master-Slave structure. . . . .	46
4.9	The functional structure of a Slave Board for the TGC doublet pairs. Shown is the wire Slave Board; the strip Slave Board has 16-bit output instead. . . . .	47
4.10	Structure of a 3-out-of-4 Doublet Slave Board Low- $p_T$ matrix and the encoded output information. The wire (r) Slave Board is shown. The strip Doublet Slave Board is similar, but with $\Delta\phi = \pm 3$ . . . . .	48
4.11	Detailed structure of the 3-out-of-4 Low- $p_T$ matrix for wires. Also shown is the function of a matrix element. Cells with the same shading have the same $\Delta r$ . The matrix for $\phi$ is the same, except $\Delta\phi$ goes from -3 to +3. (Actually X and Y in the figure are the same.) . . . . .	49
4.12	Declustering rules. When a hit pattern wider than two is found, the rules shown assign a position to the track. . . . .	50
4.13	Slave Board for TGC Triplets (for wire signals). . . . .	51
4.14	Structure of the Triplet logic for wire signals. Logic to deal with the staggering of triplet layers and the output format after encoding is also shown. . . . .	51

4.15	Functional structure of a Slave Board for TGC Triplet strip signals. There are only two active layers of strips per “triplet”. One chip handles up to two triplet units independently. . . . .	52
4.16	The functional structure of the triplet Slave Board for strip signals. Logic to deal with the staggering of triplet layers and output format after the encoder section is also shown. . . . .	53
4.17	Slave Board for the EI/FI TGC doublet. . . . .	54
4.18	The functional structure of the EI/FI Slave Board. Logic to deal with the staggering of doublet layers and output format after the encoder section is also shown. . . . .	54
4.19	Block Diagram of the SLB Readout Block. . . . .	55
4.20	Layout of the Readout macro-core. In this figure, alligned rectangles means the location of the memory macro cells. . . . .	56
4.21	A Schematic View of SLB ASIC Test Setup. . . . .	59
4.22	Various SLB Test Vectors and Results. . . . .	60
4.23	Block Diagram of Sector Logic (trigger logic functional view). . . . .	62
4.24	Detail of Sub Sector Cluster (SSC) for the R- $\phi$ coincidence togther with hit inputs. . . . .	63
4.25	A schematic of Track Selection logic block. . . . .	64
4.26	Data Format from Hi-p <sub>T</sub> ASIC chip (Wire mode). . . . .	64
4.27	Wire High-p <sub>T</sub> Boards coverage and its correspondant SSCs. . . . .	65
4.28	Wire (R) input signal from from Wire High-p <sub>T</sub> Board. . . . .	66
4.29	Strip ( $\phi$ ) input signal from from Strip High-p <sub>T</sub> Board. . . . .	67
4.30	A Photograph of TGC Sector Logic Prototype-0 (top view). . . . .	72
4.31	Block Diagram of Sector Logic Prototype-0 (FORWARD Region type). . . . .	73
4.32	Correlation plots of p <sub>T</sub> levels (left) and ROI location(right) for trigger words read out by Sector Logic vs MUCTPI. . . . .	75
4.33	The Sector Logic system. . . . .	76
4.34	The layout of TGC FORWARD Sector Logic (top view). . . . .	79
4.35	The layout of TGC ENDCAP Sector Logic (top view). . . . .	79
4.36	$\gamma$ -ray irradiation test setup. . . . .	81
4.37	VCON voltages of PP ASIC for $\gamma$ -ray irradiation. . . . .	82
4.38	Frequencies of Ring Oscillator on Rohm 0.35 $\mu$ m for $\gamma$ -ray irradiation. . . . .	82
4.39	Consumption current of A54SX32A for $\gamma$ -ray irradiation. . . . .	84
4.40	Frequencies of Ring Oscillator on A54SX32A for $\gamma$ -ray irradiation. . . . .	84
4.41	Consumption current of AX250 for $\gamma$ -ray irradiation. (1 krad = 10 Gy) . . . . .	85
4.42	Frequencies of Ring Oscillator on AX250 for $\gamma$ -ray irradiation. (1 krad = 10 Gy) . . . . .	85
4.43	Schematic of proton beam test setup. . . . .	87
4.44	Picture of proton beam test setup. . . . .	88

# List of Tables

1.1	Parameters of the LHC. . . . .	14
1.2	Main Parameters of the dipole magnet. . . . .	14
1.3	Fundamental Forces and their Bosons. . . . .	16
3.1	contributions to the total estimated TGC latency, in bunch-crossing in number of bunch crossing. (BC) (1 BC = 25 ns) . . . . .	39
4.1	Control Registers in SLB ASIC. . . . .	57
4.2	Data format between Sector Logic and MUCTPI [16]. . . . .	70
4.3	Compilation of the SEE test results. . . . .	89

# Chapter 0

## Introduction

The Standard Model (SM) is a very successful model in describing interactions of the matter components, applicable to very small scale and high energies. Past experiments, performed with the Large Electron Positron collider (LEP), have confirmed the validity of the SM up to the energy of about 200 GeV. However, there still are questions to be answered in the SM framework such as the existence of the Higgs boson. The next generation collider, where protons are chosen as the beam particles, is now being built in the LEP tunnel at CERN. Since the synchrotron radiation is not a serious problem for proton beams at this energy level, the collider, named as “the Large Hadron Collider” (LHC), can accelerate the beams up to 7 TeV. The collider offers a large range of physics opportunities and provides the potential to make tests of the model with the highest energy and to search for signature of physics beyond the Standard Model.

Since most of the physics questions involve interactions that has very low cross section, not only the high energy but also the highest possible luminosity is required. The LHC will reach a luminosity of  $10^{34} \text{ cm}^{-2}\text{s}^{-1}$ , with inter-bunch crossing time of 25 ns and more than  $\sim 10^9$  interactions per second are expected.

ATLAS Experiment is one of the general purpose experiments scheduled to start taking data at the LHC in 2007. A lot of work is currently underway to complete the ATLAS detector system. In addition, detailed simulation works are performed in order to estimate the sensitivity of the ATLAS Experiment to various interesting physics processes. This thesis is devoted to developments and studies of electronics systems mostly for the Level-1 Trigger of the ATLAS Experiment.

The ATLAS Trigger and data-acquisition system is an essential part to reduce the data from the initial interaction rate  $\sim 10^9 \text{ Hz}$  to  $\sim 200 \text{ Hz}$  for the permanent storage. Since this requires an overall rejection factor of  $10^7$  against “minimum-bias” or QCD processes, an extremely excellent trigger system, essential for rare new physics such as Higgs boson decays, is required. This requirement is by far the most difficult one compared with any other experiments in the past. There are many technical difficulties needed to be overcome in producing the ATLAS Trigger system.

The Level-1 (LVL1) Trigger system locates at the front-end part of the ATLAS Trigger system and must be operated in synchronous with 40.08 MHz LHC clock. The LVL1 Trigger makes an initial selection to reduce the rate into 100 kHz, based on reduced-granularity information from the calorimeters and muon detectors.

An essential requirement on the LVL1 Trigger is that it should uniquely identify the bunch crossing of the interest event(s) occurred. Given the short bunch crossing interval, this is a non-trivial consideration. In the case of the muon Trigger, the physical size of the muon spectrometer implies times-of-flight comparable to the bunch crossing period.

It is also important to keep the latency (time taken to form and distribute the trigger decision) to a minimum. During this waiting time all signals in detector channels has to be retained in “pipeline” memories. These memories are generally contained in custom integrated circuits, placed on or close to the detector, usually in inaccessible area and under a high-radiation environment. For reasons of cost and reliability, it is desirable to keep the pipeline lengths as short as possible. The LVL1 latency, measured from the time of the proton-proton collision until the trigger decision is made available to the front-end electronics, is required to be less than  $2.5 \mu\text{s}$ . In order to achieve this, the LVL1 Trigger is implemented as a system of dedicated hardware processors.

For today’s electronics, the system clock of 40.08 MHz is relatively slow. Many CPUs operates over a GHz. This high frequency operation is achieved not only by the latest device technologies but also by the long length pipeline architecture, where each step in the pipeline has minimized logics. (i.e. This aims lowest latency in each step.) This is a straightforward way to achieve the high performance in the viewpoint of data throughput.<sup>1</sup>

On the other hand, the LVL1 Trigger system is required to minimize the latency.<sup>2</sup> In addition, due to the trigger logic of our system needs to cover large geometrical area of which signals are correlated each other, one unit trigger logic has large number of input channels. From the viewpoint of implementation, each step of the pipeline should process these signals all together, so that breakdown of these processes into smaller steps might be limited. Therefore, we have to implement large-scale logics into steps synchronized with the system clock of 40.08 MHz with sufficient timing margin. To meet this requirement, technical challenges were needed to develop the logic design.

The author made efforts to finalize the one of front-end core components implementing Application Specific Integrated Circuit (ASIC), named Slave Board (SLB) ASIC, which makes both trigger decisions and data read out by using “pipeline” memories. The ASIC is manufactured with a full custom  $0.35 \mu\text{m}$  CMOS technology in  $9.86 \text{ mm} \times 9.86 \text{ mm}$  die size. The ASIC has over  $2 \times 10^5$  gates. To equip enough performance and reliability, various techniques were developed in both logic implementations and gate layouting in the die.

---

<sup>1</sup>Throughput is the amount of data processed in a unit time.

<sup>2</sup>In general, latency and throughput are in the relation of tradeoff.

The Sector Logic, which is the final part of the Endcap muon Trigger system, combines two-dimensional muon track information and finds muons with high transverse momentum. From the physics requirements, the Sector Logic should have wide flexibility of muon selection criteria of changing  $p_T$  threshold at any value. The author has developed the Sector Logic by using Field Programmable Gate Array (FPGA) devices with Look-Up Table (LUT) method.

From the viewpoint of minimization of latency for the LVL1 Trigger system, many components are needed to install near the detector as far as possible, where the radiation level is considerable high. Devices robust against such a hard radiation environment of ten years of ATLAS Experiment were chosen for our system. Devices should not be fatally damaged against total ionization doze (TID) and should be strong against large ionization event by energetic hadrons ( $>20$  MeV) (Single Event Effect (SEE)). In order to confirm the radiation tolerance of these devices, we have executed irradiation tests ( $\gamma$ -ray for TID effects, proton beam for SEE effects).

In this thesis, following issues are mainly discussed:

1. Architecture and its implementation of the Level-1 Trigger, especially Endcap muon Trigger (Thin Gap Chamber (TGC) Trigger),
2. Functions of Slave Board (SLB) ASIC for the Endcap muon Trigger system and its development,
3. Sector Logic functions and its development,
4. Irradiation tests for the semiconductor devices used in the system.

This thesis is organized as follows: In Chapter 1, overview of the LHC and ATLAS Experiment and its subsystem are described. In Chapter 2, the design of the ATLAS Trigger/DAQ (TDAQ) system is described. In Chapter 3, the design of the Endcap (TGC) muon Trigger system is described. Chapter 4 is the main part of this thesis and is devoted for both the discussions on (1) technology selection and radiation tolerance test, and (2) the detailed design and its specification of the components that the author developed. In Chapter 5, discussion and summary of the study are described.

# Chapter 1

## The ATLAS Experiment

### 1.1 The Large Hadron Collider

The Large Hadron Collider (LHC) is the latest proton-proton collider being built at CERN, which will provide a center of mass energy of  $\sqrt{s} = 14$  TeV with a design luminosity of  $L = 10^{34} \text{ cm}^{-2}\text{s}^{-1}$ . The beam crossing will occur at every 25 ns and, in each crossing, about 23 interactions are expected on average. For the first three years, it will be operated with a lower luminosity of  $L = 10^{33} \text{ cm}^{-2}\text{s}^{-1}$  (denoted as “Low-Lumi.”), then the luminosity will be increased to the design value (“High-Lumi.”). The details are summarized in Table 1.1. The LHC offers a wide range of physics opportunities. The primary goal of the ATLAS project is to discover the origin of particle masses at the electroweak scale. In addition, there are several important goals such as the searches for heavy W- and Z-like objects, supersymmetric particles, compositeness of the fundamental fermions, as well as the investigation of CP violation in B-decays, and detailed studies of the top quark.

#### 1.1.1 The LHC Accelerator Complex

The LHC, whose construction was approved in 1994, will be operational in 2007. It will be accommodated in the LEP tunnel. The existing accelerator complex, which consists of the 50 MeV linac, the 1 GeV booster, the 26 GeV Proton Synchrotron (PS) and 450 GeV Super Proton Synchrotron (SPS), will be employed as the injection system for the LHC as shown in Figure 1.1. The LHC is also designed to be used for heavy ion collisions and reaches for lead ions a center of mass energy of up to  $\sqrt{s} = 1312$  TeV.

As shown in Figure 1.2, four experiments are proposed and being constructed. Two experiments (ATLAS [1] and CMS) are for general purpose, one (ALICE) for heavy ion experiment and one (LHCb) for b-physics experiment. One additional experiment (TOTEM), which hosts on CMS, is an experiment to measure the total cross section, elastic scattering and diffractive processes at the LHC.



Table 1.1: Parameters of the LHC.

Parameter	Normal (High-Lumi.)	Low-Lumi.	Ultimate	Unit
Circumference	27			km
Proton Energy	7.0	←	←	TeV
# of Protons/Bunch	1.1	0.17	1.67	$10^{11}$
# of Bunch	2835	←	←	
Bunch Spacing	25	←	←	ns
Current	0.56	0.087	0.850	A
Trans. emittance	3.75	1.0	3.75	$\mu\text{rad}$
Beam size at IP	16	←	←	$\mu\text{rad}$
Crossing Angle	300	←	←	$\mu\text{rad}$
Luminosity	1.0	0.1	2.3	$10^{34}\text{cm}^{-2}\text{s}^{-1}$
Life Time	10	←	←	Hour
Filling Time	3	←	←	Min

Table 1.2: Main Parameters of the dipole magnet.

Operational field	8.33 T
Coil Aperture at 293K	56.00 mm
Distance between aperture axes at 1.9K	194.00 mm
Magnetic length at 1.9K and at normal field	14312 mm
Current at normal field	11850 A
Operating Temperature	1.9 K

### 1.1.2 The Bending (Dipole) Magnets in the LHC

In order to realize the highest beam energy with the given ring circumference, and also considering spatial limitation of the tunnel, superconducting dipole magnets [2], made with a special technique, are employed in the LHC beam bending system. Due to the space constraint, (See Figure 1.3) the magnet has two beam pipes for counter-rotating proton beams and provides an anti-parallel magnetic field of 8.33 T for them. To realize such strong magnetic field, copper-clad niobium-titanium windings are employed and they are operated under a temperature of 1.9 K with liquid helium. The parameters are summarized in Table 1.2. A total of 1,232 main dipole magnets will be installed in the ARC area, (see Figure 1.2) where the number is maximized to achieve the highest energy. The cryogenics system for the magnets will contain about 700 kl of liquid helium and have a power consumption of about 140 kW.

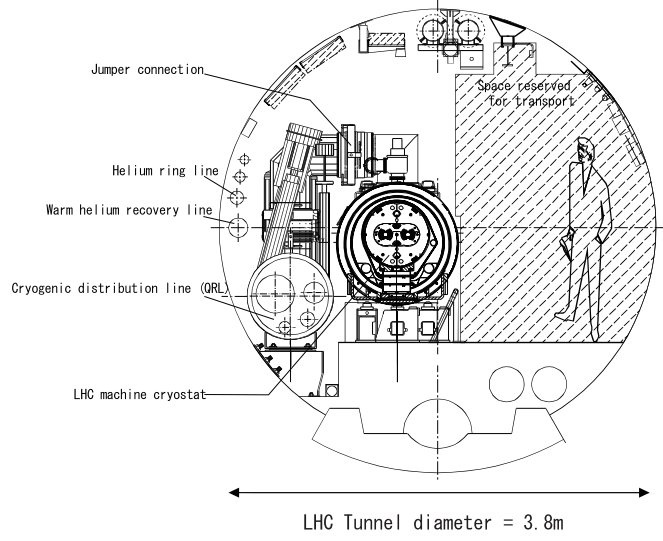


Figure 1.3: Cross Section of LHC Tunnel with showing the LHC machine cross section.

## 1.2 Physics at the ATLAS Experiment

The ATLAS Experiment is designed to try to reveal the mechanism of electroweak symmetry breaking and to study a variety of other physics which would appear at the TeV scale. In particular, a Higgs boson, which is predicted in the Standard Model (SM), is able to be observed in various decay channels over the full range of allowed mass region, if it exists. The ATLAS Experiment can determine the Higgs mass and its couplings.

### 1.2.1 The Standard Model

The Standard Model (SM) is a very successful description of the interactions of the components of matter at the smallest scales ( $< 10^{-18}\text{m}$ ) and highest energies ( $\sim 200\text{GeV}$ ) accessible to current experiments. It is constituted of a quantum field theory that describes the interaction of spin- $\frac{1}{2}$ , point-like fermions, whose interactions are mediated by spin-1 gauge bosons.

The fermions consist of two groups: the leptons and the quarks. The leptons interact weakly and electromagnetically (charged leptons only) and fall into three families,

$$\begin{pmatrix} e \\ \nu_e \end{pmatrix} \begin{pmatrix} \mu \\ \nu_\mu \end{pmatrix} \begin{pmatrix} \tau \\ \nu_\tau \end{pmatrix}$$

The quarks interact electromagnetically, weakly and strongly and fall into three families,

$$\begin{pmatrix} u \\ d \end{pmatrix} \begin{pmatrix} c \\ s \end{pmatrix} \begin{pmatrix} t \\ b \end{pmatrix}$$

Both the leptons and quarks have their own anti-particles. All mesons and baryons are composed of the quarks and anti-quarks.

Table 1.3: Fundamental Forces and their Bosons.

Forces	Boson	Symbol	Relative Strength
weak	intermediate vector bosons	$W^\pm, Z^0$	$\alpha_{\text{weak}} = 1.02 \times 10^{-5}$
electromagnetic	photon	$\gamma$	$\alpha_{\text{em}} = 1/137$
strong	gluons	$g$	$\alpha_{\text{strong}} \approx 0.1$

There are three fundamental forces; the electromagnetic, weak and strong forces.<sup>1</sup> They are described by means of gauge theories and the forces are mediated by one or more boson(s). They are summarized in Table 1.3.

In order to explain the spontaneous symmetry breaking in the electroweak sector, Higgs mechanism, which provides masses to the W and Z bosons, has been introduced. The mechanism employs a spin-less particle called “the Higgs boson” in its minimal formulation. This particle can also provide the masses of all the fermions in the SM.

### 1.2.2 Physics Potential

From an estimated non-diffractive cross-section of  $\sim 100$  mb [1], an average of 23 events are expected per bunch crossing at the peak luminosity. They are mainly from QCD soft collision processes, involving small momentum transfer, with spectator quarks. The events, which are collected with the minimum-bias trigger, can be used to study the topological shapes and energy flows of the events as a test of QCD. Jet cross-sections can be also investigated over several orders of magnitude. More interesting events, such as a Higgs boson is produced, are several orders of magnitude ( $10^{-13}$ ) less frequent. Among the various important physics [3], the followings can be exploited in the ATLAS Experiment [1] :

- Higgs Boson:

One of the most important issues in the ATLAS Experiment is an approach to the origin of the spontaneous symmetry breaking in the electroweak sector in the SM and to understand the origin of particle masses. The LHC has a capability of the Higgs boson production for wide range of its mass ( $m_H$ ) from  $m_H \approx 80$  GeV up to  $m_H \approx 1$  TeV.

- Top Quark:

The LHC is a top quark factory. It produces roughly  $10^7 t\bar{t}$  pairs per year even at the moderate luminosity of  $10^{33} \text{ cm}^{-2}\text{s}^{-1}$  (at low luminosity). The mass of the top quark can be measured with an accuracy of about  $\pm 2\text{GeV}$  at a mass of  $m_t \approx 170$  GeV.

- B-Physics:

In the ATLAS Experiment, a large number of B mesons are available for the studies of the B-physics. The main purposes of the studies are precise measurements of CP violation

---

<sup>1</sup>Gravitational force is not considered in this context.

in the b-quark system ( $B_d^0$ ) and the determination of the angles of the unitary triangle derived from the unitarity of the Cabibbo-Kobayashi-Maskawa matrix. In addition, it is also possible to measure  $B_s\bar{B}_s$  mixing and to search for rare decays such as  $B \rightarrow \mu\mu$ .

- Supersymmetric particles:

Supersymmetric extensions of the SM predict a wide spectrum of new particles with masses and production rates such that at the LHC they could be discovered over a large fraction of the parameter space. Events with a high jet multiplicity and large missing energy make a search possible in the range of 1 to 4 TeV.

- Physics beyond the SM:

While the existing precision electroweak measurements are consistent with a light Higgs boson, the possibility of electroweak symmetry breaking by new strong dynamics at the TeV scale cannot be excluded. The following searches and measurements are proposed:

- Strongly interacting W's.
- Technicolor.
- Compositeness.
- New Gauge Bosons.
- Extra Dimensions.
- Anomalous Gauge-boson Couplings.

### 1.2.3 Higgs Boson

The search for the Higgs boson is the most prominent issue for the LHC. It is used to optimize the ATLAS detector geometry and is given here as an example of the physics potential. The current limit on the Higgs mass from experiments at LEP [11] is  $m_H > 113.5\text{GeV}$ .

The Feynman-diagrams for Higgs boson production are shown in Figure 1.4. Over the mass range of  $80\text{GeV} < m_H < 800\text{GeV}$  the gluon fusion (a) is dominant. The process (b)  $q\bar{q} \rightarrow q\bar{q}H$  becomes dominant for higher masses up to 1 TeV.

The decay branching fraction of standard model Higgs boson is shown in Figure 1.5. The search strategy for the Higgs boson depend on its mass and several methods have to be combined to cover the full mass range:

- $H \rightarrow b\bar{b}$ :

With a Higgs boson mass below the threshold for decays into a pair of vector bosons, this decay mode is essentially 100%. The signature used will be a lepton from one b-quark and a b-quark jet from the other, possibly used with the associated production (Figure 1.4 (c) and (d)). This channel is sensitive at  $80\text{GeV} < m_H < 100\text{GeV}$ .

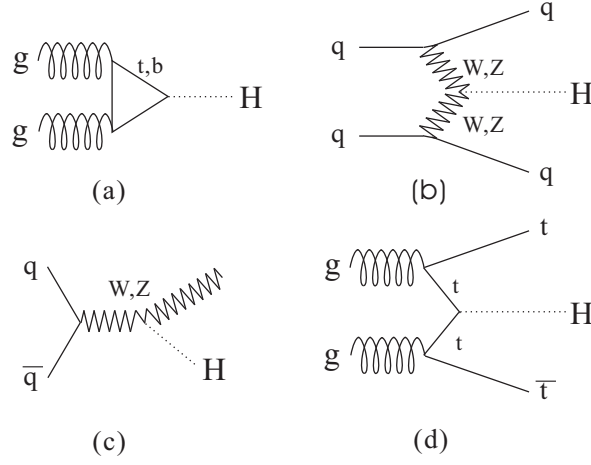


Figure 1.4: Feynman-Diagrams for Higgs Boson Production.

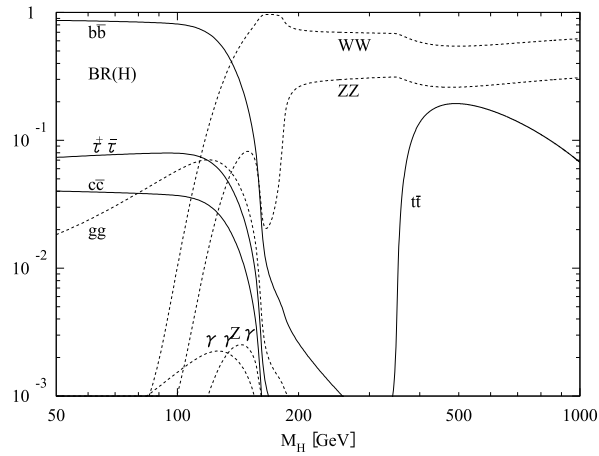


Figure 1.5: Decay branching fraction of StandardModelHiggs.

- $H \rightarrow \gamma\gamma$  :

This is a sensitive channel for  $90\text{GeV} < m_H < 150\text{GeV}$  and requires an excellent electromagnetic calorimeter and identification of photons against a huge background from jets misidentified as photons.

- $H \rightarrow ZZ^{(*)} \rightarrow 4l^\pm$  :

For masses between  $130\text{GeV} < m_H < 2m_Z$ , one of the Z bosons is virtual and the Higgs boson is rather narrow with a large background from boson pair production. For masses  $m_H > 2m_Z$ , both bosons are real and the signal is rather clean.

- $H \rightarrow WW, ZZ \rightarrow l^\pm \nu jj, 2l^\pm jj$  :

These signatures are important in the mass range up to  $m_H \approx 1\text{TeV}$  and uses two jets for identification.

## 1.3 The ATLAS Detector

ATLAS [3] is a general-purpose proton-proton collider detector, which is being constructed for LHC. It is designed to exploit the full discovery potential of the LHC. At the high luminosity, integrated luminosity amounts  $100\text{fb}^{-1}$  per year. Detectors and front-end electronics are firmly required to be radiation tolerance for these high luminosities.<sup>2</sup> Furthermore, bunches of proton are separated by only 25 ns, then high speed operations and low dead time of response are strongly demanded on the detectors. In particular, the very first section of the ATLAS Trigger system (LVL1 Trigger) is required to have low latency and no dead-time for its operation, which will be discussed in the Chapter 2.

### 1.3.1 Overview

The ATLAS detector is illustrated in Figure 1.6, and it measures 22 m high, 44 m long, and weighs 7,000 tons. The characteristics of the ATLAS detector are summarized as follows:

- Precision inner tracking system (denoted as “Inner Detector”) is constituted with pixel, strip of silicon, and TRT with 2 T solenoidal magnet. Good performance is expected on the  $B$ -tagging and the  $\gamma$ -conversion tagging.
- A very good electromagnetic calorimeter is mounted to identify and measure electrons and photons.
- $4\pi$ -covered hadronic calorimeter for hermetic jet measurement and missing transverse energy.
- A stand-alone muon spectrometer with toroidal magnets to identify muons and measure their momentum.

---

<sup>2</sup>This issue is discussed in the section 4.4.

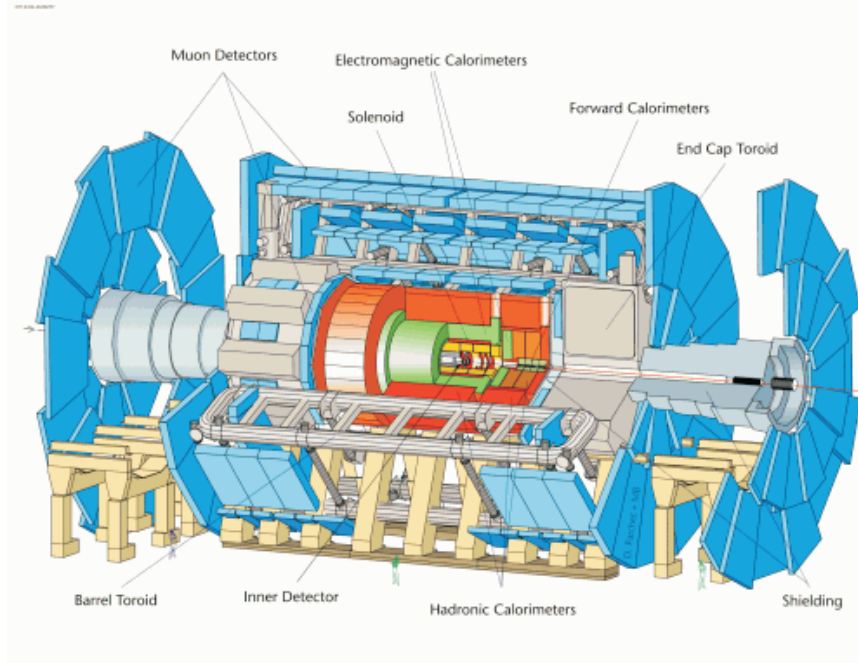


Figure 1.6: The ATLAS detector overview.

### 1.3.2 Inner Detector

The inner detector is in an axial central field of 2 T provided by a superconducting solenoidal magnet and measures the paths of electrically charged particles. The inner detector system consists of following detectors:

- The pixel detector is based on silicon detectors which contain an array of pixel diodes. The size of pixel is  $50 \mu\text{m} \times 400 \mu\text{m}$ .
- The SemiConductor Tracker (SCT) uses strip detectors with fine granularity in the  $\phi$  direction. Silicon is foreseen in the barrel region and GaAs substrates in the forward region where the radiation doses are higher.
- The Transition Radiation Tracker (TRT) is based on straw tubes of 4mm diameter. The straws are interleaved with polyethylene radiators to produce and detect X-ray emission from very relativistic particles.

### 1.3.3 Calorimetry

The ATLAS detector has, like most colliding-beam high-energy beam experiments, two types of calorimeters: an electromagnetic calorimeter situated directly outside of the solenoid magnet of the inner detector, and a hadronic calorimeter is surrounding the electromagnetic one. (Shown in Figure 1.8.) Accurate jet energy measurement and excellent missing energy reconstruction

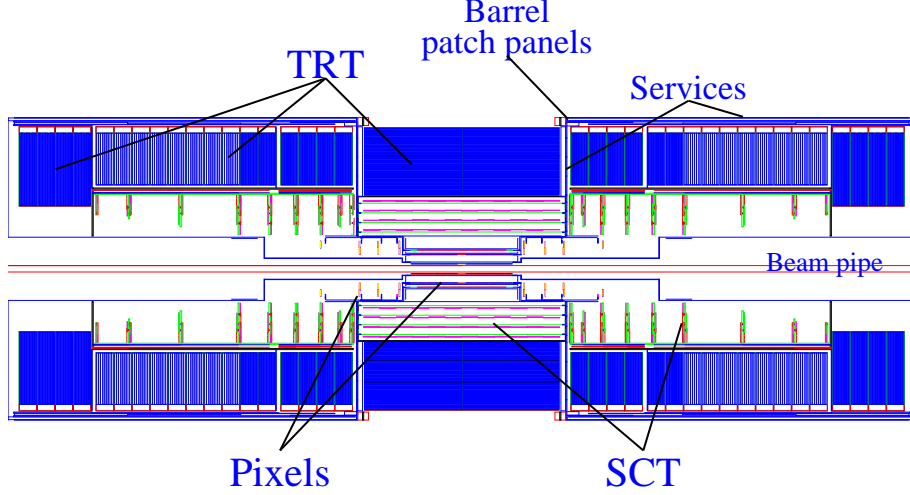


Figure 1.7: Inner Detector.

requirements demand large rapidity coverage. The ATLAS calorimeters therefore extend up to  $|\eta| = 4.9$ .

#### 1.3.3.1 Electromagnetic Calorimeter

The electromagnetic (EM) calorimeter is a lead-liquid argon detector with accordion-shaped Kapton electrodes and lead absorber plates over its full coverage. The accordion geometry provides complete  $\phi$  symmetry without azimuthal cracks. The lead thickness in the absorber plates has been chosen as a function of rapidity, so as to optimize the calorimeter performance in terms of energy resolution.

The total thickness of the EM calorimeter, which is shown in Figure 1.9 as a function of rapidity, is above 24 radiation length( $X_0$ ) in the barrel and above 26  $X_0$  in the end-caps. The EM calorimeter is segmented into square towers of size  $\Delta\eta \times \Delta\phi = 0.025 \times 0.025$  ( $\sim 4 \times 4\text{cm}^2$ ) at  $\eta = 0$ . The electromagnetic calorimeter is designed to keep the energy resolution at the level of  $\sim 10\%/\sqrt{E(\text{GeV})}$  or below.

#### 1.3.3.2 Hadronic Calorimeter

The ATLAS hadronic calorimeter covers the range  $|\eta| < 5$  using different techniques and devices as best suited for the different requirements and radiation environment. In the range  $|\eta| < 1.6$  the iron-scintillating-tiles technique is used for the barrel and extended barrel Tile calorimeters and for partially instrumenting the crack between them with the Intermediate Tile calorimeter (ITC). This gap provides space for cables and services from the innermost detectors. In the range  $\sim 1.5 < |\eta| < 4.9$  the liquid argon calorimeter takes over: the end-cap hadronic calorimeter extends till  $|\eta| < 3.2$  while the range  $3.2 < |\eta| < 4.9$  is covered by the high-density forward calorimeter.

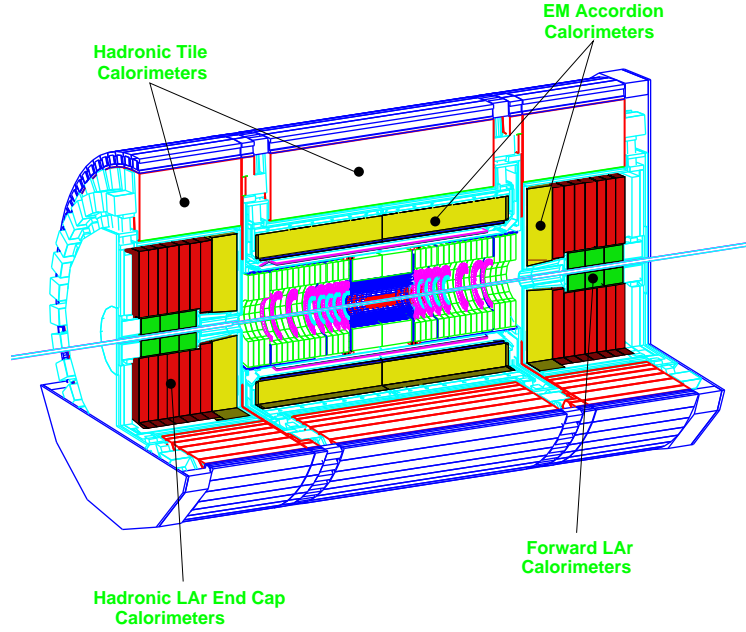


Figure 1.8: Layout of the Calorimeters.

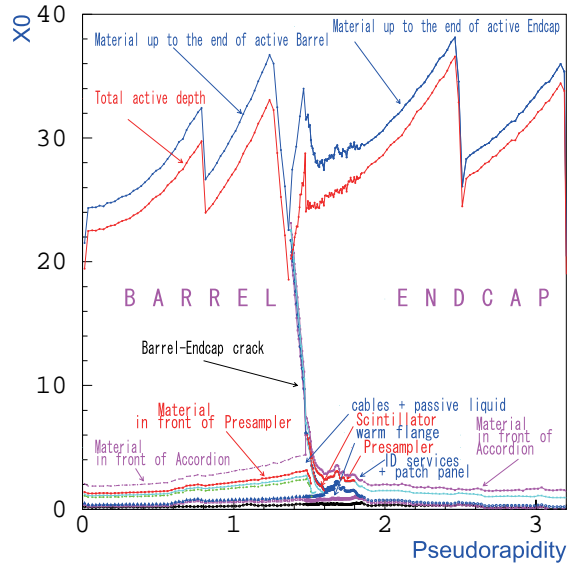


Figure 1.9: Total thickness (in radiation length) of the ATLAS EM calorimeter as a function of  $\eta$ .

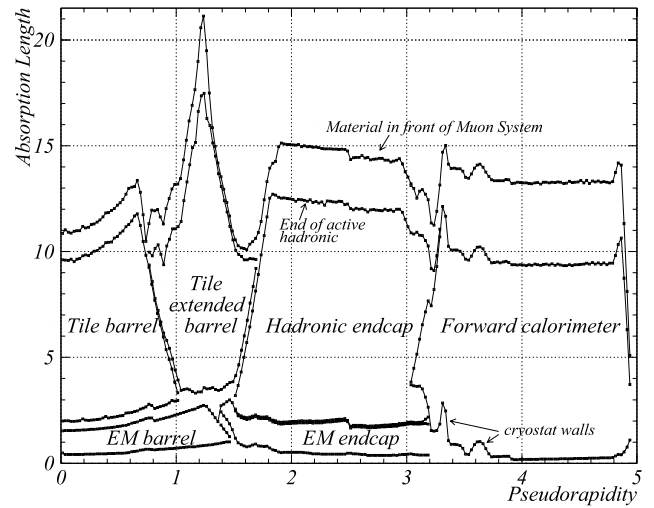


Figure 1.10: Amount of material (absorption length) in the ATLAS Calorimetry as a function of  $\eta$ .

The total thickness is 11 interaction lengths ( $\lambda$ ) at  $\eta = 0$ , including  $1.5\lambda$  of the outer support, sufficient to reduce the punch-through below the irreducible level of prompt or decay muons. Figure 1.10 shows the amount material in the ATLAS calorimetry as a function of  $\eta$  (including EM calorimeter). Together with the large  $\eta$  coverage this thickness will guarantee a good  $E_T^{\text{miss}}$  measurement important in many physics signatures and in particular for SUSY particle searches.

The most stringent transverse granularity requirement comes from the  $W \rightarrow \text{jet-jet}$  decay at high- $p_T$  and applies for  $|\eta| < 3$  (barrel and end-cap), where a granularity  $\Delta\eta \times \Delta\phi = 0.1 \times 0.1$  is needed. At these regions, the required energy resolution criteria are:

$$\frac{\Delta E}{E} = \frac{50\%}{\sqrt{E}} \oplus 10\%.$$

This resolution is adequate to the tasks of providing jet reconstruction and jet-jet mass reconstruction as well as missing  $p_T$  measurement for physics process of interest.

In ATLAS the forward calorimeter ( $|\eta| > 3$ ) is integrated in the end-cap cryostat, with the front face at about 5 meters from the interaction point; this provides a clear benefit in terms of uniformity of coverage, reducing to the minimal possible level the effects of the crack and dead space in the transition region around  $\eta = 3.1$ , with advantages for the efficiency of forward jet tagging and for the reduction of the tails in the  $E_T^{\text{miss}}$  distribution. For this forward calorimeter, a granularity  $\Delta\eta \times \Delta\phi = 0.2 \times 0.2$  is sufficient and required energy resolution criterion is:

$$\frac{\Delta E_T}{E_T} = \frac{100\%}{\sqrt{E}} \oplus 10\%.$$

### 1.3.4 Muon Spectrometer

The ATLAS muon spectrometer is based on a superconducting air-core toroid magnet system, producing an average magnetic field of 0.5T, which consists of a 26 m long barrel part with an inner bore of 9.4 m and an outer radius of 19.5 m and two end-caps with lengths of 5.6 m and inner bores of 1.26 m. Each toroid consists of eight flat coils symmetrically arranged around the beam axis with the end-caps rotated with respect to the barrel so that the coils interleave.

Muon chamber planes are attached to the toroids to measure the trajectories of muons. In the barrel the layout consists of three layers of chambers and in the end-caps the chambers are placed on the front and back faces of the cryostats. A third layer is fixed on the cavern wall. Two types of chambers are used for the high-precision measurements: Monitored Drift Tube chambers (MDT) and Cathode Strip Chambers (CSC).

The high-precision measurements are complemented with chambers for triggering. There are also two types used for this: Resistive Plate Chambers (RPC) and Thin Gap Chambers (TGC).

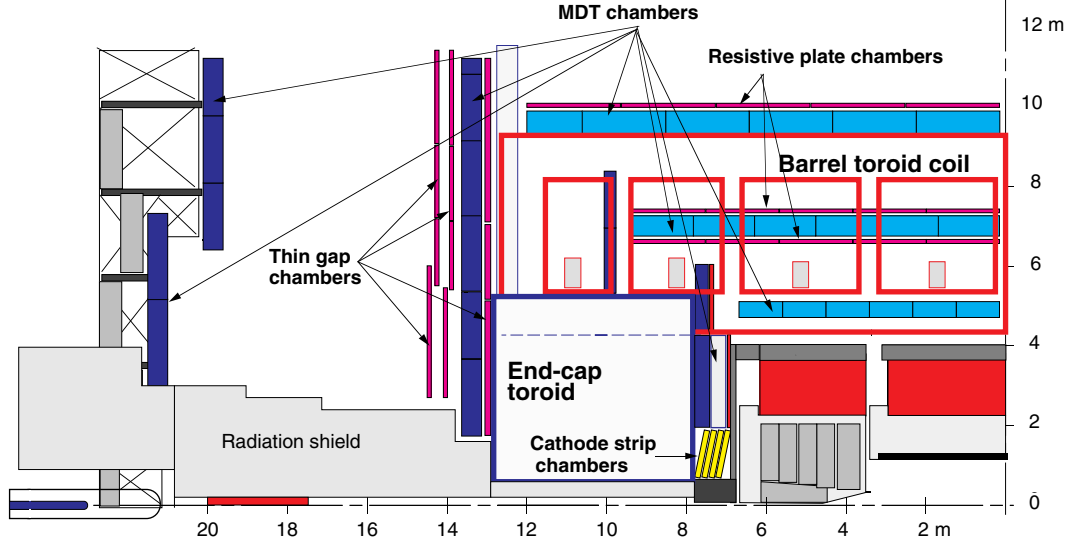


Figure 1.11: R-Z View of the ATLAS Muon Spectrometer.

#### 1.3.4.1 Monitored Drift Tube (MDT)

The Monitored Drift Tube chamber (MDT) consists of multi-layers of drift tubes with a diameter of 30 mm as shown in Figure 1.12. The MDTs use non-flammable Ar(93%)/CO<sub>2</sub>(7%) gas at 3 atm. Maximum drift time is 500 ns and position resolution is 80  $\mu\text{m}$ .

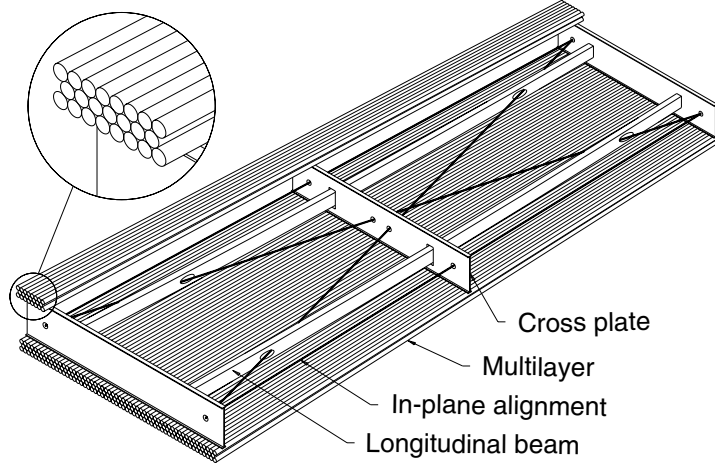


Figure 1.12: The MDT (Monitored Drift Tube).

#### 1.3.4.2 Cathode Strip Chamber (CSC)

The Cathode Strip Chamber (CSC) is a multi-wire proportional chamber (MWPC) with a symmetric cell in which the anode-cathode spacing is equal to the anode wire pitch, which has been fixed at 2.54 mm. (Figure 1.13) In a CSC the precision coordinate is obtained by measuring the charge induced on the segmented cathode by the avalanche formed on the anode

wire. The CSCs can be operated in highest rate environment at large  $\eta$  using an appropriate segmentation. (cf. Figure 1.11)

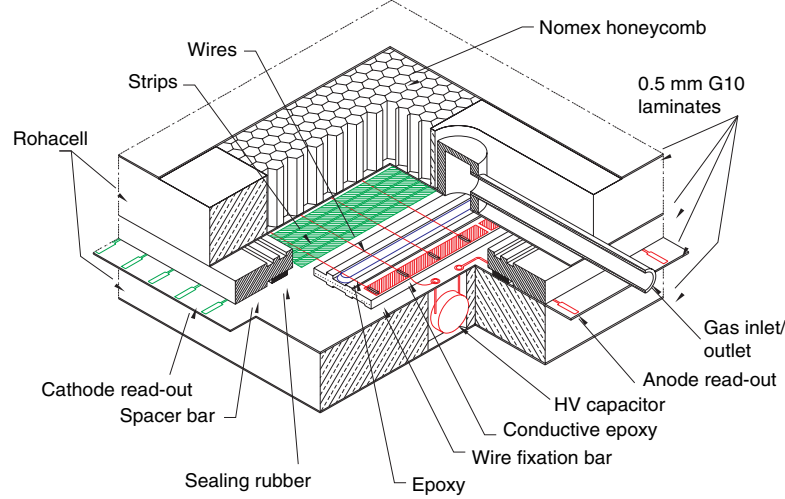


Figure 1.13: The CSC (Cathode Strip Tube).

#### 1.3.4.3 Resistive Plate Chamber (PRC)

The Resistive Plate Chamber is a trigger chamber and used in the barrel region. The RPC is the gaseous parallel plate detectors with two bakelite plates coated with layers of graphite paint providing the electric field and external pick-up strips on plastic material for the signal. A set of two orthogonal strips is used to provide two-dimensional information with good spatial resolution.

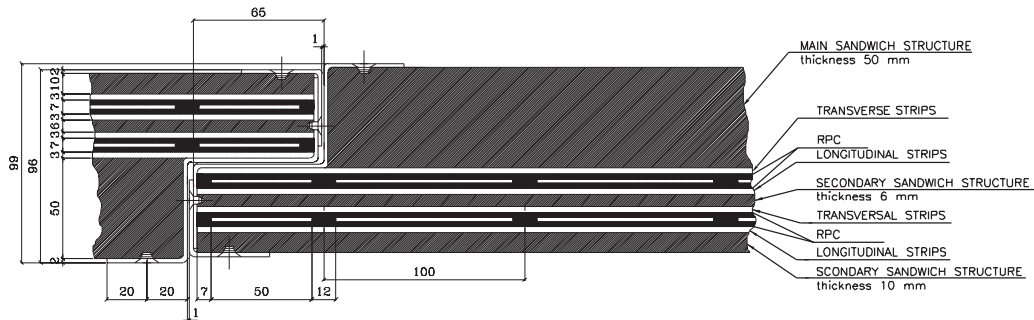


Figure 1.14: The RPC (Resistive Plate Chamber).

#### 1.3.4.4 Thin Gap Chamber (TGC)

The Thin Gap Chamber (TGC) is a trigger chamber used in the end-cap region. The TGC has a structure similar to Multi-Wire Proportional Chambers (MWPCs), except that the anode-to-anode, i.e. wire-to-wire, distance is larger than the cathode-to-anode distance. Figure 1.15 shows the TGC structure. This thin gap gives shorter drift time and high time resolution. Two graphite cathodes with distance of 2.8 mm are sandwiched with 50  $\mu\text{m}$  diameter Au-coated anode wires with a pitch of 1.8 mm. The pick-up strips are formed in orthogonal direction to the wires and this gives two-dimensional information.

To match the geometric granularity to the needed momentum resolution, from 4 to 20 anode wires are grouped and these wire-groups give R coordinates. The strips are readout individually and give  $\phi$  coordinates.

With the use of a highly quenching gas mixture of  $\text{CO}_2$  and pentane ( $\text{C}_5\text{H}_{12}$ ), 55% : 45% , this type of cell geometry allows operation in saturated mode. Saturated mode operation enables the operation with the hit-rate of 1 kHz/cm<sup>2</sup>, which is ten times greater than the estimated hit-rate at the ATLAS Experiment.

Since the TGC is too thin to satisfy the deformation requirement (maximum allowable deformation is less than 100  $\mu\text{m}$ ), two or three TGCs sandwiches thick paper honeycombs. A module with two TGCs denotes doublet and three TGCs one denotes triplet.

Figure 1.16 shows the cross-sections of triplet (left) and doublet of TGCs.

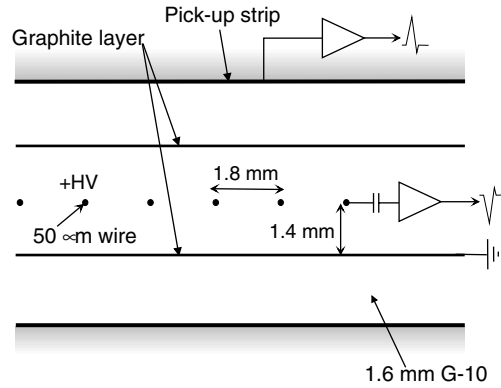


Figure 1.15: TGC structure showing anode wires, graphite cathodes, G-10 layers, and read-out strip orthogonal to the wires.

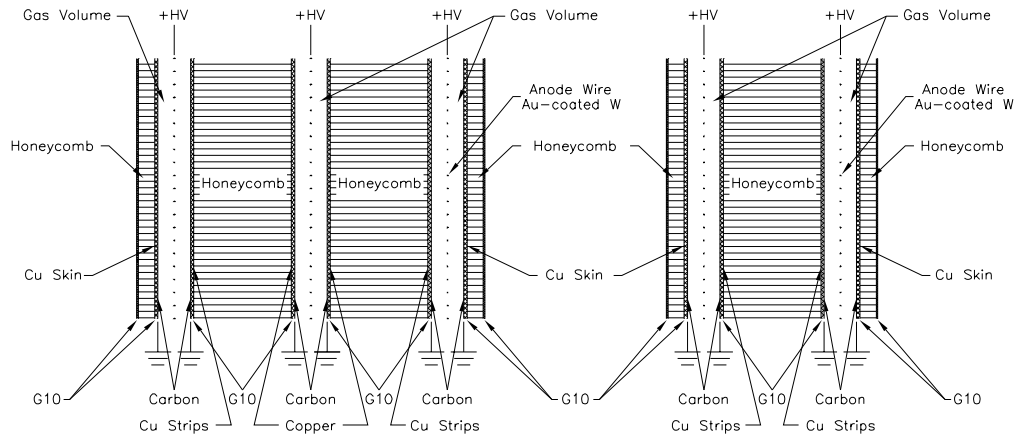


Figure 1.16: Cross-section of a triplet (left) and of a doublet of TGCs (right).

## Chapter 2

# The ATLAS Trigger/Data-Acquisition (TDAQ) System

The ATLAS Trigger and Data-Acquisition (TDAQ) system is based on three levels of online event selection. Each trigger level refines the decisions made at the previous level and, where necessary, applies additional selection criteria. Starting from an initial bunch-crossing rate of 40.08 MHz (interaction rate  $\sim 10^9$  Hz at a luminosity of  $10^{34}$  cm $^{-2}$ s $^{-1}$ ), the rate of selected events must be reduced to  $\sim 100$  Hz for permanent storage. While this requires an overall rejection factor of  $10^7$  against “minimum-bias” processes, excellent efficiency must be retained for the rare new physics, such as Higgs boson decays, that is sought in ATLAS.

Figure 2.1 shows a simplified functional view of the ATLAS TDAQ system. In the following, a brief description is given of some of key aspects of the event-selection process.

The Level-1 (LVL1) Trigger system makes an initial selection based on reduced-granularity information from the calorimeter (e,  $\gamma$ , jet,  $E_T^{\text{miss}}$ ) and muon detector( $\mu$ ). High transverse-momentum (high- $p_T$ ) muons are identified using only the trigger chambers [7]. The calorimeter selections are based on reduced-granularity information from all the ATLAS calorimeters (electromagnetic and hadronic; barrel, end-cap and forward) [8], [9].

The maximum rate at which the ATLAS front-end systems can accept LVL1 Trigger is limited to 75 kHz (upgradeable to 100 kHz).

An essential requirement on the LVL1 Trigger is that it should uniquely identify the bunch-crossing of interest. Given the short (25 ns) bunch-crossing interval, this is a non-trivial consideration. In the case of the muon Trigger, the physical size of the muon spectrometer implies times-of-flight comparable to the bunch-crossing period. For the calorimeter Trigger, a serious challenge is that the pulse shape of the calorimeter signals extends over many bunch crossings.

It is important to keep the latency (time taken to form and distribute the trigger decision) to a minimum. During this time period, information for all detector channels has to be retained in “pipeline” memories. These memories are generally contained in custom integrated

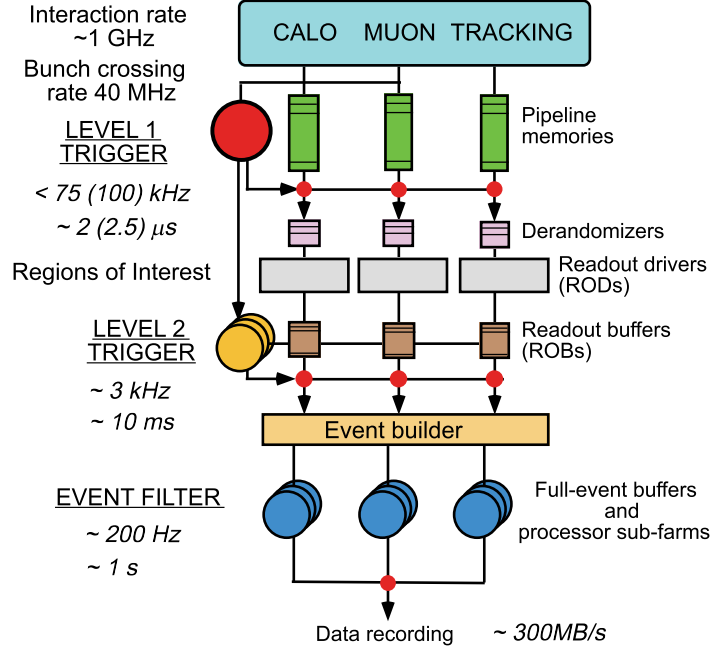


Figure 2.1: Schematic diagram of the ATLAS Trigger and DAQ System.

circuits, placed on or close to the detector, usually in inaccessible regions and in a high-radiation environment. The total number of detector channels, excluding the pixel detectors, exceeds  $10^7$ . For reasons of cost and reliability, it is desirable to keep the pipeline lengths as short as possible. The LVL1 latency, measured from the time of the proton-proton collision until the trigger decision is available to the front-end electronics, is required to be less than  $2.5 \mu\text{s}$ . In order to achieve this, the LVL1 Trigger is implemented as a system of purpose-built hardware processors. The target latency for the LVL1 Trigger is  $2.0 \mu\text{s}$  (leaving 500 ns contingency).

Events selected by LVL1 are read out from the front-end electronics systems of the detectors and put into readout buffers (ROBs). A large number of front-end electronics channels are multiplexed into each ROB. Intermediate buffers, labeled “derandomizer” in Figure 2.1, average out the high instantaneous data rate at the output of the pipeline memories to match the available input bandwidth of the readout drivers (RODs).

All of the data for the selected bunch crossing from all of the detectors are held in the ROBs either until the event is rejected by the Level-2 (LVL2) Trigger (in which case the data are discarded) or, in case the event is accepted by LVL2, until the data have been successfully transferred by the DAQ system to storage associated with the Event Filter (which makes the third level of event selection). The process of moving data from the ROBs to the Event Filter (EF) is called event building. Whereas before event building each event is composed of many fragments, with one fragment in each ROB, after event building the full event is stored in a single memory accessible by an EF processor.

The LVL2 Trigger makes use of “region-of-interest” (RoI) information provided by the

LVL1 Trigger. This includes information on the position ( $\eta$  and  $\phi$ ) and  $p_T$  range of candidate objects (high- $p_T$  muons, electrons/photons, hadrons/taus, jets), and energy sums (missing- $E_T$  vector and scalar  $E_T$  value, where  $E_T$  is transverse energy). The RoI data are sent by LVL1 to LVL2, for all events selected by the LVL1 Trigger, using a dedicated data path. Using the RoI information, the LVL2 Trigger selectively accesses data from the ROBs, moving only the data that are required in order to make the LVL2 decision. The LVL2 Trigger has access to all of the event data, if necessary with the full precision and granularity. Thanks to this RoI mechanism, usually only a few per cent of the full event data are required. The LVL2 Triggers are required to reduce the rate to  $\sim 3$  kHz. The latency of the LVL2 Trigger is variable from event to event; it is expected to be  $\sim 10$  ms.

After LVL2, the last stage of selection is performed in the EF. Here the algorithms will be based on the offline code. The EF must reduce the rate to a level suitable for permanent storage ( $\sim 300$  MB/s), currently assumed to be  $\sim 200$  Hz for full events of size  $\sim 1.5$  Mbyte.

## 2.1 Level-1 (LVL1) Trigger Overview

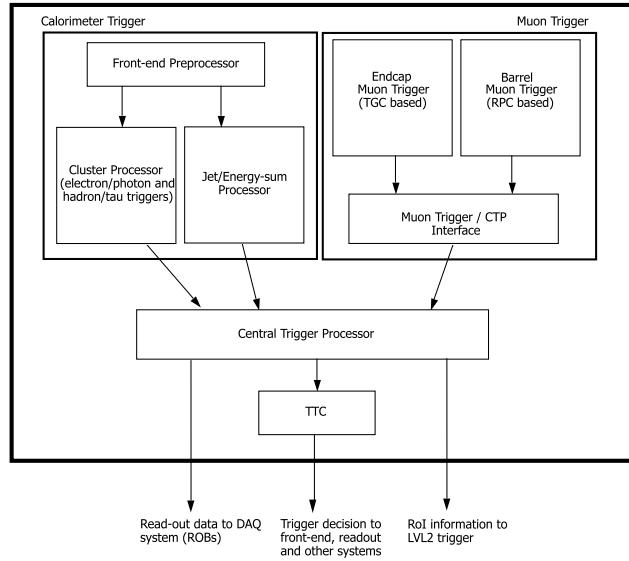


Figure 2.2: ATLAS LVL1 Trigger System.

The LVL1 Trigger is one of the most essential parts of the ATLAS Experiment for the reason that it decides whether the event is interest or not at the very early stage. As described above, the LVL2 Trigger only searches selected region by LVL1 Trigger. Therefore, if the LVL1 Trigger makes failure, there is no way to salvage significant events at any following stages.

The LVL1 Trigger system is a system of synchronous, pipelined processors running at 40.08 MHz or multiples thereof. As shown in Figure 2.2, the LVL1 Trigger system is composed of a number of building blocks: the calorimeter Trigger, the muon Trigger, the Central Trigger Processor (CTP) and the Timing, Trigger and Control (TTC) system.

In the muon Trigger, both TGC based Endcap muon Trigger subsystem and RPC based Barrel muon Trigger subsystem are operating in parallel. Each result of both muon Trigger subsystem are gathered by the Muon Trigger CTP Interface (MUCTPI) and combined data from all muon trigger chambers are sent to the CTP.

In the calorimeter Trigger, both Cluster processor and Jet/Energy processor are operating in parallel and these results are sent to CTP individually.

### 2.1.1 Muon Trigger

The Level-1 muon Trigger is based on dedicated, fast and finely segmented muon detectors. The layout of these trigger chambers, RPC detectors in the barrel regions and TGC detectors in the end-cap regions are shown in Figure 2.3. RPC Trigger system covers the pseudorapidity range  $|\eta| < 1.05$ , while the TGC Trigger system covers  $1.05 < |\eta| < 2.4$ . In order to prevent punch-through muons, RPC and TGC are overlapped at boundary region around  $|\eta| = 1.05$ . The double counting of muon tracks introduced by this overlap will be solved at MUCTPI.

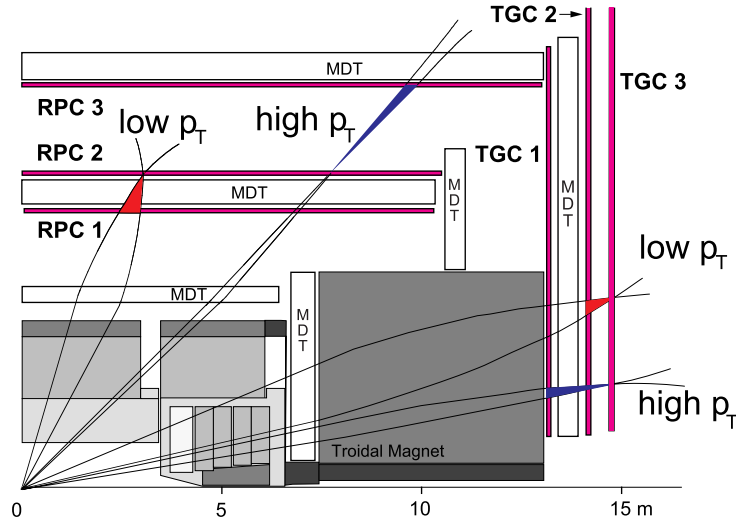


Figure 2.3: Layout of the ATLAS Muon Trigger Chambers.

There are troidal magnets at both end-cap and barrel regions creating rotating fields in  $\phi$  direction for bending muon tracks. (These troidal magnets are shown in Figure 1.11.) These trigger chambers measure muon tracks.

As illustrated in Figure 2.3, the LVL1 muon Trigger is based on three trigger stations. Two stations are used for low- $p_T$  muon triggers (threshold range approximately 6-10 GeV), while the third station is used in addition for high- $p_T$  triggers (threshold range approximately 6-35 GeV)<sup>1</sup>. High- $p_T$  triggers are made by using the results of low- $p_T$  triggers. If high- $p_T$  trigger candidates are found, they override the corresponding low- $p_T$  trigger candidates. Each station is composed of two detector planes (with the exception of the innermost TGC station that has

<sup>1</sup>For TGC, lower threshold of high- $p_T$  triggers had been extended down to 6 GeV.

three planes). Each detector plane is read out in two orthogonal projections,  $\eta$  and  $\phi$ . Both  $\eta$  and  $\phi$  trigger candidates are combined to measure the muon transverse momentum ( $p_T$ ) and two highest  $p_T$  candidates in a trigger sector are sent to MUCTPI with information of  $p_T$  value and RoI position.

## 2.2 Timing, Trigger and Control (TTC) distribution system

The TTC system is responsible for distributing a number of signals, including the LHC clock and the LVL1 Trigger decision(LVL1 Accept (L1A)), to the front-end systems. The TTC backbone is based on the optical-broadcast system developed in the RD12 Collaboration as the LHC common system [4]. While the TTC system treat many signals, the following signals are utilized in the LVL1 Trigger system.

**BC:** The LHC clock (40.08 MHz); phase adjusted clock (denoted as “de-skewed clock”) is also provided.

**L1A:** The LVL1 Trigger decision signal from CTP.

**BCR:** Bunch Counter reset signal issued by LHC machine. This signal indicates bunch-zero.

**ECR:** Event Counter reset signal. This signal is issued before the each run.

**Test Pulse:** An trigger signal to make a pseudo-hit data at each readout system.

These and other signals are encoded and transmitted optically to the front-end systems, or to intermediate points at which a change is made to detector-specific protocols for TTC distribution.

## Chapter 3

# The Endcap Muon (TGC) Trigger System

As described in Section 2.1.1, TGC provides the muon Trigger in the end-cap region. There are two sides at the ATLAS detector. All ATLAS detector layouts and connections are arranged as mirror symmetry, and there are no functional difference between both side Endcap muon Trigger electronics.

### 3.1 Layout and its Algorithm

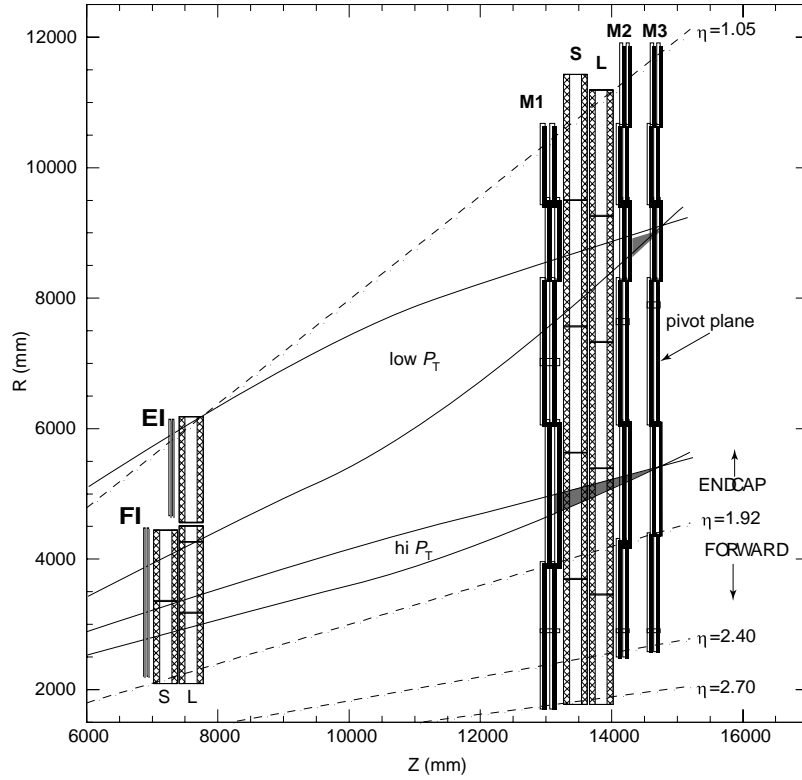


Figure 3.1: The Longitudinal view of the TGC system.

TGCs which cover end-cap region are layouted as Figure 3.1. Where EI (End-cap Inner), FI (Forward Inner), M1, M2 and M3 are the station name of TGC planes. In M1 station, triplet type TGCs are used and in M2 and M3 station, doublet type TGCs are used. (see Figure 1.16) M3 station is referred to as the pivot plane, and its chamber layout and electronics are arranged such that, to a good approximation, there are no overlaps or holes in this plane. For triggering, the TGCs cover a pseudorapidity range  $1.05 < |\eta| < 2.4$ , except for the innermost plane (EI/FI) which covers a range  $1.05 < |\eta| < 1.9$ .

Figure 3.1 also shows the LVL1 muon Trigger scheme in the end-cap region. The trigger algorithm uses pivot plane hits and extrapolates to the interaction point to construct the apparent infinite-momentum path of the track. The deviation from this path of hits found in the preceding “confirming” trigger planes is related to the track momentum. A window is constructed for each trigger region in the  $r$  and  $\phi$  directions around the infinite momentum path. A coincidence is signaled if there is a hit in the window corresponding to the hit location in the pivot plane. Independent signals are generated for  $R$  and  $\phi$ , with the wire signals determining the  $R$ -coordinate and strip signals determining  $\phi$ -coordinate. The low- $p_T$  trigger is a trigger candidate utilizes information from two doublets (M2 and M3). And the high- $p_T$  trigger is a trigger candidate utilizes information low- $p_T$  trigger and triplet (M1). In order to have a good trigger efficiency and an efficient background reduction, a 3-out-of-4 coincidence is required for the doublet pair planes of M2 and M3, for both wires and strips, a 2-out-of-3 coincidence for the triplet wire planes, and a 1-out-of-2 coincidence for the triplet strip planes is required.

Then the trigger windows are formed in  $R - \phi$  space. Using these information, muon tracks are classified into six levels of their transverse momentum ( $p_T$ ). The applied  $p_T$  threshold is determined by the size of the two-dimensional ( $R$  and  $\phi$ ) window, and for any single threshold this window is optimized to provide 90% efficiency. Tracks are flagged according to the highest threshold they cross. The final trigger decision in the end-cap system is done by merging the results of the  $R - \phi$  coincidence and the information from EI/FI chambers in order to reject tracks coming from other than the interaction point. [13]

## 3.2 Implementation on the Electronics System

In this section, a detail description and its implementation of the Endcap muon Trigger system along with the trigger path are given. Then, overview of readout system and DCS (Detector Control System) issues are given in brief.

Figure 3.2 shows an overview of the TGC LVL1 Trigger electronics scheme and Figure 3.3 shows the placement of these electronics relative to the trigger chambers. The wire and strip signals emerging from the TGC are fed into a two-stage amplifier in an Amplifier Shaper Discriminator (ASD) circuit [23] [24]. Four ASD circuits are built into a single ASD chip and four ASD chips are incorporated into an ASD Board; hence each ASD Board handles 16

channels of signals. The ASD Board is physically attached to the edge of a TGC and enclosed inside the TGC electrical shielding.

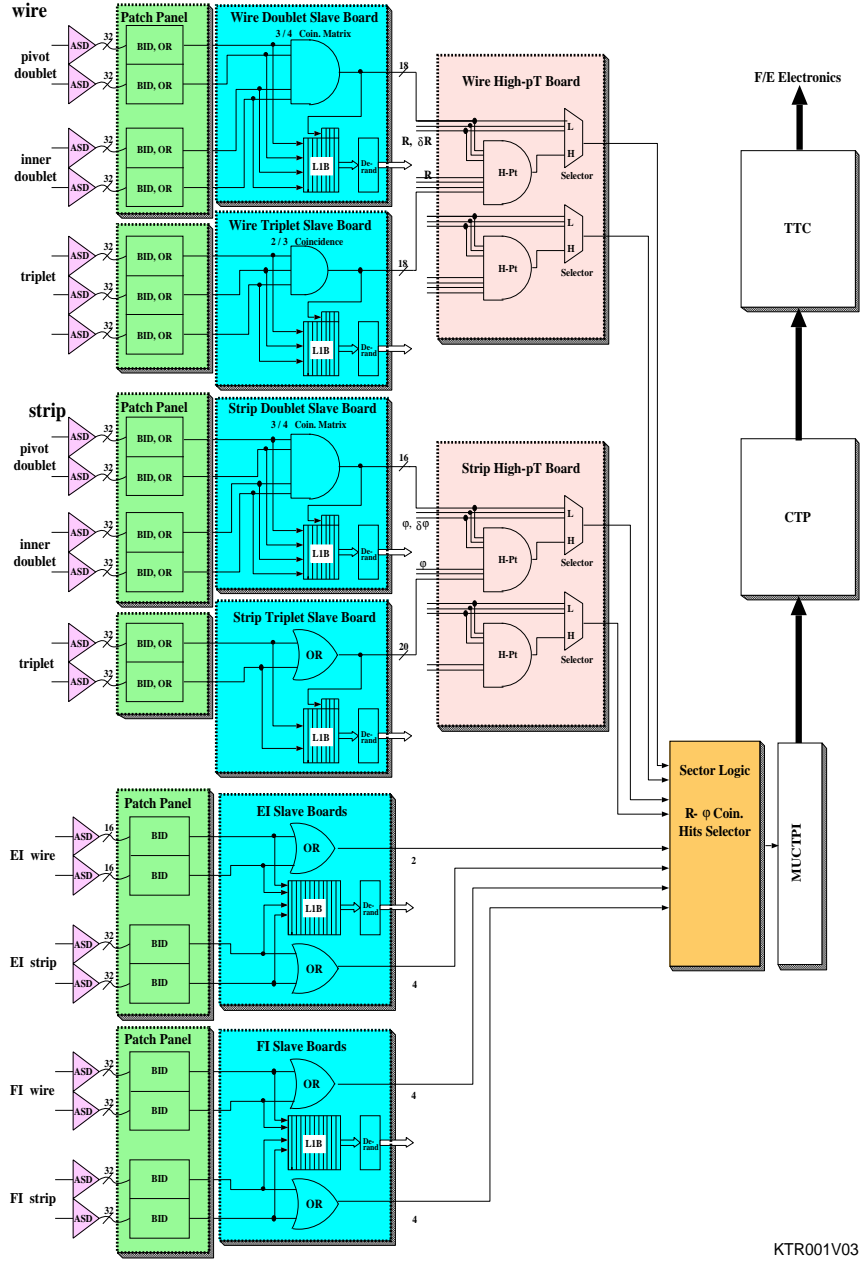


Figure 3.2: Overview of the TGC LVL1 Trigger electronics system.

Signals from the ASD Boards are sent to a PS-Board where Patch-Panel (PP) ASICs and Slave Board (SLB) ASICs are implemented. PS-Boards are placed on the accessible outer surfaces of the TGC wheels except for EI/FI PS-Boards. Thus, electronics for the two doublets are mounted on the outside of the outer doublet wheel and those for the triplets on the inner surface of the triplet wheel. The PP ASIC has 32 channels of Bunch-Crossing Identification (BCID) circuits. Outputs from PP are fed to the on-board logic to take care of physical overlap

in the TGCs and fan-outs.

The processed signals are sent to corresponding SLB ASICs where the coincidence and read-out circuits are placed. There are five different types of SLB; wire and strip boards for each of the triplet and doublets and a board for the EI/FI chamber. They differ in their number of inputs, the kind of coincidence made and the maximum window width.

Information from the SLBs for the triplet and doublets is encoded to produce more compact signals and the encoded coincidence information is passed to a High- $p_T$  coincidence Board located near the outer rim of the triplet wheel. Signals from the doublet and triplet SLBs are combined here to find high- $p_T$  track candidates. Wire (R-coordinate) and strip ( $\phi$ -coordinate) information is treated separately.

Signals from the High- $p_T$  Boards are sent to Sector Logic Boards containing an R- $\phi$  coincidence unit and track selectors, to select the highest- $p_T$  candidates. In the Sector Logic, hit information from EI/FI SLBs is incorporated to the trigger logic. This provides excellent robustness against soft charged particles due to the very large field integral produced by the forward toroids located between the Trigger system and the innermost muon station. The Sector Logic boards are located in USA15 outside the main ATLAS cavern. The resulting trigger information is sent to the MUCTPI in a standard format [16]. The total latency of the system, from the bunch-crossing in which the interaction occurs until the delivery of the LVL1 track candidates to the MUCTPI is  $1.20 \mu s$ .

Full-information data sets are read-out through the DAQ system in parallel with the primary trigger-logic. For read-out purposes the SLBs of one or more trigger sectors are grouped into Local DAQ Blocks. Each SLB is connected to the Star Switch (SSW) which manages the data collection for a Local DAQ Block. The transfer, via S-LINK (using optical fiber), of data from the SSW witch to the Read Out Drivers (ROD) in USA15 is managed by the Local DAQ Master.

The DCS has been developed on a ATLAS wide system to controle and monitor detectors. The DCS is a slow path primarily for initial setting of the system and monitoring the environment, power, gas flow, etc. TGC DCS is implemented by using the CAN-bus system.

### 3.3 Trigger Sector

Figure 3.4 shows the pivot plane formed by the TGC doublet plane furthest from the interaction point. As shown in Figure 3.1 the pivot plane is divided into two regions, ENDCAP ( $|\eta| < 1.9$ ) and FORWARD ( $|\eta| > 1.9$ ). The end-cap region of each octant (one eights of pivot plane) is divided into six trigger sectors in  $\phi$ , where a trigger sector is a logical unit that is treated independently in the trigger. Similarly the Forward region of each octant is divided into three trigger sectors. Thus in each side of TGC wheels, there are 48 ENDCAP trigger sectors and 24 FORWARD sectors.

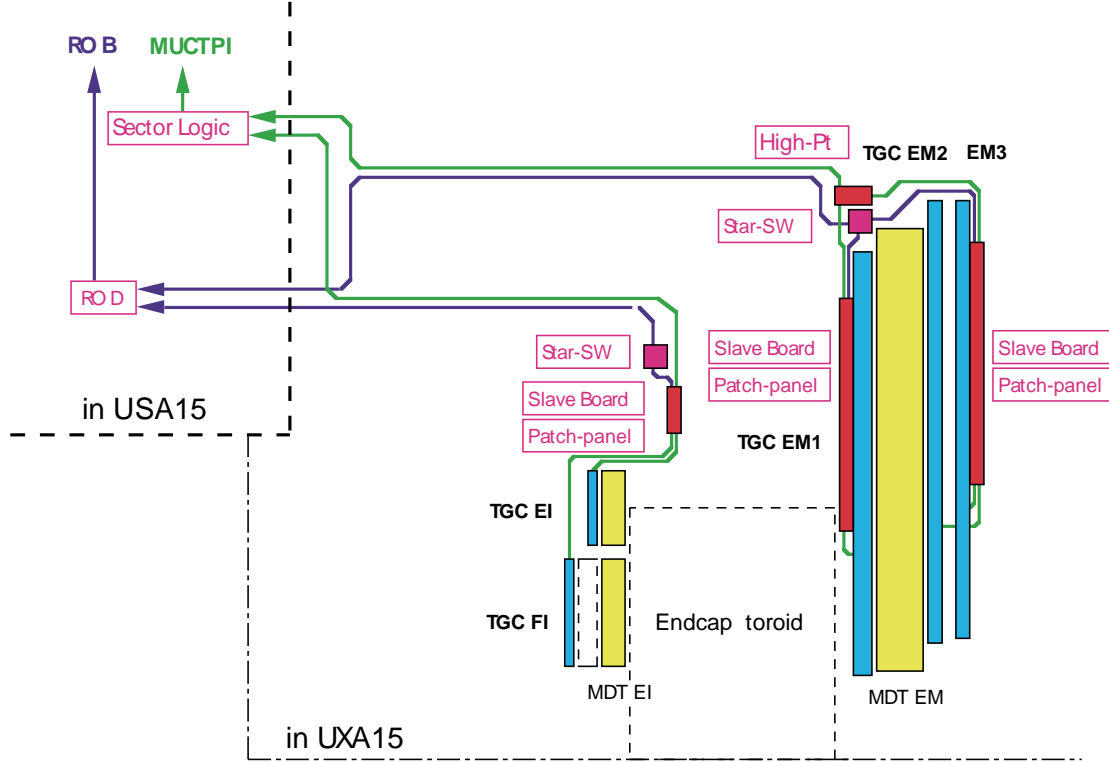


Figure 3.3: TGC electronics placement.

In each trigger sector, the two highest- $p_T$  track candidates are selected and sent to the MUCTPI.

The small region, shown by read dashed line in Figure 3.4 is a trigger subsector which corresponds to the smallest unit area of the trigger segmentation. A trigger subsector corresponds to eight channels of wire-groups and eight channels of readout strips. An ENDCAP trigger sector contains 37  $\eta$  rows by 4  $\phi$  columns, 148 trigger subsectors in total. A FORWARD trigger sector contains 16  $\eta$  rows by 4  $\phi$  columns, 64 trigger subsectors in total. Each trigger subsector corresponds to one Region of Interest (RoI). Each subsector is treated independently in the trigger so that the  $\Delta r$  and  $\Delta\phi$  inputs that determine the  $p_T$  condition applied can be set separately for each subsector.

System segmentation is different between the detector and trigger logic. Each chamber output is divided into 16-channel segments, corresponding to output from ASD boards (described below). This segmentation, however, does not correspond to the trigger segmentation in wire-group signals since the chamber layout in R-direction shown in Figure 3.1 is not projective toward the interaction point. Hence the signals should be rearranged into proper segments before entering trigger logic. Figure 3.5 shows the wire-signal segmentation. As shown in the figure, trigger segments are over the boundaries of chambers, and signal exchanges are necessary between them. This signal rearrangement is taken care of by PS-Boards. Totally 19 kinds of PS-Boards are made and every signals are rearranged by rerouting and/or between adjacent

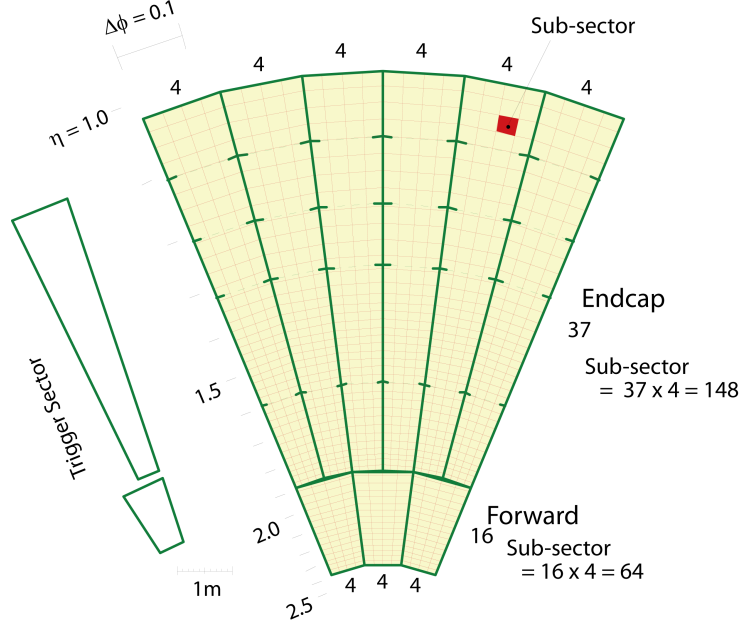


Figure 3.4: TGC LVL1 Trigger segmentation for an octant (one eighths of pivot plane). One octant wheel is divided into six ENDCAP sectors and three FORWARD sectors. Bold lines in the figure indicate individual trigger sectors. They are further subdivided into trigger subsectors.

boards. For strip signals, the segmentation is same between the chamber and electronics and no signal exchanges are needed. Details of signal rearrangement in PS-Boards are described in “The TGC Excel Parameter Book” [25].

### 3.4 Latency

The total estimated latency of the Endcap muon Trigger system from interaction through to the input to the MUCTPI is  $1.20 \mu\text{s}$ . The contributions to this latency are listed in Table 3.1. Adding the additional 12 bunch crossings for the MUCTPI and CTP, plus 20 bunch crossings for the TTC and the cable back to front-end electronics, gives a total latency of  $2.00 \mu\text{s}$ . This meets the requirement of  $2 \mu\text{s}$  and provides the full  $0.5 \mu\text{s}$  contingency allocated within the  $2.5 \mu\text{s}$  absolute maximum latency.

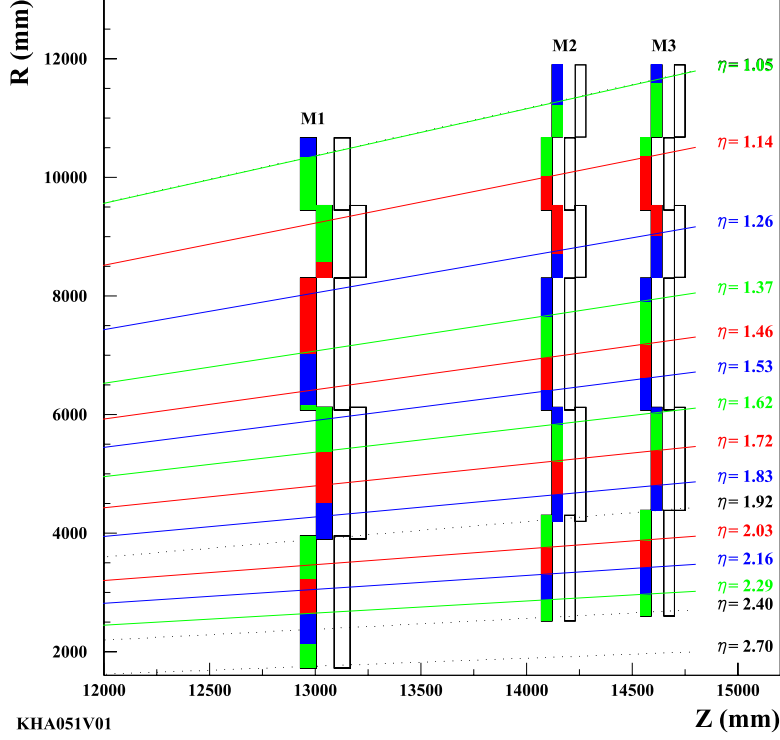


Figure 3.5: Wire-signal segmentation. Each small box represents a segment of 32 channels, corresponding to 4 subsectors.

Table 3.1: contributions to the total estimated TGC latency, in bunch-crossing in number of bunch crossing. (BC) (1 BC = 25 ns)

Process/transmission	Time required	Accumulated time
TOF to TGC	3	3
TGC response	1	4
ASD	1	5
Cable to Patch Panel	2	7
Bunch-crossing ID and OR (PP ASIC)	2	9
Cable to SLB	0	9
Delay Adjust (SLB ASIC)	1	10
3/4 or 2/3 coincidence (SLB ASIC)	3	13
Cable to high- $p_T$ coincidence	3	16
Delay adjustment (HPT ASIC)	1	17
High- $p_T$ coincidence matrix (HPT ASIC)	4	21
Optical cable to USA15 (90 m)	18	39
Sector Logic processing	8	47
Cable to MUCTPI (5 m)	1	48
Total delay sum	48BC	1.20 $\mu$ s

## Chapter 4

# System Development Issues

This section is devoted for both the discussions on technology selection and radiation tolerance test, and the detailed design and its specification of the components which the author had developed.

### 4.1 Technology selections for the system components

In this section, discussions on the requirements of choosing devices for each component are described. As following reasons, we decided to use only ASIC and Anti-Fuse type FPGA for electronics devices located in the experimental hall.

The FPGA (Field Programmable Gate Array) and the CPLD (Complexed Programmable Logic Device) are popular devices and have convenient features such as; reprogrammable<sup>1</sup>, wide line-up of its gate size and speed range, and availability. For this reason, the FPGA/CPLD is widely used for today's electronic circuits such as computers, networking equipments and scientific instruments.

FPGAs and CPLDs have large configuration memories to determine its functionality. There are two types of configuration memories: SRAM (volatile) and Flash (non-volatile). The configuration data stored in the memories set properties of whole logic blocks and set connections between logic cells and I/O ports.

It is known that bit-flip phenomenon of their configuration memories at high radiation environment, and this may cause function failure of the device. Such data change can be found by read-back the configuration data from the device periodically. Thus such a failure can be fixed by re-configuring the device. Using this method (periodical read-back & re-configuration), the system functionality can be retained except the read-back cycle duration<sup>2</sup>.

This technique sounds good idea, therefore at first TGC system planed to adopt both SRAM-based FPGAs and Flash-based CPLDs for some components.<sup>3</sup> However, we've found

---

<sup>1</sup>This means any circuit modifications can be done after the components made.

<sup>2</sup>The period of read-back from each device should be determined in consideration of MTBF (Mean Time Before Failure) by the modification of configuration memories and the number of this type of devices.

<sup>3</sup>In that design, the read-back and re-configuration are done by using a Flash-based CPLD (non-volatile).

the studies [39] [40] [41] that Flash memories can not be used in the radiation environment; its charge-pump that makes high voltage to re-writing may be broken. By this reason, we have changed the design to eliminate all memory embedded FPGAs and CPLDs.

We've adopted the Anti-Fuse type FPGA<sup>4</sup> made by Actel as a substitute. Anti-Fuse type FPGA is used in the aerospace applications where devices are exposed to high radiation level. Anti-Fuse type FPGA has no configuration memories in the device and can be programmed only one time. Candidate devices were tested and proved to have sufficient radiation tolerances. In details, see Section 4.4.

Meanwhile, the ASIC (Application Specific Integrated Circuit) is another choice to implement the circuit. ASICs are specially designed devices for a particular application. ASICs have advantages such as; high-speed operation, low power consumption, and large flexibility in chip design (e.g. implement Memory Macros). While ASICs have ideal characteristics, initial costs for ASIC development are considerably expensive so that ASICs can be used for limited applications where large number of the same chip is used.

Next, we have to protect remaining user registers which are used to set the functional properties. We've introduced the Voting Logic (or referred as Triple Module Redundancy (TMR)). As shown in Figure 4.1, Voting Logic consists of three D-type Flip-Flops and four gates. This logic maintains an initial value even if any one Flip-Flop causes bit-flip. Since the probability of bit-flips in two Flip-Flops for the same Voting Logic register is extremely low, thus this technique is efficient way to protect the user register.

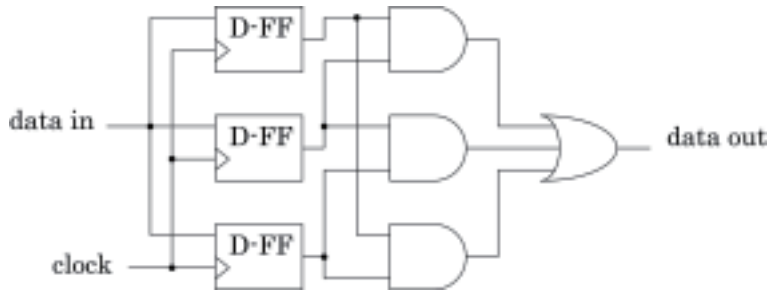


Figure 4.1: Voting Logic implementation: Three D-type FlipFlops are used to implement 1bit Voting Register. Even if any one register value flipped, the data out keeps the initial value.

Since a Voting Logic register consumes over three times resources than a usual register, the size of device resources need to be taken into account.

Figure 4.2 shows the device selection we've done for our system. Four components, PP, SLB, HPT and ASD, are implemented in the ASIC, because number of these components in the system is large (over a few thousands). Since radiation level in the USA15 is not so severe,

---

<sup>4</sup>An Anti-Fuse is an electrical in a silicon device that performs the opposite functions of a fuse. Whereas a fuse starts with a low resistance and is designed to permanently break an electrically conductive path, an antifuse starts with a high resistance and is designed to permanently create an electrically conductive path.

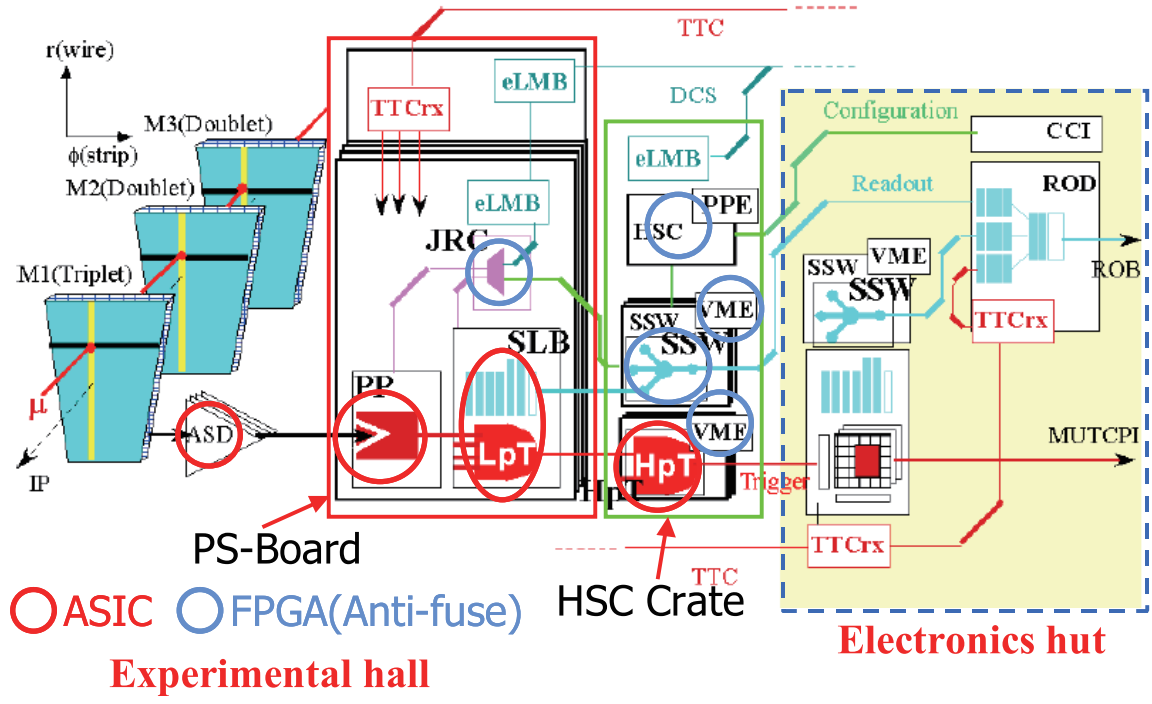


Figure 4.2: Device selection at the TGC electronics system.

any FPGA can be used. In Section 4.3, the development of the Sector Logic, which is located in the electronics hut, is described.

## 4.2 Slave Board ASIC

### 4.2.1 Overview

The SLB ASIC has two main roles. One is to do coincidence for low- $p_T$  triggers. This ASIC receives synchronized hit data from PP ASIC for either wire or strip as input signals and makes coincidence operations. The other is to keep hit data until the LVL1 trigger arrives and send them to SSW after the LVL1 trigger. This Readout block consists of the pipe-line buffer (Level-1 Buffer) and the derandomizer (FIFO type memory).

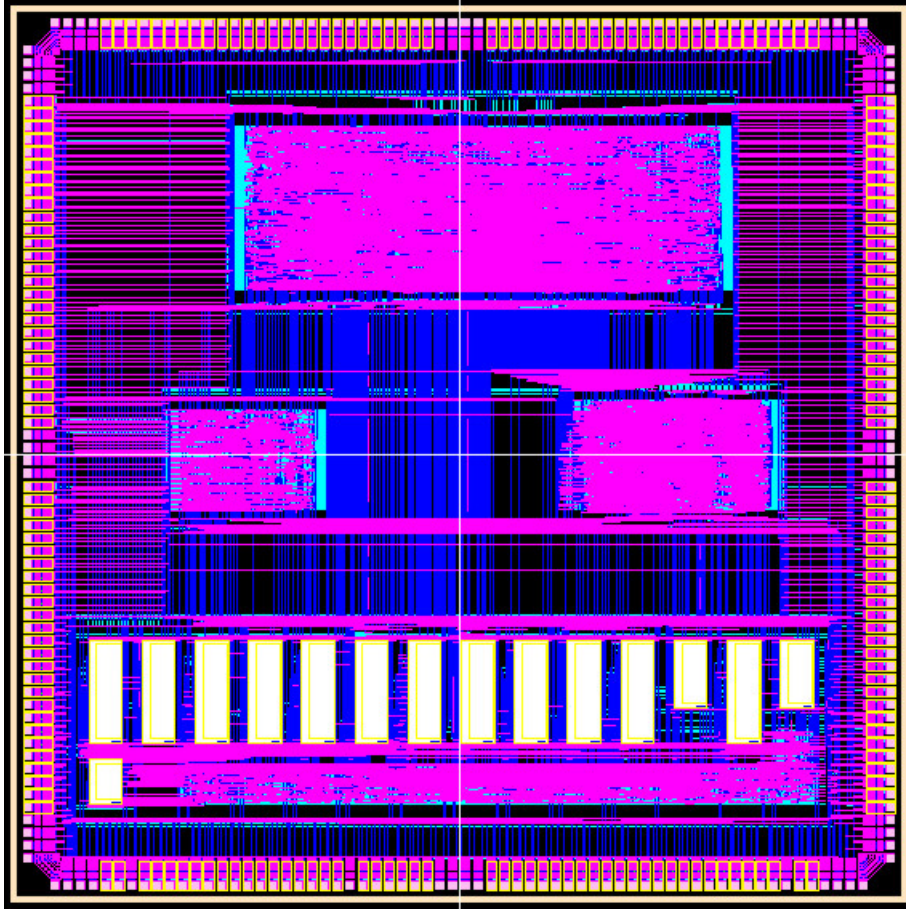


Figure 4.3: Layout Mask pattern of SLB ASIC Version 6. This version is final design and mass-production has done with this design.

Figure 4.3 shows the mask pattern of the Slave Board (SLB) ASIC. It was processed with Rohm full custom  $0.35\ \mu\text{m}$  gate width CMOS technology in  $9.86\ \text{mm} \times 9.86\ \text{mm}$  die size. The ASIC has over  $2 \times 10^5$  gates. It operates on 3.3 V supply voltage.

### 4.2.2 Master-Slave Structure

At the first phase of SLB ASIC development, we have suffered a serious problem at shift registers. Data changes and/or fluctuations of shift register length were observed. We found 0.2 to 1.6 ns timing difference between clock signals for different Flip-Flops whereas clock signal to all the shift registers must be synchronized. This timing difference was introduced by the difference of the propagation delays of the clock signal line. As shown in Figure 4.4, the following Flip-Flop may cause timing violation. In such case, its output is unpredictable, and this state is known as metastable state (quasi stable state). At the end of metastable state, Flip-Flop settles down to either “1” or “0”. This whole process is known as metastability. The problem in our ASIC was caused by this metastable in the shift-registers.

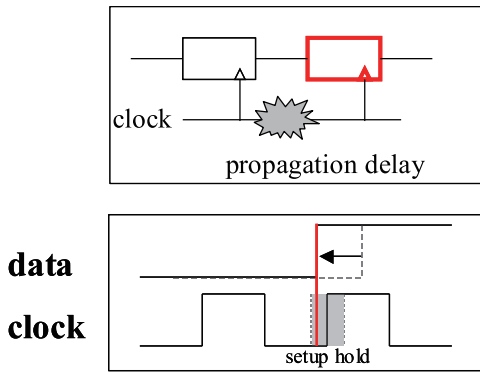


Figure 4.4: Normal Shift Register.

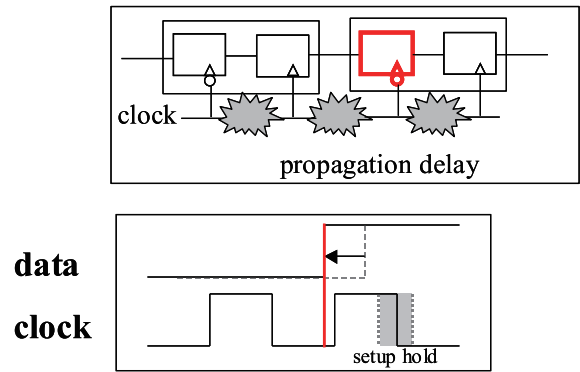


Figure 4.5: Master-Slave Shift Register.

To solve this problem, we have introduced two methods. One is enhancement and optimization of the clock tree synthesis (CTS) in the chip Place&Route process. The other is adoption of bi-phase structure in the logic. Namely we shifted the timing of data load to a shift register a half clock. In order to implement this feature, we have changed the simple shift register structure to so called Master-Slave structure shown in Figure 4.5.

### 4.2.3 Block Diagram

As shown in the Block Diagram (Figure 4.6), the SLB ASIC consists of four blocks. Each block is implemented into a macro core as an independent functional unit in the ASIC. These four functional blocks are:

1. Input (Input Block)
2. Low- $p_T$  trigger (Trigger Block)
3. Readout (Readout Block)
4. JTAG Control (JTAG Block)

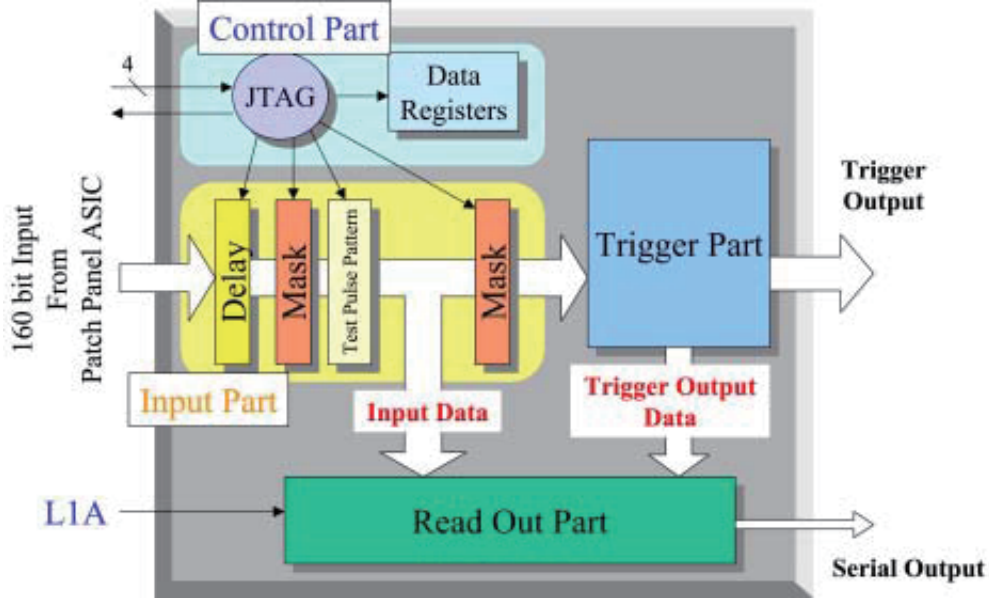


Figure 4.6: Block Diagram of the SLB ASIC.

The macro core structure can be seen from the picture of the ASIC layer mask pattern. Several small squares regularly aligned at the bottom in Figure 4.3 are the macro cores for the Readout block with the memory of 128 bits depth and 12, 20 or 32 bits widths while the single large square at the top is for the input block. The small squares in the central part are the JTAG control and the low- $p_T$  matrix blocks from left to right.

#### 4.2.4 Input Block

The SLB ASIC can accept maximum 160 input signals from PP ASICs. In the Input block, every individual channel can be masked in three different ways. The mask can be set as:

1. through input data (no mask),
2. always low (=0; force cold channel)
3. always high (=1; force hot channel)

Namely we have 2 bits mask for each channel. The mask registers can be accessed with the standard JTAG protocol. In addition, we have two masks for one input channel; one for hit signal stream (thus consequently for the trigger stream too) and the other one for only trigger data stream. The concept of this double mask scheme for a channel is shown in Figure 4.7.

The “always high” logic can improve acceptance loss that comes from dead channels even if one chooses the 4-out-of-4 coincidence logic. The “always low” logic is used to eliminate noisy channels and unwanted channels for the trigger. The masking logic posterior to the phase-adjust circuit has a function of a test pulse input. The test pulse is triggered by the Test Pulse

signal from TTC and can be delayed programmable. Independent MASK for Test Pulse signal is also equipped.

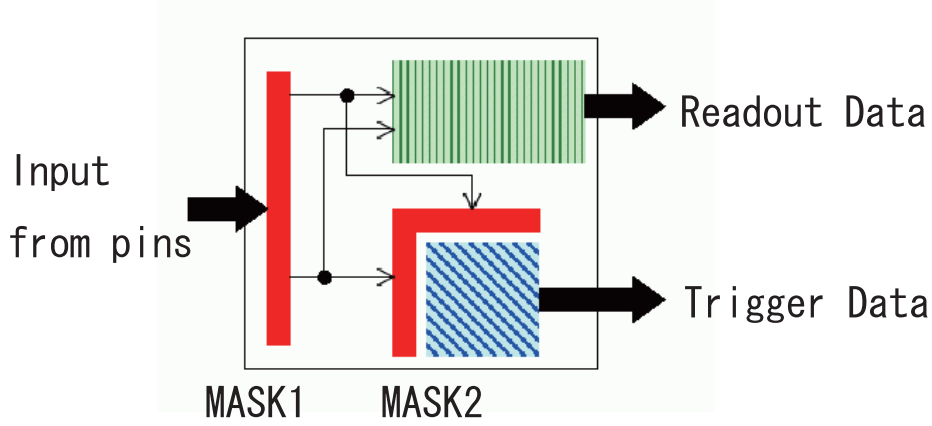


Figure 4.7: Double mask scheme implemented in the SLB ASIC, two masks are shown in the (red) solid squares. One is common for the Readout and the Matrix, and the other one is only for the trigger matrix.

Input channels are divided into four segments. Each segment has a delay circuit to adjust the input phase with signals from other segments. Channels in one segment can have, therefore, a common delay adjustment. The adjustable delay range is from 1 to 4.5 clocks with 0.5 clock step (3 bits).

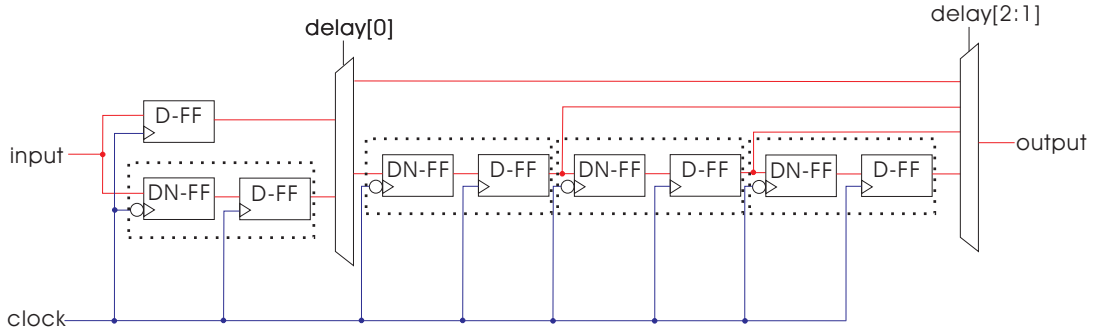


Figure 4.8: Schematic of Delay Circuit of SLB ASIC Input block. At first, the input signal is latched either on Positive edge (D-FF) or Negative edge (DN-FF). Following delay shift register circuit is formed by the Master-Slave structure.

Figure 4.8 is the delay circuit for the SLB ASIC. The input signal is latched either on Positive edge (D-FF) or Negative edge (DN-FF) of system clock. Then, the output is fed to delay circuit. This delay circuit is formed by the Master-Slave structure.

#### 4.2.5 Low- $p_T$ trigger Block

In order to manipulate the trigger operation for all five different input configurations (Wire Doublet (WD), Strip Double (SD), Wire Triplet (WT), Strip Triplet (ST) and EI/FI) with one

single ASIC, the Low- $p_T$  trigger block has three main logics, which are selectable by setting appropriate registers. A coincidence matrix technique is used commonly for wire WD and strip SD configurations while 2 out of 3 and 1 out of 2 (or) logics are used for WT and ST respectively. EI/FI is used ST logic. In the following subsections, the implementations of these logic are described.

#### 4.2.5.1 Coincidence Matrix for Doublets pair (DSB)

The Doublet Slave Board (DSB) services the four layers of the two sets of TGC doublets. A block diagram of the Doublet Slave Board is shown in Figure 4.9, where Phase adjust and Masks are implemented in Input block (see Section 4.2.4) and L1 buffers, Derandomizer and counters are implemented in Readout block (See Section 4.2.6) respectively.

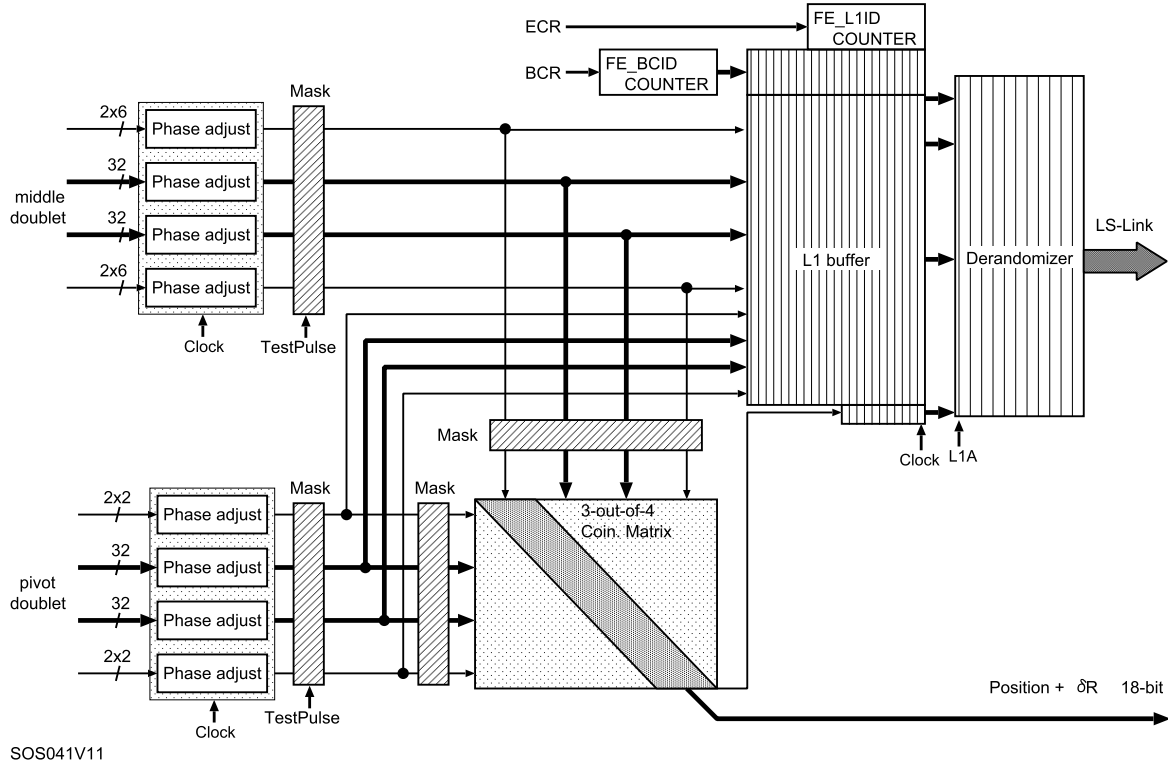


Figure 4.9: The functional structure of a Slave Board for the TGC doublet pairs. Shown is the wire Slave Board; the strip Slave Board has 16-bit output instead.

Each DSB covers a 32-channel per layer width of either wire or strip signals, giving 128 channels of inputs to a DSB from the four TGC layers. For wires, a track segment found by the coincidence matrix is encoded as an 18-bit word containing  $R$ , its pivot plane position, and  $\Delta R$ , its deviation from the infinite momentum path. Similarly, for strips, a 16-bit word is encoded containing  $\phi$  and  $\Delta\phi$  information. If high background rates produce a large number of accidental coincidences, the 3-out-of-4 coincidence matrix can be programmed to provide a 4-out-of-4 coincidence offering a more robust trigger.



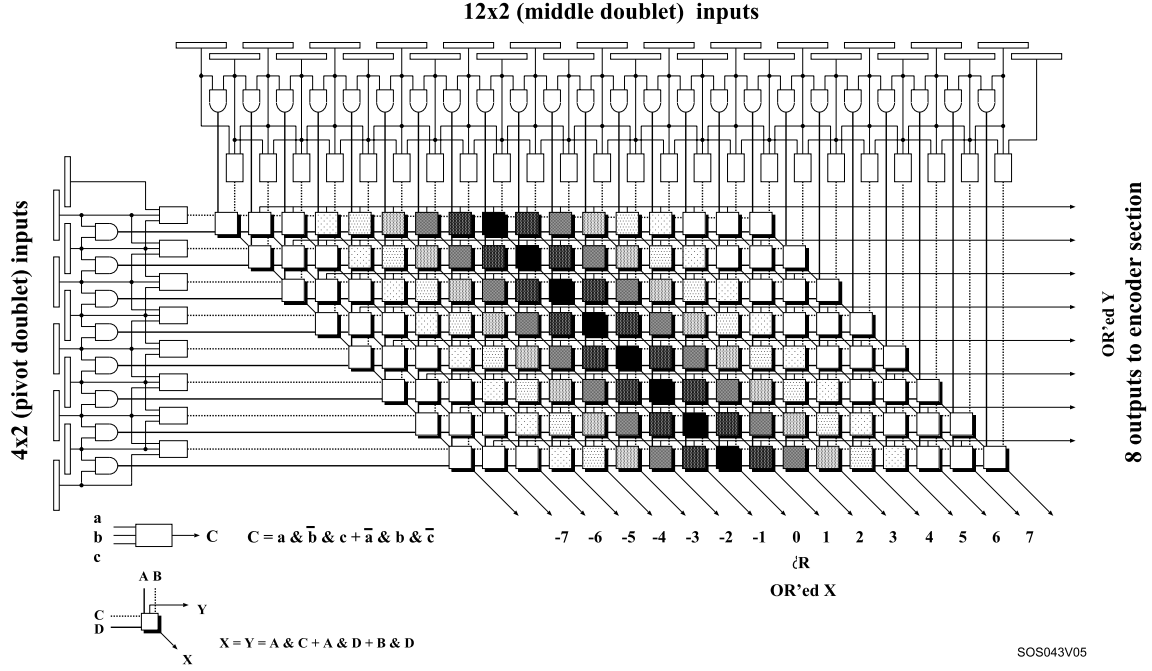


Figure 4.11: Detailed structure of the 3-out-of-4 Low- $p_T$  matrix for wires. Also shown is the function of a matrix element. Cells with the same shading have the same  $\Delta r$ . The matrix for  $\phi$  is the same, except  $\Delta\phi$  goes from  $-3$  to  $+3$ . (Actually  $X$  and  $Y$  in the figure are the same.)

for the half-cell staggering between layers in order to improve the effective resolution. The 3-out-of-4 coincidence is then performed in each coincidence element. When a coincidence is found, a hit signal and  $\Delta R$  (or  $\Delta\phi$ ) signal are generated. Hit signals in the elements of each row are OR'ed, while the  $\Delta R$  (or  $\Delta\phi$ ) signals are OR'ed along the diagonal elements. For  $R$ , the  $\Delta R$  output pattern is 15 bits wide; for  $\phi$ , the  $\Delta\phi$  output pattern is seven bits wide.

In Figure 4.10, the coincidence matrix is shown divided into two halves,  $A$  and  $B$ , (each half services signals from a 16-channel per layer width) and the highest- $p_T$  track candidate found in each half is selected. Hence the OR'ing mentioned above is done for each half independently. To select the highest- $p_T$  track,  $\Delta R$  (or  $\Delta\phi$ ) outputs are examined first and then the selected hits with the smallest  $|\Delta R|$  from the 3-out-of-4 coincidence are passed through declustering logic to produce a single track. Figure 4.12 shows the declustering rules. Even though a real particle almost always makes at most two hits, a cluster is treated as a single track, regardless of its size. If more than one cluster is found in any half-matrix, only the highest- $p_T$  track candidate is kept. For wires, the 15-bit  $\Delta R$  pattern ( $\Delta R = -7$  to  $\Delta R = +7$ ) is encoded in four bits and position information is encoded in five bits so that the  $R$  information for each track is nine bits wide. This encoding reduces the required number of cables and hence the line-driver power dramatically. Since each of the two halves of the Slave Board can produce a track candidate, the output from this circuit is 18 bits wide. For strips, the seven bit wide  $\Delta\phi$  pattern ( $\Delta\phi = -3$  to  $\Delta\phi = +3$ ) is encoded in three bits. Position in  $\phi$  is encoded in five bits

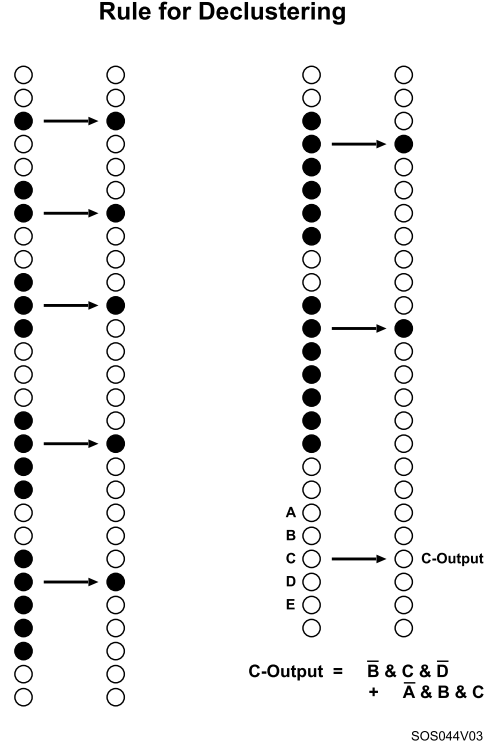


Figure 4.12: Declustering rules. When a hit pattern wider than two is found, the rules shown assign a position to the track.

so that the  $\phi$  information for each track is eight bits wide and for the two highest- $p_T$  tracks, 16 bits. Despite this attention to multi-muon encoding, the occurrence of more than one muon in the area covered by a Slave Board is rare.

#### 4.2.5.2 Triplet Slave Board (TSB)

The Triplet Slave Board (TSB) (Figures 12-18 and 12-20) performs coincidence operations on signals from the three layers of the triplet. The TSB is similar to the Doublet Slave Board. The wire coincidence operation uses 2-out-of-3, and the strip 1-out-of-2, logic. Figure 4.13 and Figure 4.15 show the TSB trigger-logic and Readout components for wires and strips respectively.

**Wire Triplet Slave Board:** Each wire TSB receives from each layer of TGCs a 36-channel wide wire pattern. It also includes two bits from each of the two adjacent boards to take care of boundaries between regions covered by adjacent Slave Boards, resulting in a 108-bit input pattern. The coincidence matrix is subdivided into three 32-channel sections. The structure of the 2-out-of-3 coincidence for triplet wire signals and the logic equation are shown in Figure 4.14. Signals first pass through circuits to account for the cell-staggering of  $1/3$  between successive layers before they go through the coincidence circuits. A 3-out-of-3 coincidence can also be required should the background rate be

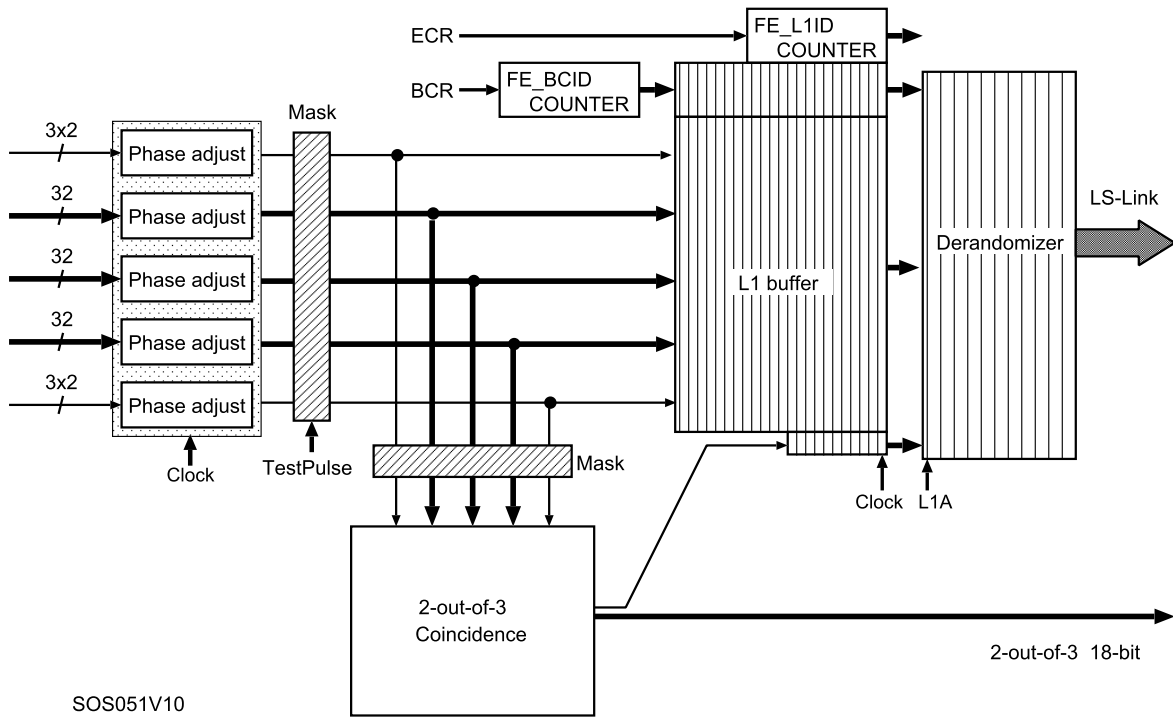


Figure 4.13: Slave Board for TGC Triplets (for wire signals).

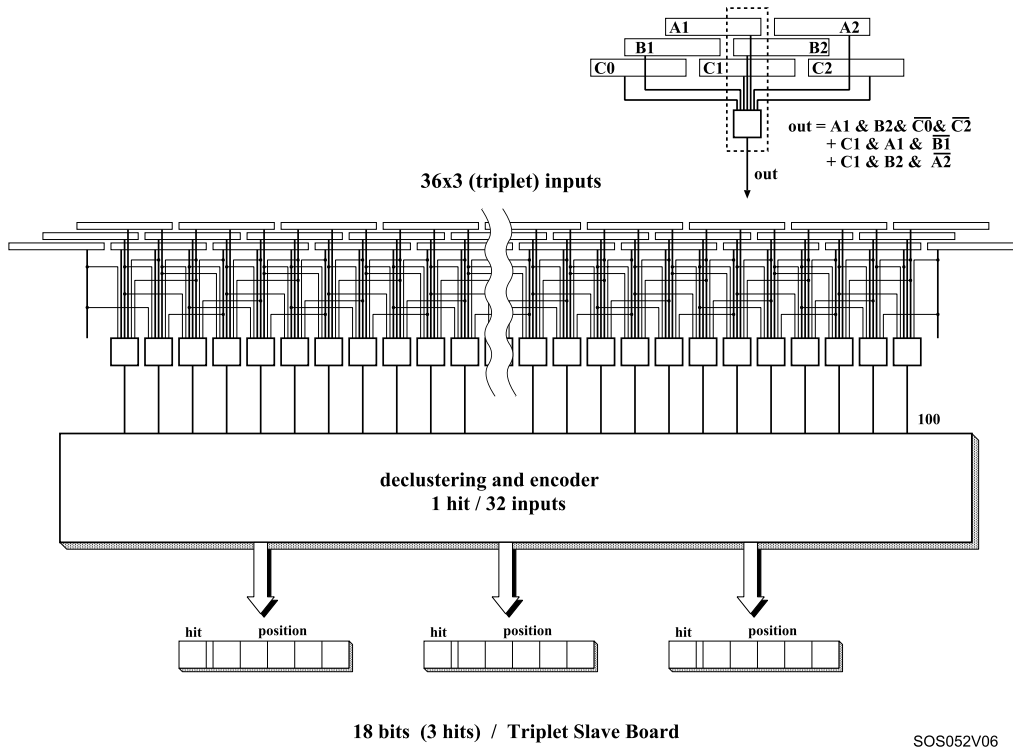


Figure 4.14: Structure of the Triplet logic for wire signals. Logic to deal with the staggering of triplet layers and the output format after encoding is also shown.

so high that the accidental coincidences force a more robust approach. The output is encoded to form a 5-bit hit position plus a 1-bit hit-found flag giving a total of six bits for each hit. The hit at highest R is selected from each section giving three hits per TSB, an 18-bit wide result after encoding (see Figure 4.14).

**Strip Triplet Slave Board:** The middle TGC of the triplet does not have strips so there are only two 32-bit patterns. No channels from adjacent boards are used in this logic. A single strip TSB is able to serve two TGC triplets, and so each strip TSB receives 128 channels of strip signals. The strips are staggered by  $1/2$ . Figure 4.15 shows the block diagram of the strip TSB. The inner structure is similar to that for the wires. However, as shown in Figure 4.16, the coincidence operation performed for the strips is 1-out-of-2. The full logic equation is given in the figure. Again, this coincidence section can be configured to provide a 2-out-of-2 coincidence should the background rate become too high. The 32-bit wide per layer input pattern is split into four sections, each eight channels per layer wide. The declustering logic, as described in Section 4.2.5.1, selects one hit per section. Each hit is encoded as a 4-bit position plus a 1 bit valid hit flag. The four sections thus give a 20-bit wide output per triplet as shown in Figure 4.16, resulting in a 40-bit output per strips TSB.

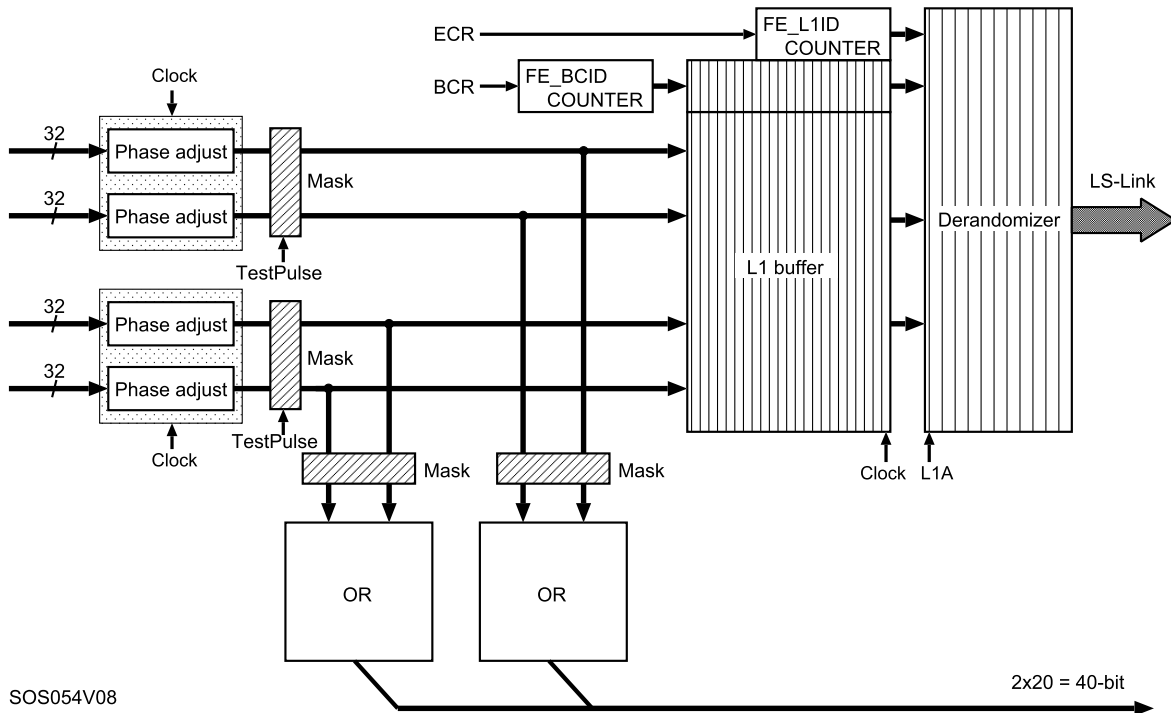


Figure 4.15: Functional structure of a Slave Board for TGC Triplet strip signals. There are only two active layers of strips per “triplet”. One chip handles up to two triplet units independently.

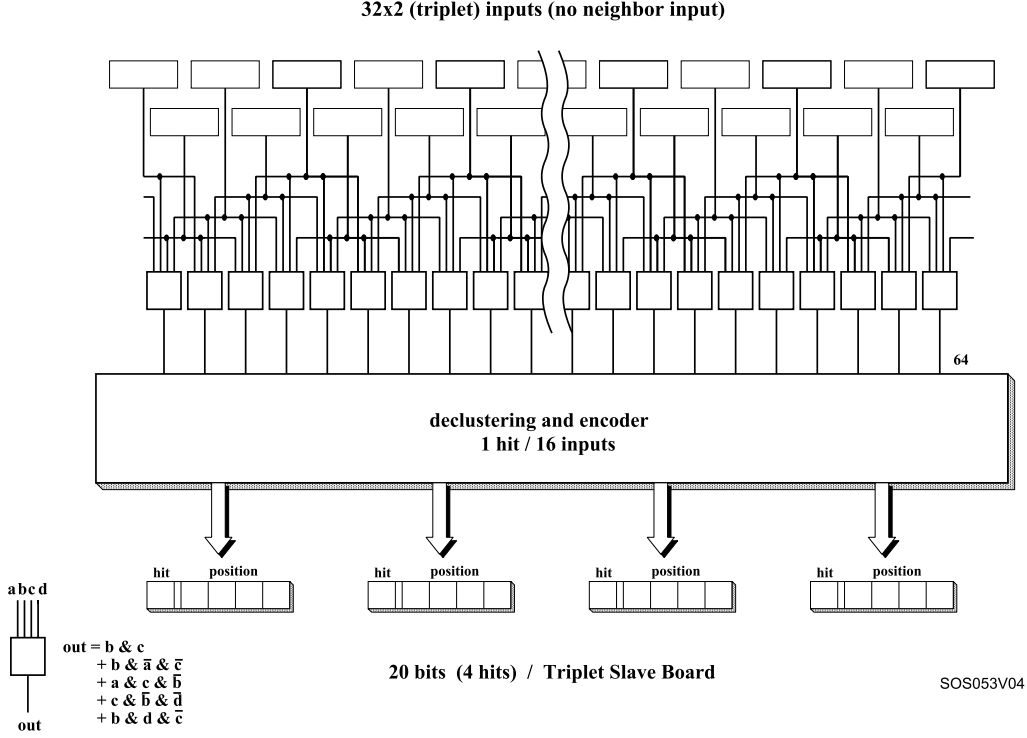


Figure 4.16: The functional structure of the triplet Slave Board for strip signals. Logic to deal with the staggering of triplet layers and output format after the encoder section is also shown.

#### 4.2.5.3 EI/FI Slave Board (EFSB)

The EI/FI Slave Board (EFSB) (Figure 4.17) performs coincidence operations (1-out-of-2) on signals from the EI/FI doublet. The total numbers of the wire signals from an EI TGC doublet unit and an FI TGC doublet unit are 16 and 32 per layer respectively. The total number of the strip signals per layer is 32 for both the EI and FI TGC units. A single EFSB takes care of signals from an EI or an FI doublet.

The EFSB has very similar structure to the TSB, as shown Figure 4.18. The additional functionality of the EFSB is coincidence logic that provides hit-signals to the Sector Logic boards. The Slave Board performs the 1-out-of-2 (or optionally 2-out-of-2) coincidence operation. Since the trigger window size in the EI/FI station is larger than 50 cm (in the bending plane), fine granularity in the provision of hit-signals is not necessary. The segmentation for the EI TGC unit is defined to be two segments in the R-direction and four segments in the  $\phi$ -direction. The FI TGC unit is subdivided into four segments in both the R and  $\phi$ -directions. Each segment provides a hit-signal using the coincidence logic shown in Figure 4.18. The total number of the hit-signals sent to the Sector Logic is 6 bits per the EI TGC doublet and 8 bits per the FI TGC doublet.

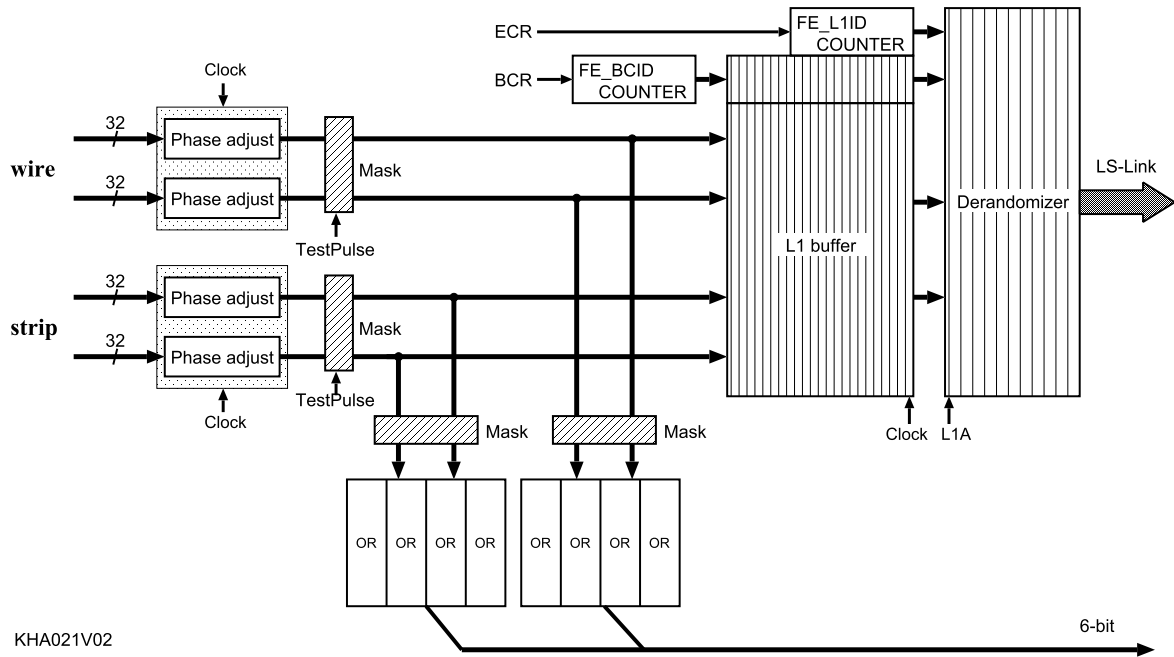


Figure 4.17: Slave Board for the EI/FI TGC doublet.

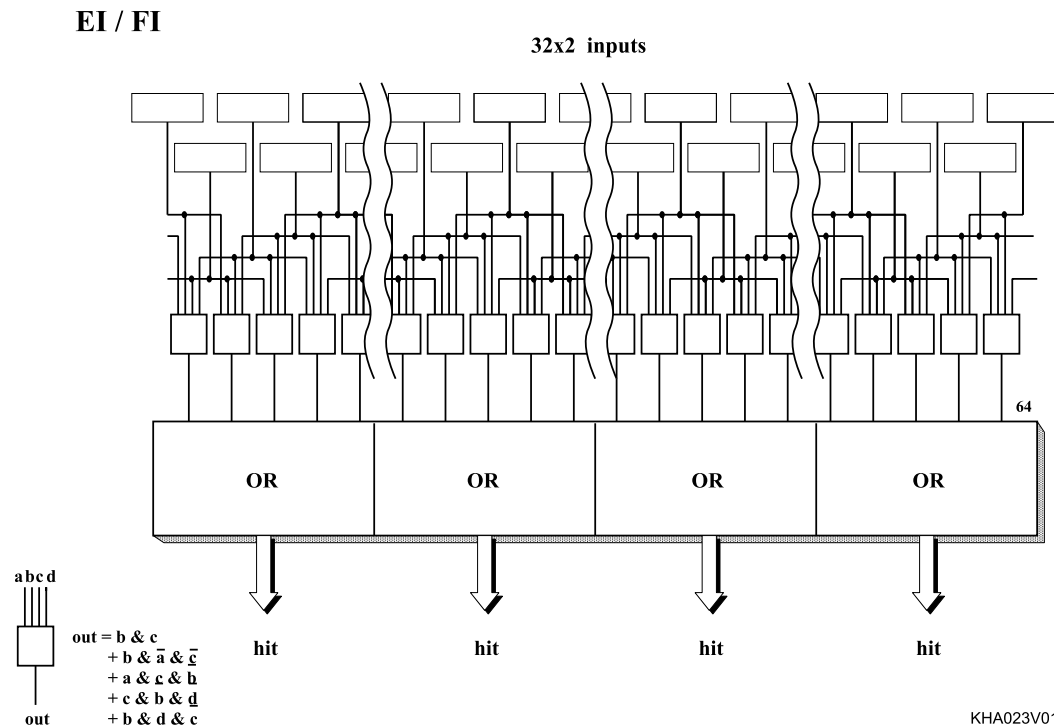


Figure 4.18: The functional structure of the EI/FI Slave Board. Logic to deal with the staggering of doublet layers and output format after the encoder section is also shown.

#### 4.2.6 Readout Block

The schematic diagram of the block is shown in Figure 4.19. The block consists of mainly three sub-blocks, which are the level 1 buffer (L1BUF), derandomizer and the parallel to serial converter (PSC). This block has 15 high-density memory macro cells. The output data are going out from the right side while the input data are arranged on the top side of the memory cell array. The memory allocation is optimized the power consumption and the wire length for fast data processing.

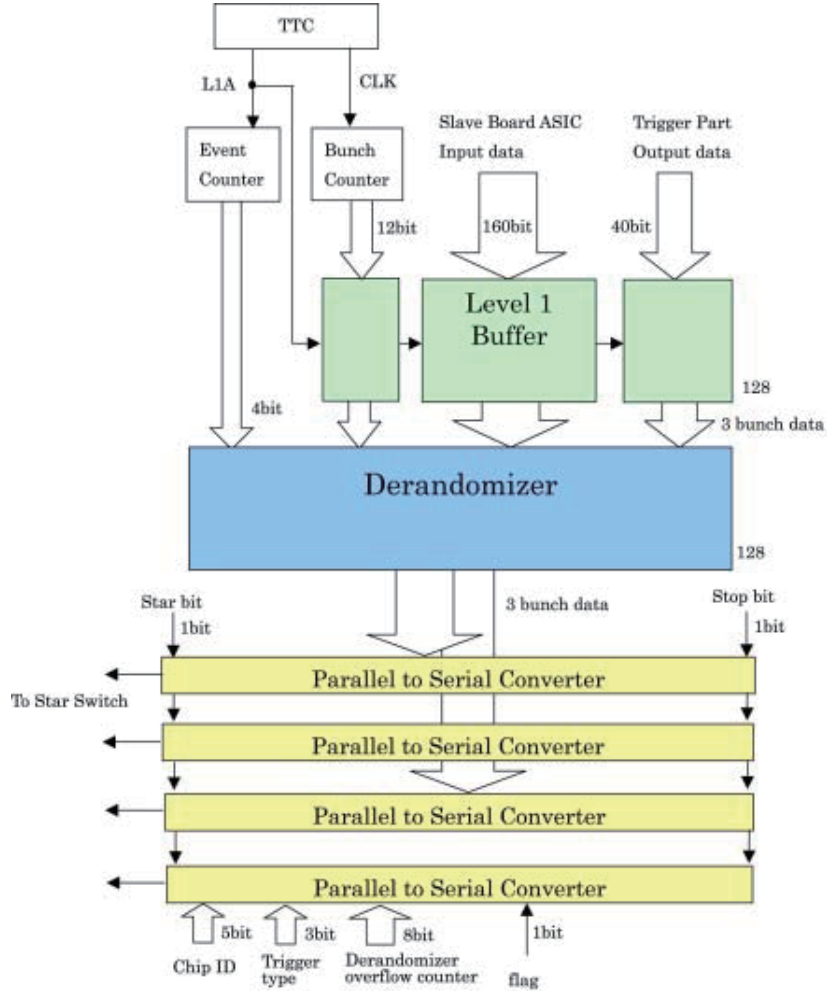


Figure 4.19: Block Diagram of the SLB Readout Block.

The level 1 buffer has a pipe-line structure made with shift-register arrays (212 bit width and 128 bit depth). Among 212 bit, 160 bit is used for the input binary data, 40 bits are for the trigger data, and 12 bits are for bunch crossing ID (Bunch counter, BCID). The raw data must be maintained in L1BUF for maximum  $2.5 \mu\text{s}$ .

If the L1A signal is arrived, the data are put into to the derandomizer at the end of the pipeline together with the event count. The original Data are thus sorted up in the derandomizer with the event counter number (L1ID). At this moment, beside the data associated with

L1A, the data associated with one bunch earlier than L1A and one with one bunch after L1A are also put in the derandomizer FIFO. For taking BCID and L1ID into the hit data bank, we put only the least significant 8 bit of BCID and 4 bit of L1ID into the derandomizer, whereas the original data width of BCID is 12 bit and one of L1ID is 24 bit.

The derandomizer itself is a FIFO structure to buffer the time jitter in the later readout processes. The output data of the three bunches is then sent to three PSCs independently to be serialized and wrapped with start and stop bits. The serialized data are then sent to SSW with LVDS (Low Voltage Differential Signaling) level. [32] [33]

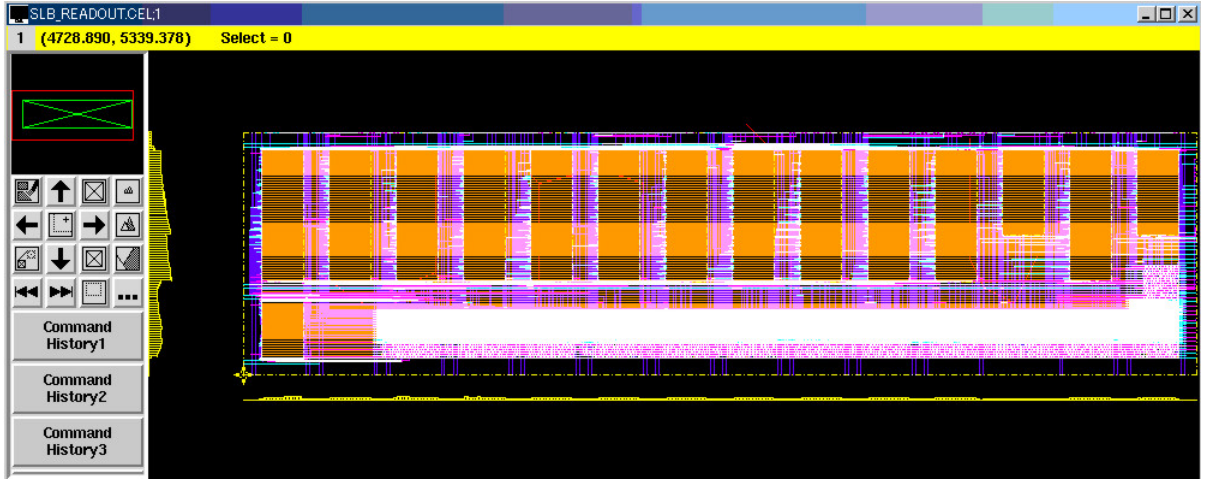


Figure 4.20: Layout of the Readout macro-core. In this figure, aligned rectangles means the location of the memory macro cells.

#### 4.2.7 JTAG Block

The JTAG Standard [34] [35] [36], developed by the Join Test Action Group, is the IEEE 1149.1 Boundary-Scan Standard has been adopted industry-wide. Although JTAG Standard is developed for boundary-scan test such as providing test access on PCB boards and so forth, JTAG is widely used such as in-system flash/PLD programming. The JTAG interface has only four (or five) signals and the JTAG protocol provides standalized register access method. Therefore, we chose the JTAG protocol as an interface to access the SLB registers.

In the SLB ASIC, JTAG standard access port and the boundary scan architecture are also implemented. Each of the trigger matrix outputs (40 bits) and outputs of the readout (4 bits) had kept own boundary scan cell when captured via JTAG. <sup>5</sup>

The SLB ASIC has various internal registers (total 18 different kinds of the registers). The contents of the registers are listed in Table 4.1. These registers formed with the voting logic technique (Figure 4.1).

<sup>5</sup>The inputs (160 bits) do not connect the boundary scan cells.

Table 4.1: Control Registers in SLB ASIC.

Name	Bit	RW	Description
DEPTH	21	RW	Depth of L1Buffer
TESTPULSE	5	RW	Delay of Test pulse Trigger
DELAY	4	RW	No longer used (after version 3)
DELAY_A	4	RW	Delay adjust for block A (form 0 to 3clk with 0.5clk)
DELAY_B	4	RW	Delay adjust for block B (form 0 to 3clk with 0.5clk)
DELAY_C	4	RW	Delay adjust for block C (form 0 to 3clk with 0.5clk)
DELAY_D	4	RW	Delay adjust for block D (form 0 to 3clk with 0.5clk)
SCHEME	1	RW	Coincidence condition 0: 3 out of 4, 1:4 out of 4
L1VETO	1	RW	Level1 Accept (L1A) usage 0:Through,1:supress L1A
CLKINV	1	RW	Clock phase 0: Order, 1:Invert
Reset	1	RW	Reset of Internal ECR and BCR
DRDRST	1	RW	Derandomizer Reset
DCVETO	1	RW	Input data Low Level 0:DC balanced, 1:Normal
SEU	1	RO	SEU flag
MODULE	8	RO	Module type and Module Address
OVERFLOW	8	RO	Counts the number of Derandomizer Overflow was happened.
ID	32	RO	ID=0010_0100_0000_0100_1100_0000_0000_0100
MASK1P	160	RW	Mask Pattern for Readout and Matrix
MASK1	160	RW	Mask Enable for Readout
MASK2P	160	RW	Mask Pattern for Matrix only
MASK2	160	RW	Mask Enable for Matrix only
TPP	160	RW	Test Pulse Pattern

### 4.2.8 Implementation on the ASIC

The functions of the each block are described in Hardware Description Language (HDL). For ASIC development, Verilog HDL is the default language we used.

At first, we verified the described function block has proper functionality using the Verilog Simulator NC-Verilog (Cadence).

Then, the code is converted into gate-level code or net list using Logic Synthesizer Design-Compiler (Synopsys). The gate-level code consists of instantiation of logic cells of the ASIC libraries and the connection information among these logic cells. The gate-level code has equal functionality with original code and can be implemented in the ASIC. At this point, we verified the functionality using the gate-level code.

Finally, Place and Route (P&R) was performed. We used Milkyway and Apollo (Synopsys) P&R software.

P&R consists of following steps:

1. Read in the gate-level code: The gates and connections are registered into the P&R library.
2. Floor Plan: Define the areas for each function block will be located.
3. Gate Placement: The gates of the each function block will be placed automatically using the algorithm that aims to minimize the total length of the circuit connections.
4. Routing: Place the connection wires among the gates. These connections are optimized step-by-step. This step is very important to reduce the propagation delay.
5. Back Annotation: Extract actual delays between each connection. Extracted delay consists of propagation delay and input port charge-up delays ( $= R \times C$ ).<sup>6</sup>

### 4.2.9 Validation

We have tested an ASIC chip on test board to validate full functionality.

Figure 4.21 shows a schematic view of the inspection setup, which consists of a SLB ASIC Test Board (equiped with a 256 pin QFP socket), 6 VME Pulse Pattern Generator (PPG) modules for data feed, 2 FIFO modules for data Readout, a clock generator and so forth.

We prepared test vectors, which simulated the input patterns for the five types of SLB ASIC (WD, WT, SD, ST, EI/FI) when muon tracks pass the TGCs. The input data from PPG modules were fed to the DUT (Device Under Test) chip on the test board, and the output are read out by FIFO modules in synchronous with 40.08 MHz system clock. The output data are compared with test vector outputs. In this test, a universal clock generator is used. TTC signals are provided via PPG (L1A, BCR, ECR), via a clock generator (CLK)

---

<sup>6</sup>Unfortunately some libraries (such as we used) do not have input port capacitance information.

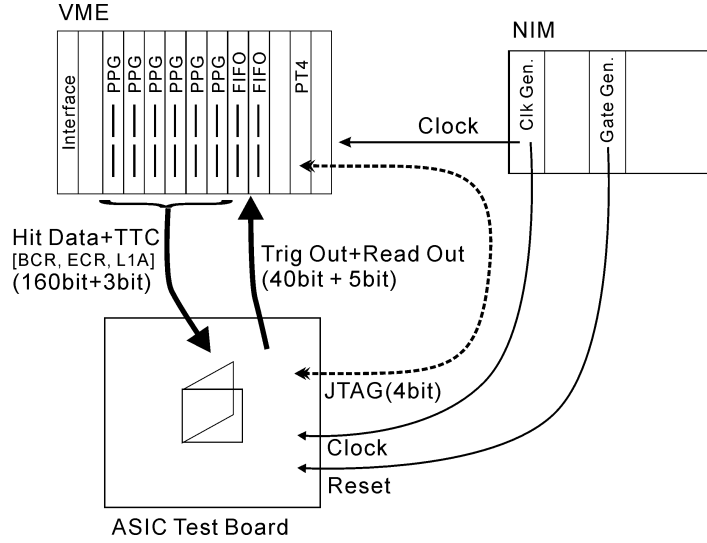


Figure 4.21: A Schematic View of SLB ASIC Test Setup.

and via gate generator (Reset), respectively. Various test vectors data-set (2M Events) listed in Table 4.22 were fed to the DUT ASIC, and outputs from the prototype were found to be correct without any failure.

Therefore, we have justified our design and its implementation. Next, we changed frequency of system clock to check that the ASIC run with adequate timing margin at 40.08 MHz. We have found that it works correctly up to 54 MHz. At higher frequencies, some error events that are inconsistent with the test vector outputs have occurred. From this result, we can conclude that the prototype has at least 6.5 ns timing margin at trigger matrix block.

Readout functionality test has been done with almost same setup with trigger matrix check except a TTC input, L1A, was added. With all the depth at Level-1 Buffer, the output of readout data is correct. Then, we changed system clock frequency and have found that it works correctly up to 69 MHz. At higher frequencies, some readout bits are different with the input data. From this result, we can conclude that the prototype has at least 10.5 ns timing margin at readout block.

All the functionality configured by JTAG registers (cf. Table 4.1) including Input block Masks and Delays has been also verified and found all functionality works well.

Figure 4.22: Various SLB Test Vectors and Results.

Trigger Type	Tracks/event	Scheme	# of Error
Wire Doublet (WD)	1track	3 out of 4	0
		4 out of 4	0
	2tracks	3 out of 4	0
		4 out of 4	0
	3tracks	3 out of 4	0
		4 out of 4	0
Sire Doublet (SD)	1track	3 out of 4	0
		4 out of 4	0
	2tracks	3 out of 4	0
		4 out of 4	0
	3tracks	3 out of 4	0
		4 out of 4	0
Wire Triplet (WT)	1track	2 out of 3	0
		3 out of 3	0
	2tracks	2 out of 3	0
		3 out of 3	0
	3tracks	2 out of 3	0
		3 out of 3	0
Strip Triplet (ST)	1track	1 out of 2	0
		2 out of 2	0
	2tracks	1 out of 2	0
		2 out of 2	0
	3tracks	1 out of 2	0
		2 out of 2	0
EI/FI	1track	1 out of 2	0
		2 out of 2	0
	2tracks	1 out of 2	0
		2 out of 2	0
	3tracks	1 out of 2	0
		2 out of 2	0

## 4.3 Sector Logic

The Sector Logic is the final part of ATLAS TGC muon Trigger system. One Sector Logic covers one trigger sector (shown in Figure 3.4 in Section 3.3.). In each 25 ns bunch crossing, the Sector Logic receives track information of wires ( $\Delta R$ ) and strips ( $\Delta\phi$ ) from High- $p_T$  modules. To get transverse momentum ( $p_T$ ) of muon tracks, the Sector Logic combines both inputs. Then, it chooses the two highest- $p_T$  tracks in each trigger sector. Resulting trigger information including  $p_T$  and RoI location are sent to the MUCTPI.

### 4.3.1 Overview

Requirements for the track selection in the Sector Logic are:

1. Both transverse momentum and hit position on the pivot plane of the TGC should be reconstructed from hit information of wires and strips from the High- $p_T$  modules.
2. Information of the innermost TGCs (EI/FI stations) should be used for track finding to suppress fake tracks and low momentum background tracks.
3. Muons with more than 6 GeV/c  $p_T$  from the interaction point should be accepted.
4. Accepted muon tracks should be classified into six groups based on  $p_T$  information. These 6  $p_T$  thresholds should be programmable.
5. Up to 2 highest- $p_T$  tracks are chosen in each trigger sector. These track information including  $p_T$  and RoI location should be sent to the MUCTPI.
6. Track finding should be applied to each beam crossing. (i.e. These circuitry are implemented with dead time less logic)

The Sector Logic is also equipped with a Level-1 Readout Buffer. The High- $p_T$  module outputs and the Sector Logic output thus are included in the Readout data flow in the same way as the chamber data. This information from the Sector Logic will play important role in diagnosis of the trigger system as well as in checking trigger performance.

### 4.3.2 Design of the Sector Logic

A schematic of the Sector Logic is shown in Figure 4.23. The Sector Logic consists of Decoder,  $R$ - $\phi$  coincidence matrices, Track Selection logic and Encoder. The logic operates in pipeline mode at 40.08 MHz.

The Sector Logic receives hit information of wires and strips from each High- $p_T$  module in one trigger sector (cf. Figure 3.4 in Section 3.3). In order to get transverse momentum of tracks, it combines both inputs and then classifies muon tracks into six levels ( $R$ - $\phi$  Coincidence).

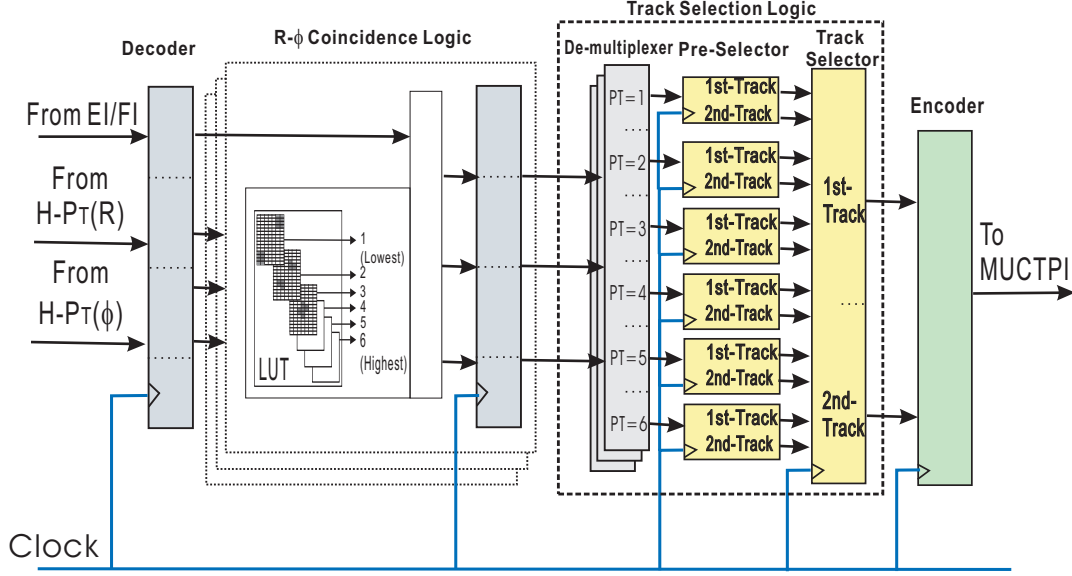


Figure 4.23: Block Diagram of Sector Logic (trigger logic functional view).

This  $R\text{-}\phi$  coincidence is performed by Look-Up Table (LUT) method with FPGA embedded memory. In addition, hit information of EI/FI TGC chambers from the Slave boards is used to suppress fake hits and low momentum background tracks. The innermost TGC (EI/FI stations) covers only ENDCAP Region.

The output of  $R\text{-}\phi$  coincidence is fed to Track Selection Logic. The two highest  $p_T$  tracks are chosen in each trigger sector. Encoder block receives them, formats them into 32-bit format, and transmits them to MUCTPI in LVDS signal. There are 144 Sector Logic modules in total for the TGC system, which will be located in USA15.

The Sector Logic is also equipped with SLB (Slave Board) ASIC as a Level-1 Readout Buffer. The High- $p_T$  module outputs and the Sector Logic output are sent to the TGC ROD via a Star Switch module.

#### 4.3.2.1 $R\text{-}\phi$ coincidence

The Sector Logic adopts LUT for the  $R\text{-}\phi$  coincidence, where the  $\Delta R$  information and the  $\Delta\phi$  information from the High- $p_T$  Boards are combined to get  $p_T$  information of the muon track.

To implement LUTs in FPGA embedded memory (Block selectRAM in Xilinx FPGA), one sector is divided into small blocks called SSCs (Sub Sector Clusters). Figure 4.24 shows one SSC which consists of 8 sub-sectors (2 rows of wire by 4 columns of strips). Due to the specification of High- $p_T$  coincidence, one SSC includes a maximum of one hit in  $R$  and two hits in  $\phi$ . In one SSC, two sub-coincidences (denoted as half SSC) are performed in parallel:  $(\phi_0 \times R)$  and  $(\phi_1 \times R)$ . Each hit information is 13bit and is used as the each LUT address. If an  $R\text{-}\phi$  coincided track is found, the LUT outputs 4 bits in width (1bit as charge of muon, 3bits as  $p_T$  value classified in 6  $p_T$  levels) and local position in the half SSC. If both half SSC

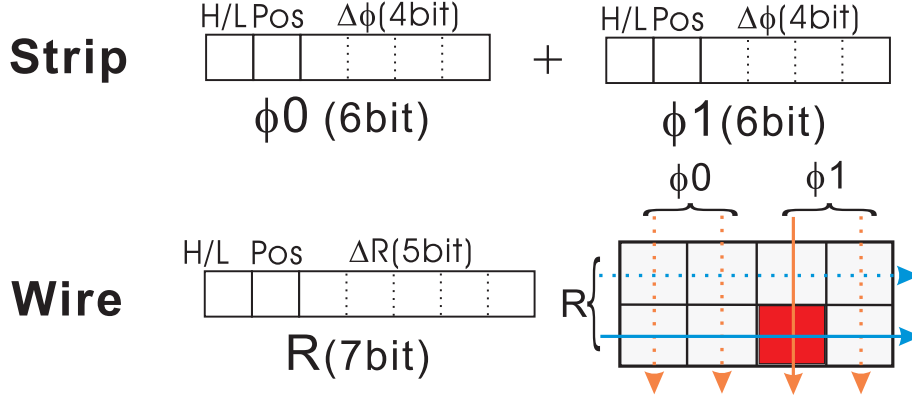


Figure 4.24: Detail of Sub Sector Cluster (SSC) for the R- $\phi$  coincidence together with hit inputs.

has candidates, higher  $p_T$  level candidate is chosen as the SSC output. In case both candidates has same  $p_T$  level, the candidate in the lower- $\phi$  half SSC is chosen. Finally, the track position information of the sector (RoI) is added.

Each ENDCAP trigger sector covers 37 rows of wire by 4 columns of strips. To cover this, 19 SSCs are needed. However, SSCs on chamber boundaries should be treated as two different SSC from the viewpoint of the R- $\phi$  coincidence. Therefore, 23 SSCs are needed in one ENDCAP trigger sector.

#### 4.3.2.2 Track Selection Logic (Pre-Track Selector, Track Selector)

Track Selection logic block consists of 6 pre-track selectors, and a track selector. Figure 4.25 shows schematics of Track selection logic block.

Track candidates from R- $\phi$  Coincidence are sent to the Pre-Track Selectors. Each Pre-Track Selector unit collects tracks with the same  $p_T$  level and selects 2 tracks with the 1st and 2nd lower (higher R). There are 6 identical Pre-Track selector units corresponding to 6 levels of track  $p_T$ . The output from the Pre-Track selector includes position information of triggered sub-sector.

The Track Selector unit picks up the final 2 highest- $p_T$  tracks among 12 tracks from 6 Pre-Track Selectors. The output from the Track Selector is a combination of position information (RoI number), charge sign of track, and 6 levels of  $p_T$  information.

#### 4.3.2.3 Decoder

Each High- $p_T$  ASIC chip chooses up to two hits and outputs them in 20 bit format. The High- $p_T$  ASIC can be configured for wire or strip by setting configuration pin. Figure 4.26 shows each High- $p_T$  ASIC outputs.

Figure 4.27 shows the connection between wire High- $p_T$  Boards and Sector Logic. As shown in this Figure, four High- $p_T$  ASICs cover in an ENDCAP trigger sector and two High- $p_T$  ASICs

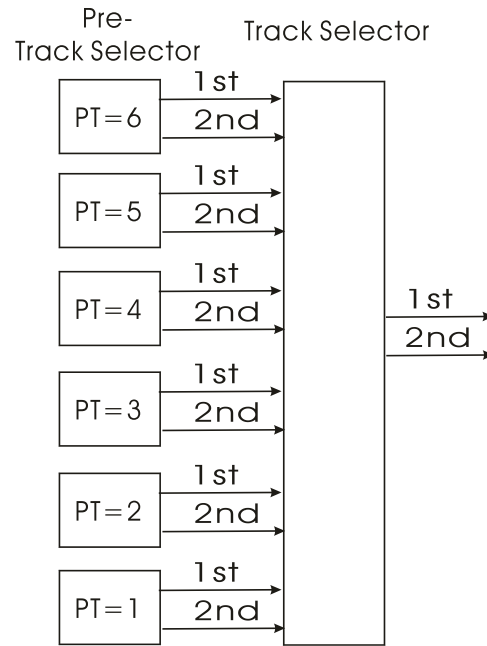


Figure 4.25: A schematic of Track Selection logic block.

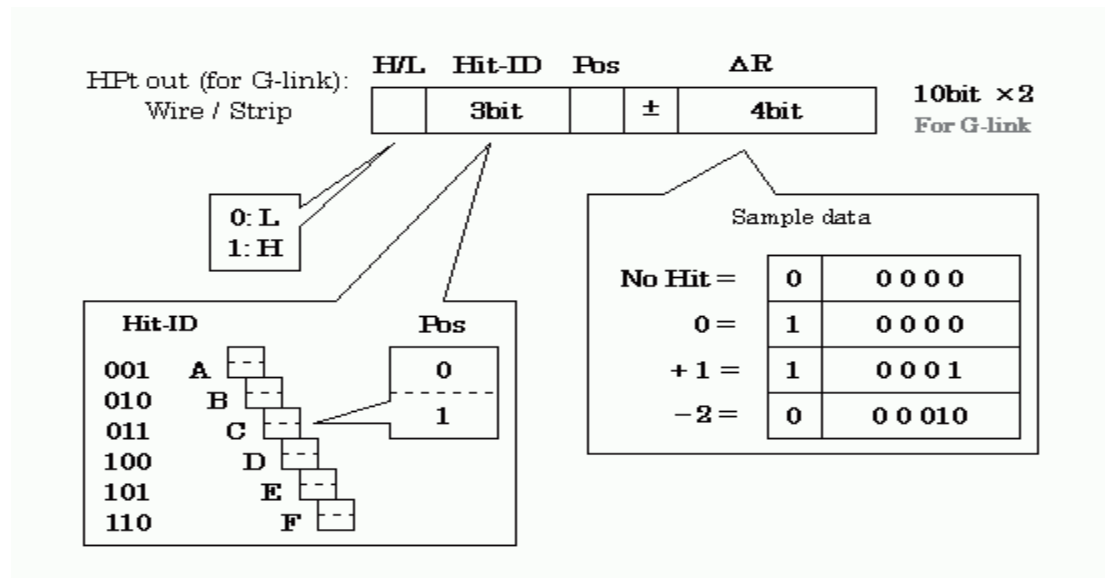


Figure 4.26: Data Format from Hi-p<sub>T</sub> ASIC chip (Wire mode).

cover in an ENDCAP trigger sector. The signal format between High- $p_T$  Boards and a Sector Logic Board is defined in “HPT Board g-link connection table” [17].

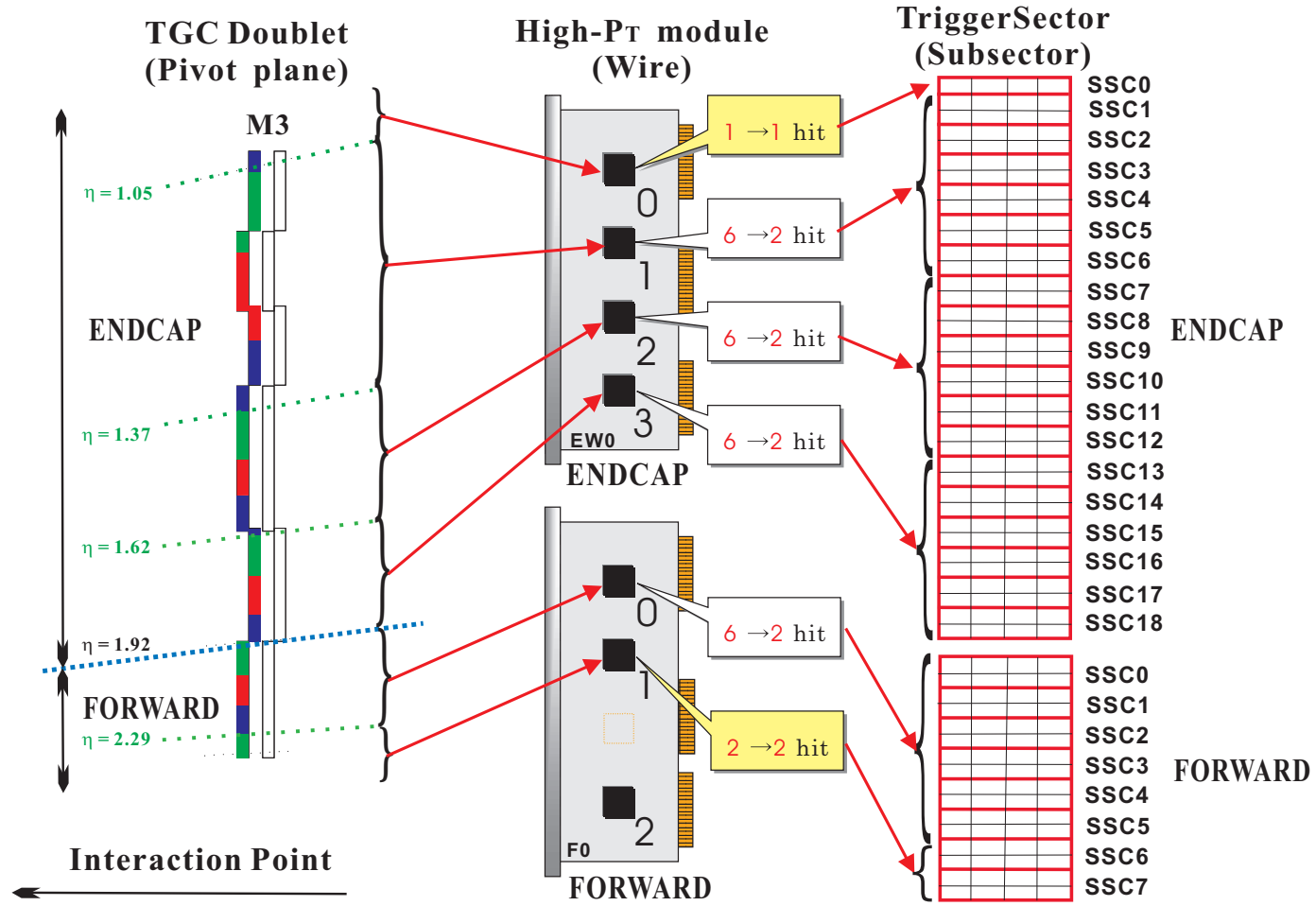


Figure 4.27: Wire High- $p_T$  Boards coverage and its correspondent SSCs.

**\*Wire (R) Signal:** Wire (R) hit signal consists of  $\Delta R$  information with a sign bit( $\Delta R$ : 1+4 bits), a bit for discriminating between Low- $p_T$  coincidence and High- $p_T$  coincidence (H/L), position information of R (HitID+POS: 3+1 bits).

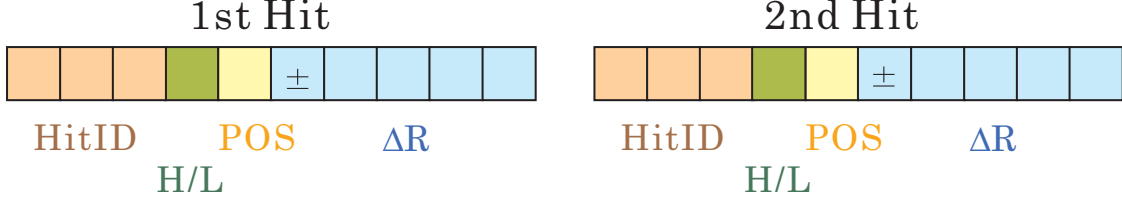


Figure 4.28: Wire (R) input signal from from Wire High- $p_T$  Board.

**ENDCAP Region:** Wire signals for ENDCAP Region sector are covered by four High- $p_T$  ASICs. In Decoder block in ENDCAP Region Sector Logic, SSC# (Sub Sector Cluster Number) are generated from HitID as:

High- $p_T$ ASIC	SSC#
EW0-Chip0	SSC# = HitID
EW0-Chip1	SSC# = HitID + 1
EW0-Chip2	SSC# = HitID + 7
EW0-Chip3	SSC# = HitID + 13

The following table shows correspondances each High- $p_T$  ASIC, its cover region and SSC#.

High- $p_T$ ASIC	$\eta$	SLB ASIC	SSC#	HitID	Max Hit
EW0-Chip0	-1.05	EWD0 EWT0	0	0	1 $\rightarrow$ 1
EW0-Chip1	1.05-1.37	EWD1 EWT1	1 2	0 1	6 $\rightarrow$ 2
		EWD2	3 4	2 3	
		EWD3 EWT2	5 6	4 5	
EW0-Chip2	1.37-1.62	EWD4 EWT3	7 8	0 1	6 $\rightarrow$ 2
		EWD5	9 10	2 3	
		EWD6 EWT4	11 12	4 5	
EW0-Chip3	1.62-1.92	EWD7 EWT5	13 14	0 1	6 $\rightarrow$ 2
		EWD8	15 16	2 3	
		EWD9 EWT6	17 18	4 5	

**FORWARD Region:** Wire signals for FORWARD Region sector are covered by two High- $p_T$  ASICs. In Decoder block in FORWARD Region Sector Logic, SSC# (Sub Sector Cluster Number) are generated from HitID as:

High- $p_T$ ASIC	SSC#
FW0-Chip0	SSC# = HitID
FW0-Chip1	SSC# = HitID + 6

The following table shows correspondances each High- $p_T$  ASIC, its cover region and SSC#.

High- $p_T$ ASIC	$\eta$	SLB ASIC	SSC#	HitID	Max Hit
FW0-Chip0	1.92-2.29	FWD0 FWT0	0 1	0 1	6 $\rightarrow$ 2
		FWD1	2 3	2 3	
		FWD2 FWT1	4 5	4 5	
FW0-Chip1	2.29-	FWD3 FWT2	6 7	0 1	2 $\rightarrow$ 2

**\*Strip ( $\phi$ ) Signal:** Strip ( $\phi$ ) hit signal consists of  $\Delta\phi$  information with a sign bit ( $\Delta\phi$ : 1+3 bits), a bit for discriminating between Low- $p_T$  coincidence and High- $p_T$  coincidence (H/L), position information of  $\phi$  (HitID+POS: 3+1 bits). Unused 4th bit of  $\Delta\phi$  information is set to “0”.

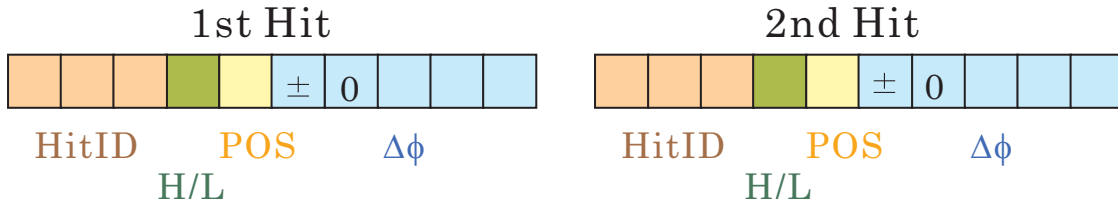


Figure 4.29: Strip ( $\phi$ ) input signal from from Strip High- $p_T$  Board.

**ENDCAP Region:** Strip signals for ENDCAP Region sector are covered by two High- $p_T$  ASICs. In Decoder block in ENDCAP Region Sector Logic, TGC (Pivot Chamber) ID and hit position in  $\phi$  are calculated from HitID and POS as:

ES0-Chip0				
HitID	Pivot Chamber	$\phi$		
		POS=0	POS=1	
0	M3-E5 (T9)	0	1	
1	M3-E5 (T9)	2	3	
2	M3-E4 (T8)	0	1	
3	M3-E4 (T8)	2	3	

ES0-Chip1				
HitID	Pivot Chamber	$\phi$		
		POS=0	POS=1	
0	M3-E3 (T7)	0	1	
1	M3-E3 (T7)	2	3	
2	M3-E2 (T6)	0	1	
3	M3-E2 (T6)	2	3	
4	M3-E1 (T5)	0	1	
5	M3-E1 (T5)	2	3	

The following table shows correspondances each High- $p_T$  ASIC, its cover region and SSC#.

High- $p_T$ ASIC	SLB ASIC	Pivot Chamber	HitID	SSC#	Max Hit
ES0-Chip0	ESD0 EST0	M3-E5	0 1	00-02	4 $\rightarrow$ 2
	EWD1	M3-E4	2 3	02-04	
ES0-Chip1	ESD2	M3-E3	0 1	04-06	6 $\rightarrow$ 2
	EWD3 EST1	M3-E2	2 3	06-12	
	EWD4	M3-E1	4 5	12-18	

In case of Strip input, more than 1 SSC correspond to each HitID. For example, a hit from High- $p_T$  (ES0-Chip0) with HitID=0 is fet to 3 SSCs (SSC#=0, 1, 2).

Since SSCs on chamber boundaries should be treated properly, SSC#=02, 04, 06, 12 appear in two column. These SSCs are treated as two different SSCs for each chamber's Strip input.

**FORWARD Region:** Strip signals for FORWARD Region sector are covered by one High- $p_T$  ASIC. In Decoder block in FORWARD Region Sector Logic, TGC (Pivot Chamber) ID and hit position in  $\phi$  are calculated from HitID and POS as:

FS0-Chip2			
HitID	Pivot Chamber	$\phi$	
		POS=0	POS=1
0	M3-F (T2)	0	1
1	M3-F (T2)	2	3

The following table shows correspondances each High- $p_T$  ASIC, its cover region and SSC#.

High- $p_T$ ASIC	SLB ASIC	Pivot Chamber	HitID	SSC#	Max Hit
FS0-Chip2	FSD0 FST0	M3-F	0 1	00-15	2 $\rightarrow$ 2

In case of FORWARD region Strip input, these inputs are fed to all SSCs. Since there is only one chamber in FORWARD Region, special treatment for chamber overlap isn't required.

#### 4.3.2.4 Encoder

The Encoder block of the Sector Logic sends resulting trigger information of 2 highest- $p_T$  tracks in the Sector to feed it to the MUCTPI.

TGC Sector Logic formats its output in 32-bit format, and transmits them to MUCTPI in LVDS signal. The format is shown in Table 4.2.

Table 4.2: Data format between Sector Logic and MUCTPI [16].

Bit#	Meaning	ENDCAP	FORWARD
0	> 2 candidates in the sector		
1	ROI1 with overlap flags	ROI1[0]	ROI1[0]
2		ROI1[1]	ROI1[1]
3		ROI1[2]	ROI1[2]
4		ROI1[3]	ROI1[3]
5		ROI1[4]	ROI1[4]
6		ROI1[5]	ROI1[5]
7		ROI1[6]	res
8		ROI1[7]	res
9		OVL1 (Note1)	res
10	ROI2 with overlap flags	ROI2[0]	ROI2[0]
11		ROI2[1]	ROI2[1]
12		ROI2[2]	ROI2[2]
13		ROI2[3]	ROI2[3]
14		ROI2[4]	ROI2[4]
15		ROI2[5]	ROI2[5]
16		ROI2[6]	res
17		ROI2[7]	res
18		OVL2 (Note1)	res
19	p <sub>T</sub> 1[0] (Note2)		
20	p <sub>T</sub> 1[1]		
21	p <sub>T</sub> 1[2]		
22	p <sub>T</sub> 2[0] (Note2)		
23	p <sub>T</sub> 2[1]		
24	p <sub>T</sub> 2[2]		
25	> 1 candidate in ROI1 (Note3)	res	res
26	> 1 candidate in ROI2 (Note3)	res	res
27	BCID[0] (Note4)		
28	BCID[1]		
29	BCID[2]		
30	Candidate1 sign (Note5)		
31	Candidate2 sign (Note5)		

**Note1.** OVLi[1..0]

- 00:** No overlap
- 01:** Overlap in  $\phi$
- 10:** Overlap in  $\eta$
- 11:** Overlap in  $\phi$  and  $\eta$

**Note2.** pTi[2..0]

- 000:** Low p<sub>T</sub> 1 (Lowest p<sub>T</sub>)
- 001:** Low p<sub>T</sub> 2
- 010:** Low p<sub>T</sub> 3
- 011:** High p<sub>T</sub> 1
- 100:** High p<sub>T</sub> 2
- 101:** High p<sub>T</sub> 3 (Highest p<sub>T</sub>)
- 111:** No Candidate
- 000:** Reserved

**Note3.** This bit field is for Barrel Muon Trigger system (RPC) only. TGC Electronics cannot tell >1 candidate in a RoI.

**Note4.** Three bits for the BCID should be enough for checking purpose as it is very unlikely to have a misalignment greater than 8 BC. They are the low order bits of the BCID provided by the TTC system (TTCrx receiver chips or equivalent).

**Note5.** Candidate sign

- 0:** Negative ( $\mu^-$ )
- 1:** Positive ( $\mu^+$ )

The double counting in the ENDCAP-FORWARD overlap region can be removed by cutting the edge of strips of the pivot chambers in the FORWARD Region, so as not to make a coincidence in  $\phi$  projection. Therefore, the MUCTPI does not need to take care and there is no overlap bit in the output for the FORWARD Region Sector Logic.

The MUCTPI receives TGC Sector Logic outputs and RPC Sector Logic outputs. It solves overlap problem between TGC and RPC, mentioned in Section 2.1.1, and then calculates overall multiplicities of muon tracks for six muon threshold levels.

The latest interface definition including Table 4.2 and strategy for solving the overlap problem are described in the official document; “Interface & overlaps in the LVL1 muon trigger system” [16].

### 4.3.3 The first prototype (Prototype-0)

In this section, first implementaion of the Sector Logic Prototype-0 (SLP0) and its functional check are described. A photograph is shown in Figure 4.30.

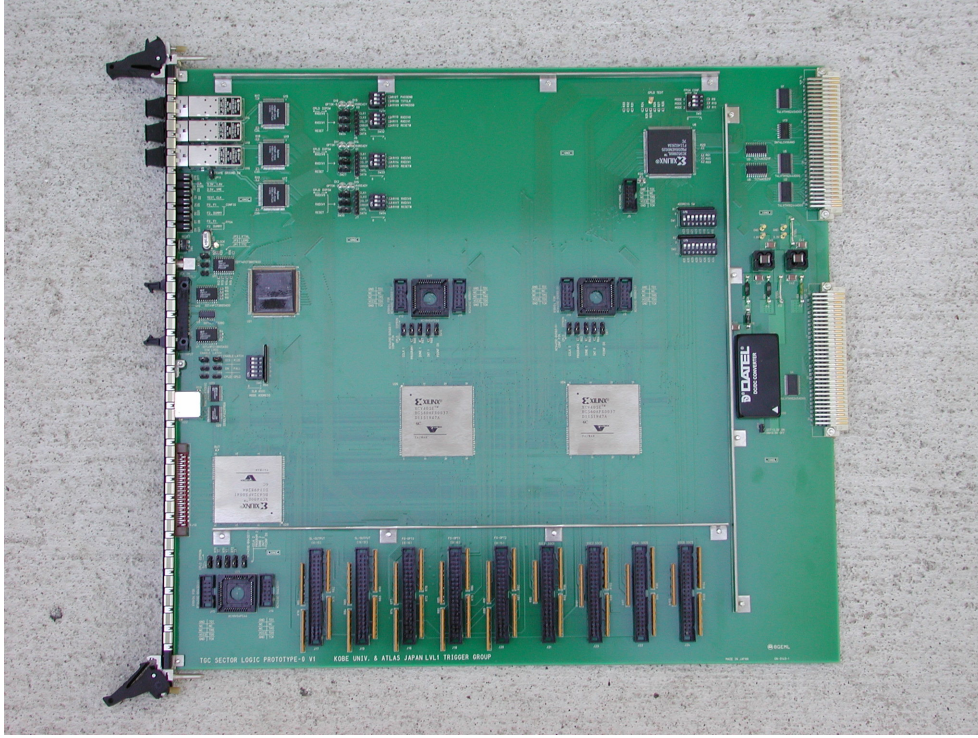


Figure 4.30: A Photograph of TGC Sector Logic Prototype-0 (top view).

#### 4.3.3.1 Specification

The SLP0 module is FORWARD Region (cf. Figure 3.1) type.

**Mechanical Standard:** This SLP0 is a 9U VME64x module of single width. It equips 160pin (5rows) J1 and J2 connectors, and a front panel with EMD shield and injector/extractor handles with locking feature.

**VME Capabilities:** This SLP0 module can be used as a VME64x A32D32 slave module and responds to the AM codes 0F, 0E, 0D, 0B, 0A and 09. However, slot geographical addressing is not supported. It covers 2K Byte (in 32bit-addressed space). The high-byte address (A32-A16) of the SLP0 module can be chosen using DIP switch.

**Input signal from High- $p_T$  module:** The signals from the High- $p_T$  modules comes using three links of serialized optical signal (Multi-mode, 850 nm) with LC connector. The EO/OE converter used in both High- $p_T$  and SL module is V23818-K305-L57 (Infineon). The data format of this connection is described in [17].

**Output signals for MUCTPI:** The signals transmits to the MUCTPI are 32-bit format LVDS signals. A 68-pin half pitch connector (8931E-068-178L (KEL)) is equipped.

**Input signal for TTC distributor:** The signal level for TTC is LVDS. The SLP0 inputs 4 TTC signals (BC (Des1), BCR, ECR, L1A) from TTC distributor with a 20-pin flat cable connector.

**Input and Output signals for Readout:** A SLB ASIC is mounted for Readout of input and output signals of the Sector Logic. The trigger matrix feature of SLB ASIC is disabled. The Readout output signals are converted into serialized LVDS signal with LVDS serializer (DS92LV1023TMSA). A RJ-45 connector is equipped for the cable to Star Switch (SSW).

#### 4.3.3.2 Implementaion

The core function blocks of the Sector Logic are divided two stages and each stage is implemented in the FPGA device(s) respectively. The block diagram is shown in Figure 4.31.

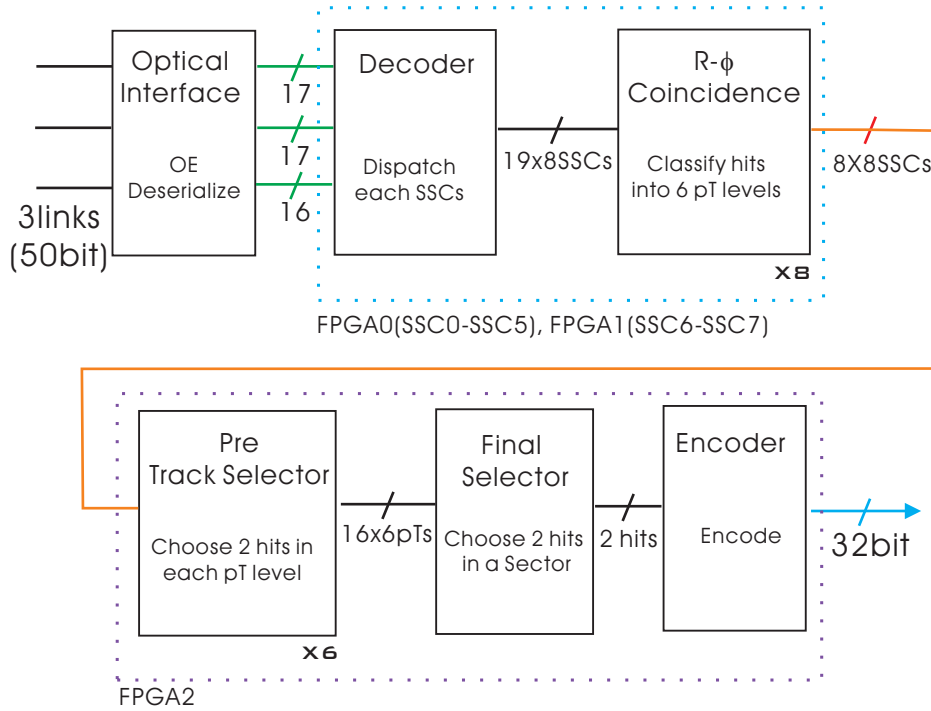


Figure 4.31: Block Diagram of Sector Logic Prototype-0 (FORWARD Region type).

At first stage, decoder block and R- $\phi$  Coincidence block are implemented. The decoder block inputs the R- and  $\phi$ - High- $p_T$  outputs and rearrange them into each SSC inputs. The R- $\phi$  Coincidence block uses FPGA embedded memory (Block SelectRAM) as LUT memory for each SSCs. In order to implement R- $\phi$  Coincidence, we choose extended memory type of

the Xilinx Virtex-E EM series FPGA [37] (XCV405E (Block SelectRAM bits: 560KByte)). FPGA0 covers from SSC0 to SSC5 and FPGA1 covers SSC6 and SSC7.

At second stage, Track Selection Logic (Pre-Track Selector and Track Selector) and Encoder are implemented. The Encoder receives two track candidates from the Track Selection Logic and formats them into for MUCTPI output format [16]. This block is implemented in one Xilinx Virtex-E FPGA [37] (XCV400E) named as FPGA2.

#### **4.3.3.3 Validation**

First, we have tested the Prototype-0 board to validate the Sector Logic design. We prepared test vectors, which simulated the input patterns for the Sector Logic when muon tracks pass the TGCs. Series of input data were fed to the prototype through an optical interface module with the serializer (G-Link), which was specially made for this test. The output to the MUCTPI was read out. The input and the output were synchronized to 40.08 MHz system clock. In this test, a universal clock generator was used. The latency from the G-Link input to the trigger output was found to be 6 clocks as expected from the design. The prototype was tested for over 1M events and outputs were found to be correct without any failure. Therefore, we have justified our design and its implementation for the prototype. Next, we changed system clock frequency to check that the prototype board runs with adequate timing margin at 40.08 MHz. We have found that it worked correctly up to 51.5 MHz. At higher frequencies, we have found problems on the links between receivers on the prototype and transmitters on the optical serializer module. From this result, we can conclude that the prototype has at least 5.5 ns timing margin.

#### **4.3.3.4 Integration test with the MUCTPI**

As explained in section 4.3.2.4, the link between the Sector Logic and the MUCTPI employs 32-bit width LVDS. Timing alignment issues and data integrity through the link were tested to check the trigger data transmission from the Sector Logic to the MUCTPI. The FPGA design of the Sector Logic Prototype-0 was once configured so that test pattern data words loaded in registers were sent to the MUCTPI. The encoder and driver parts of the FPGA design were un-changed from the original design. There was no bit error occurred during 109 events trigger data transmission. Details of these tests are reported in [19].

#### **4.3.3.5 Test beam at H8 beam line in CERN**

We have tested whole TGC electronics system with MUCTPI and CTP using muon beam at H8 experimental area of CERN SPS in 2003 [30], [31]. Configuration of TGC electronics system is same as a part of forward region and we used Prototype-0 as a Sector Logic for Forward region. Whole system worked well and the Sector Logic successfully issued trigger words to MUCTPI. We checked consistency between trigger data in SLB ASIC on the Sector Logic through the

TGC ROD and data received by MUCTPI through the MIROD. Figure 4.32 shows correlation plots of  $p_T$  levels and ROI location. We observed 0.2% inconsistencies out of about 2M events. But no errors were found in the Sector Logic functionalities and it might be caused by timing synchronization in the readout path.

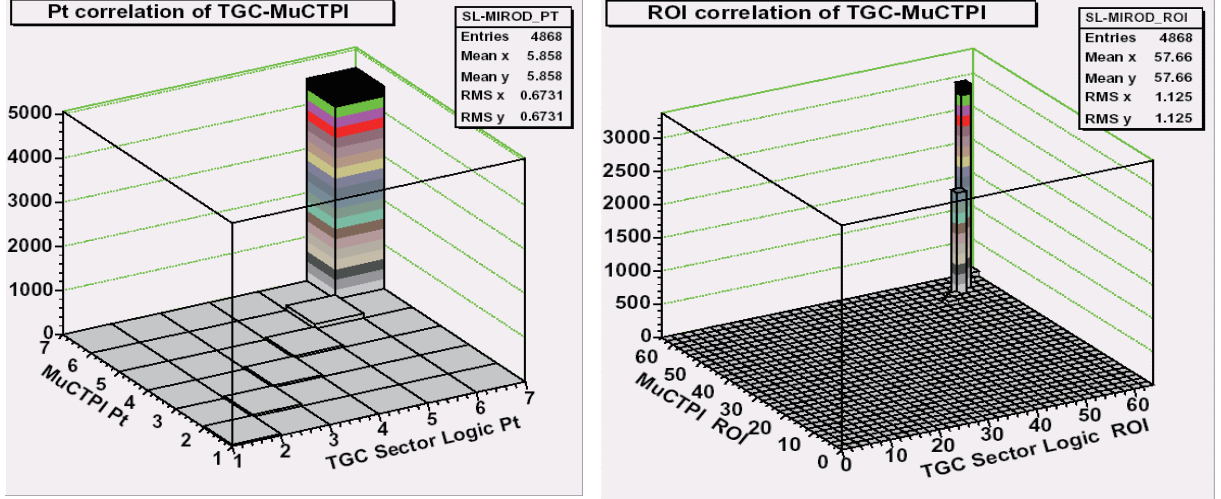


Figure 4.32: Correlation plots of  $p_T$  levels (left) and ROI location(right) for trigger words read out by Sector Logic vs MUCTPI.

#### 4.3.4 Final Design of whole Sector Logic system

As described in the previous section, the design and its functionality of the TGC Sector Logic have been verified using its prototype (SLP0).

Then, we began to design entire TGC Sector Logic system. In this section, the Sector Logic system and each component are described.

Figure 4.33 shows whole TGC Sector Logic system. The TGC Sector Logic system consists of following components:

1. FORWARD Sector Logic: 48 Sectors/System (24 Sectors/Side)

In final design, two Sector Logics are implemented in a FORWARD Sector Logic board. Therefore, there are 24 FORWARD Sector Logic boards in the System and they are stored in two 9Ux400mm VME64x crates.

2. ENDCAP Sector Logic: 96 Sectors/System (48 Sectors/Side)

The ENDCAP Sector Logic also implements two Sector Logics in a board. Therefore, there are 48 ENDCAP Sector Logic boards in the System and they are stored in four 9Ux400mm VME64x crates.

3. TTC Fanout:

For Sector Logic, the following signals are distributed: Clock, BCR (Bunch ID Clear),

76

ECR (Event ID Clear), L1A (Level-1 Trigger Accept) and Reset. The Service Patch-Panel for PS-Boards can be used for the Sector Logic TTC Fanout by setting on-board jumper pin.

4. EI/FI Optical Fanout module: 96 Optical links/System (48 optical links/Side)  
Hit signals from EI/FI PS-Boards are should be distributed to appropriate ENDCAP Sector Logic boards (up to four boards). We designed six channels 1:4 Fanout Optical Fanout Modules, which can be stored in HSC crate (without VME access). There are total 8 Optical Fanout modules in the system.
5. SSW Module:  
A SSW Module equips 10 inputs. One TGC Side can be covered 4 SSW modules (12 FORWARD Sector Logic boards and 24 ENDCAP Sector Logic boards). The output from the SSW module is sent to the ROD module.
6. HSC Crate and HSC module: 2 Crates/System (1 Crate/Side)  
A HSC Crate covers one TGC Side and stores 4 EI/FI Optical Fanout modules, 4 SSW modules and a HSC module.

#### 4.3.4.1 Final Design of Sector Logic board

In this section, the specification of the final design Sector Logic board is described.

The final design is developed with latest FPGA devices at the design time, this gives following merits:

- Three FPGAs in SLP0 is integrated in one FPGA.
- Two Sector Logics are implemented in one board. (i.e. One board covers two trigger sector.)
- In addition the final design Sector Logic board has more timing margins and its cost is cheaper than the SLP0 since FPGA has been improved very much in these years.

**Main FPGA:** We chose Xilinx Virtex-II FPGA [37] for Sector Logic implementation. The Virtex-II FPGA has 18 Kbit Block SelectRAMs in the device. 4 Block SelectRAM is required to implement a LUT for one SSC.

- FORWARD Sector Logic:  
There are 8 SSCs in FORWARD Sector and requires  $8 \times 4=32$  Block SelectRAMs. We selected XC2V1000, which have 40 Block SelectRAMs.
- ENDCAP Sector Logic:  
There are 23 SSCs in ENDCAP Sector and requires  $23 \times 4=92$  Block SelectRAMs. We selected XC2V3000, which have 96 Block SelectRAMs.

**VME Control CPLD:** For VME control and interface, we chose Xilinx CoolRunner-II CPLD, XC2S256-PQ208C. This CPLD provides following features: VME access, FPGA programming from VME, EPROM writing by JTAG protocol and JTAG controller.

**Input signal from high- $p_T$  modules and EI/FI Optical Fanout module:** These signals are serialized optical signal (Multi-mode, 850 nm with LC connector).

- **FORWARD Sector Logic:**

The signals received from the High- $p_T$  modules are 3 links times 2 sector. 6 EO/OE converters (V23818-K305-L57, Infineon) are used. We selected XC2V1000, which have 40 Block SelectRAMs.

- **ENDCAP Sector Logic:**

The signals received from the High- $p_T$  modules are 6 links times 2 sector. The signals received from the EI/FI Optical fanout are 4 links. Dual Receiver (M2R-25-4-1-TL, STRATOS Lightwave) is used to reduce the number of optical converters. 6 (for High- $p_T$  modules)+2(for EI/FI) OE/OE converter (Dual Receiver) is used.

**Output signals for MUCTPI:** The signals transmits to the MUCTPI are 32-bit format LVDS signals. The ANSI/SFF-8441 standard 68-pin VHDCI type connectors for each Sector are equipped. Detailed information is described in [16].

**Input signal for TTC distributor:** The signal level for TTC is LVDS. The SLP0 inputs 5 TTC signals (BC(Des1), BCR, ECR, L1A and Reset) from TTC distributor with a 10-pin flat cable connector.

**Input and Output signals for Readout:** Two SLB ASICs are mounted for input and output signals of each Sector Logic Readout. The trigger matrix feature is disabled. The Readout output signals are converted into serialized LVDS signal with LVDS serializer (DS92LV1023TMSA). A JRC (JTAG Routing Circuit, which is used on PS-Board) is also mounted to select both SLB's JTAG path. A RJ-45 connector is equipped to send the serialized data to Star Switch (SSW). The channel assignment is same with PS-Boards.

**G-Link Monitor:** For monitoring G-Link status, we chose a Xilinx Spartan-IIIE FPGA (XC2S50E-PQ208C). This FPGA provides G-Link status registers which can be accessed via VME and "G-Link OK" signals for each Main FPGA.

Figure 4.34 and Figure 4.35 show the layouts for FORWARD Sector Logic and ENDCAP Sector Logic respectively.

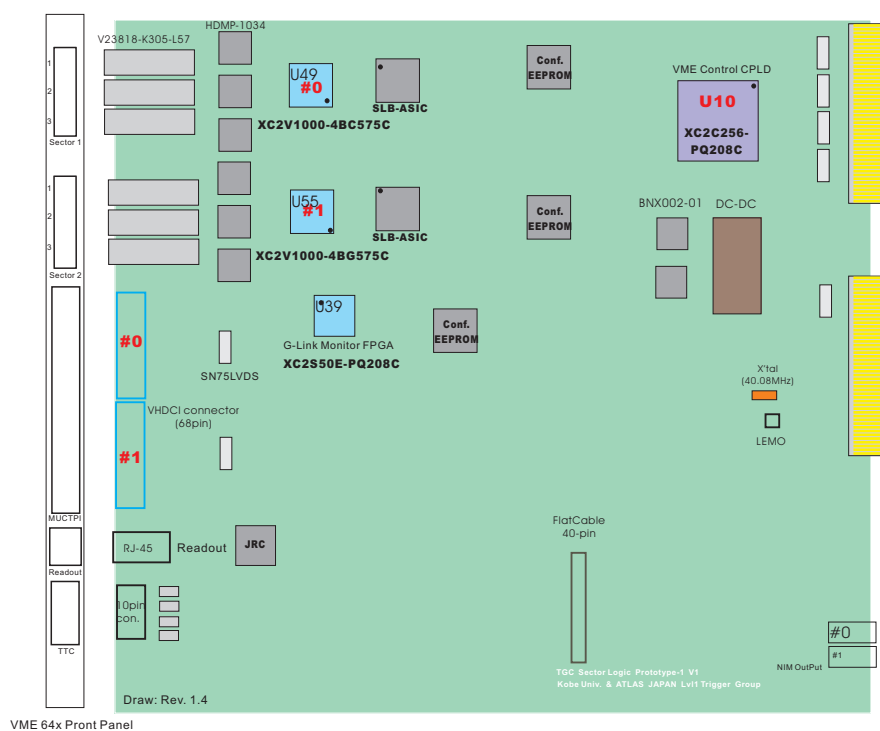


Figure 4.34: The layout of TGC FORWARD Sector Logic (top view).

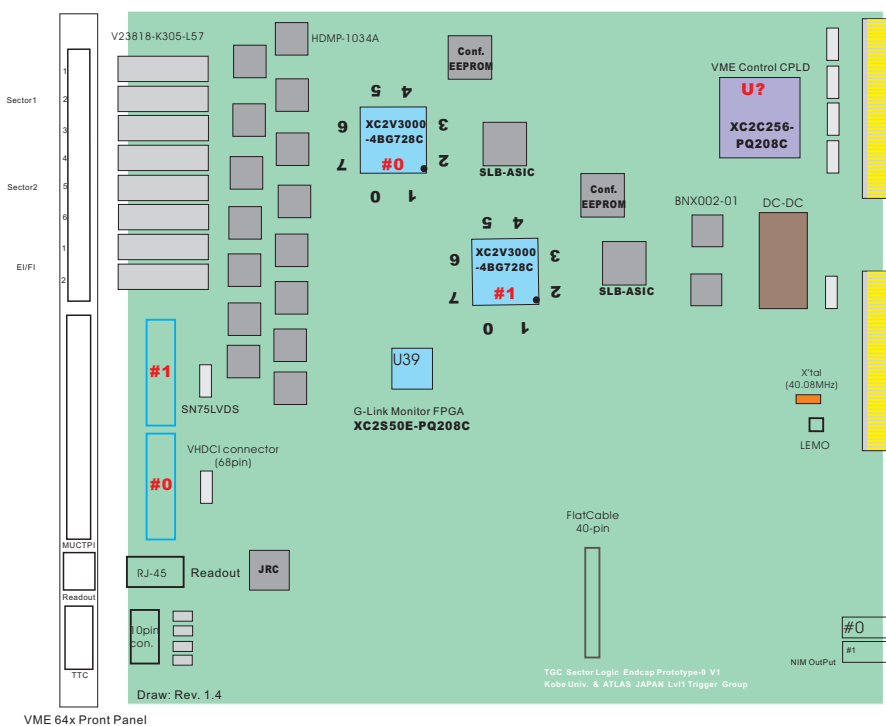


Figure 4.35: The layout of TGC ENDCAP Sector Logic (top view).

## 4.4 Radiation Tolerance

As discussed in Section 4.1, four types of ASICs are extensively used in the on-detector part of the ATLAS Level-1 muon Endcap trigger system. (See Figure 4.2 on page 42.) Anti-Fuse type FPGAs are also used for other components with not a large number of same chip is used. As illustrated on Figure 3.3 on page 37, the ASICs and FPGAs are mounted on boards, which are just behind or outer rims of the TGC wheels.

The region where these electronics (except ASD board location) are mounted will be exposed to the radiation of up to  $\sim 210$  Gy (including a safety factor 70) and a energetic hadron ( $> 20$  MeV) integrated intensity of up to  $\sim 2.1 \times 10^{10}$  hadrons/cm<sup>2</sup> for ten years in the normal operation [12] [14]. All ASICs we made except ASD ASIC <sup>7</sup> and both Anti-Fuse type FPGAs are fabricated in the CMOS process. CMOS process is not sensitive to neutrons in estimated level (up to  $\sim 1.2 \times 10^{12}$  1MeV eq. neutrons/cm<sup>2</sup>, including a safety factor 20) in the on-detector TGC electronics system.

We must clarify all the devices (of ASICs, FPGAs and other Commercial-Off-The-Shelf (COTS)) to survive in this radiation environment with no degradation in performance in terms of total ionizing dose (TID) and single event effects (SEE).

We intend to use four technologies for the chip production; (1) 0.35  $\mu$ m standard full custom CMOS of ROHM, (2) 0.35  $\mu$ m Gate Array CMOS of Hitachi for ASIC productions and (3-4) two Actel Anti-Fuse type FPGAs [38].

In order to validate the devices made with these technologies are applicable in the on-detector TGC electronics system, we have made the irradiation measurements of them using  $\gamma$ -ray from <sup>60</sup>Co for TID and 70 MeV proton beam for SEE.

In this Section, the results of the irradiation tests for chips fabricated with technologies listed above are described. The result of the irradiation test for other COTS are documented in [22].

### 4.4.1 Test for Total Ionization Dose (TID)

#### 4.4.1.1 TID Test Procedure

The  $\gamma$ -ray irradiation facility is two-story structure; an irradiation room on the downstairs and a store with a lead container for the irradiation sources on the upstairs. 48 pencil type rods as radiation sources are filled in a cylindrical vessel, which moves between the upstairs and the downstairs via remote control system. (Figure 4.36 shows the experiment setup.)

The maximum strength of the sources and the maximum dose rate are 22 TBq and 1000 Gy/hr in H<sub>2</sub>O. The irradiation rate can be controlled by changing the radiation source and the location of the DUT (we call hereafter a target chip as DUT; Device Under Test). We used

---

<sup>7</sup>The study of radiation tolerance including neutron irradiation for ASD ASIC had been done [23] [24], hence the ASD ASIC issue does not described in this thesis.

$^{60}\text{Co}$  as the source and the irradiation rate was set at 9.54 Gy(Si)/min. The irradiation facility of RCNST (Research Center for Nuclear Science and Technology) is widely being utilized in University of Tokyo, Japan; the dose rate is periodically calibrated using a Fricke Radiation Meter. The irradiation and the annealing were done at room temperature, around 25 °C. During the irradiation and the annealing, DUTs were biased without clock and the current were monitored. The functionality was checked before and after the irradiation and the annealing.

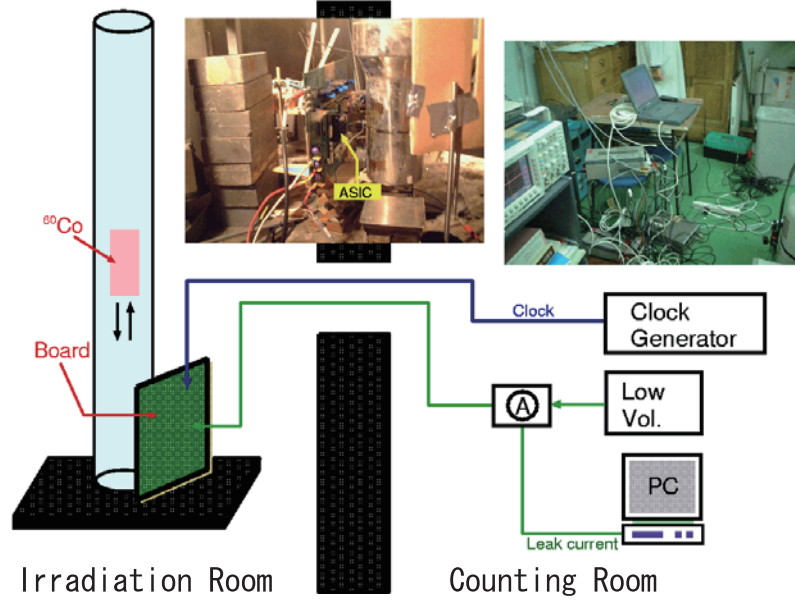


Figure 4.36:  $\gamma$ -ray irradiation test setup.

#### 4.4.1.2 Results of the TID tests

##### 1. CMOS ASIC

We have test four PP ASIC chips. Three chips were irradiated up to 300 Gy, and the other one was irradiated to 850 Gy. Until 300 Gy, we have observed no increase of the static current for all the chips while the current of the fourth one was increased from 49nA to 81nA monotonically as the irradiation level increased from 500 Gy to 850 Gy.

The PLL in a PP ASIC adjusts a voltage (VCON) to hold 25 nsec delay for the variable delay circuit of 32 delay cells. The PLL tried to increase vcon if the response of the delay circuit becomes slower. Otherwise it tried to decrease VCON to keep delay value constant as 25nsec. In Figure 4.37, a VCON plot as a function of irradiation level is shown. The VCON was decreased once and it turned up at around 600 Gy.

In the mean time in order to observe any characteristic change of a circuit in a Rohm 0.35  $\mu\text{m}$  chip caused by the irradiation, we have processed a ring-oscillator circuit in an independent chip with the same technology. The circuit is connected with 501 NAND logics to form a ring to observe the oscillation frequency. We have also irradiated this chip

as the same condition as the one for PP ASIC. Figure 4.38 shows the frequency change with the irradiation. We can find the frequency was increased till 600 Gy, then it was decreased, namely the circuit response became once faster owing to the irradiation, and then it became slower. Comparing with this figure with Figure 4.37, we found correlation. This means that the PLL worked correctly to adjust VCON in order to compensate the variation of the circuit response time due to the irradiation up to 850 Gy where we quitted the test.

The functions of the ICs were measured before, after the irradiation, after the annealing and at the breaks during the irradiations. We could not find any failure in the tests.

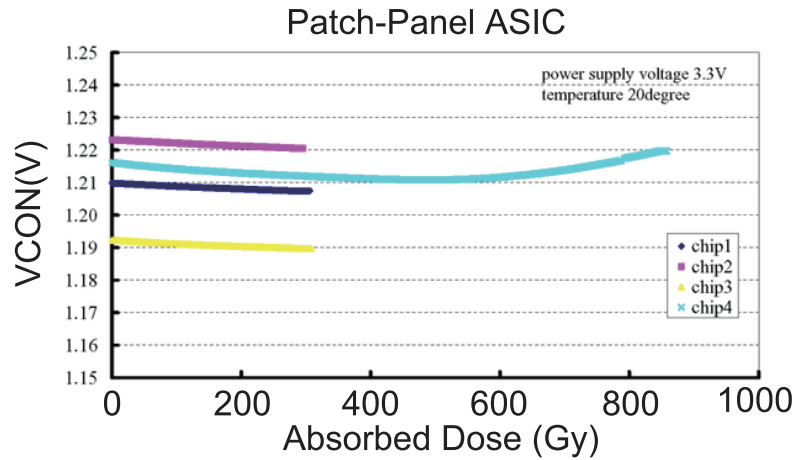


Figure 4.37: VCON voltages of PP ASIC for  $\gamma$ -ray irradiation.

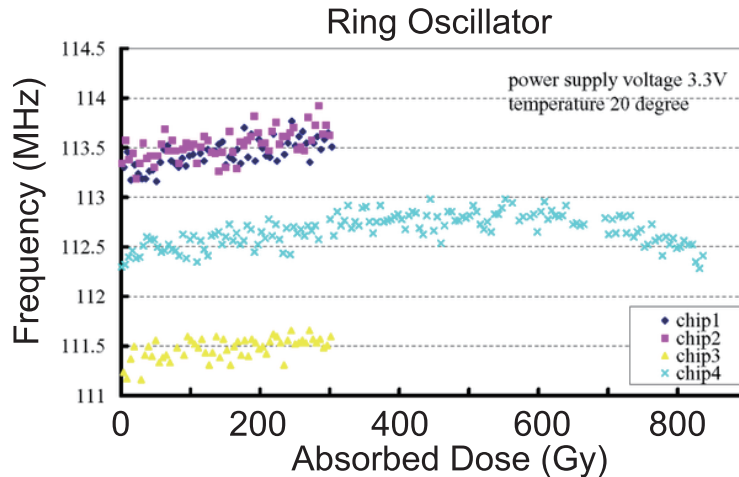


Figure 4.38: Frequencies of Ring Oscillator on Rohm 0.35  $\mu\text{m}$  for  $\gamma$ -ray irradiation.

Three SLB ASICs (0.35  $\mu\text{m}$  Rohm full custom) were sampled in the TID test. Static currents were measured during irradiation.

In the SLB ASIC, the current increased from 2.1 mA to 14.5 mA at the start of the irradiation. The increase of the current due to the integrated dose can be observed at around 150 Gy. At the integrated dose of 200 Gy, we interrupted the irradiation for the function measurement. After the inspection of the chip, the irradiation was resumed up to 430 Gy, where the current monotonously increased to 44 mA. The current went down to 33 mA at the termination of the irradiation. In the annealing of three days, the current gradually decreased to 2 mA. Other two chips were irradiated up to 200 Gy. Behaviours of the current increase were exactly same as the chip mentioned above.

For two High-p<sub>T</sub> ASIC chips, one was irradiated up to 750 Gy. During the irradiation we took two breaks at 200 Gy and 400 Gy for the function inspection of the chip. The increase of the current gradually starts at around 200 Gy and is rapid beyond 300 Gy. Another chip was irradiated up to 200 Gy and showed similar behavior.

The functions of the ICs of SLB and High-p<sub>T</sub> ASIC were measured before, after the irradiation, after annealing and at the breaks during the irradiations. The functions of the Low-p<sub>T</sub> trigger logic in the SLB ASIC and High-p<sub>T</sub> trigger logic in the High-p<sub>T</sub> ASIC were tested. Five test input patterns were fed to the ICs at 40.08 MHz and the outputs were compared with the simulation outputs. We could not find any failure in the tests.

## 2. Actel Anti-Fuse type FPGAs

In on-detector part of the system, two series A54SX-A and Axcelerator of Actel Anti-Fuse type FPGAs are used. A54SX-A will be used in PS-Board and also in the boards installed in the HSC crate while Axcelerator will be used only in SSW board mounted in the HSC crate. Axcelerator is a large scale FPGA and has embedded memories.

In a chip of A54SX-A series (A54SX32A), we have built in a ring oscillator circuit and measured its characteristic behavior in the radiation environment while a four-bit shift register circuit in R-cell and a ring oscillator circuit in C-cell have been built in a Axcelerator chip.

Figure 4.39 shows static currents versus absorbed dose (irradiation) level for four A54SX32A FPGAs. The full (dotted) curves indicate the current with (without) the operation of the ring oscillator circuit. Figure 4.40 indicates frequency dependence on the absorbed dose. From both plots, we found that no significant degradation due to the irradiation was observed up to 600 Gy in A54SX32A chips. Note that we will use them in at most 100 Gy (for ten years) radiation environment.

The static current for four Axcelerator series FPGAs (AX250) versus the absorbed dose is shown in Figure 4.41.<sup>8</sup> In the measurement, the operation of the build-in circuit (a ring oscillator) has been paused for 10 seconds in every one minute regularly. This makes

---

<sup>8</sup>1 krad = 10 Gy

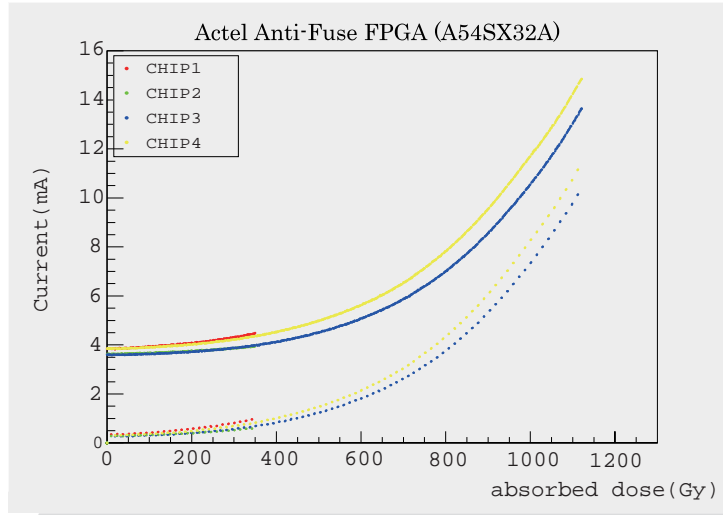


Figure 4.39: Consumption current of A54SX32A for  $\gamma$ -ray irradiation.

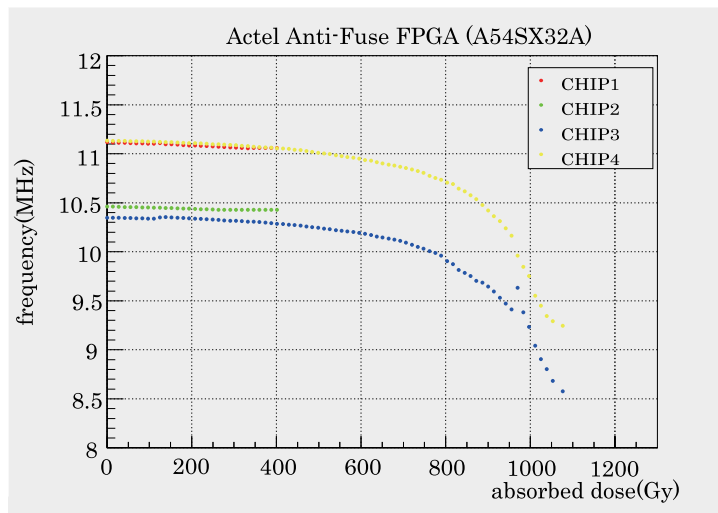


Figure 4.40: Frequencies of Ring Oscillator on A54SX32A for  $\gamma$ -ray irradiation.

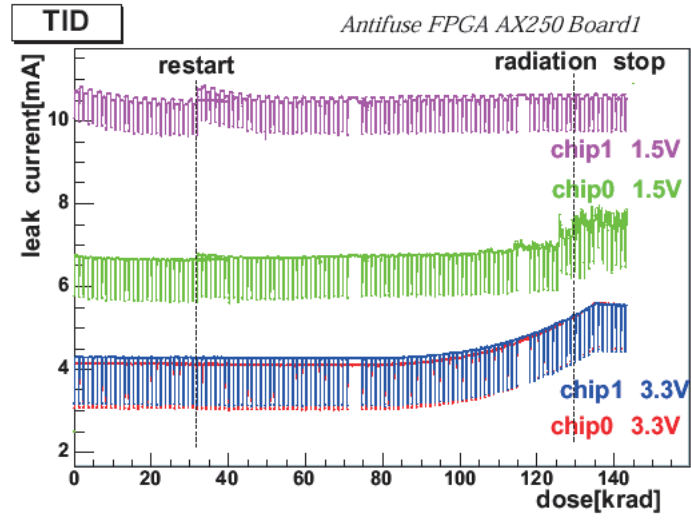


Figure 4.41: Consumption current of AX250 for  $\gamma$ -ray irradiation. (1 krad = 10 Gy)

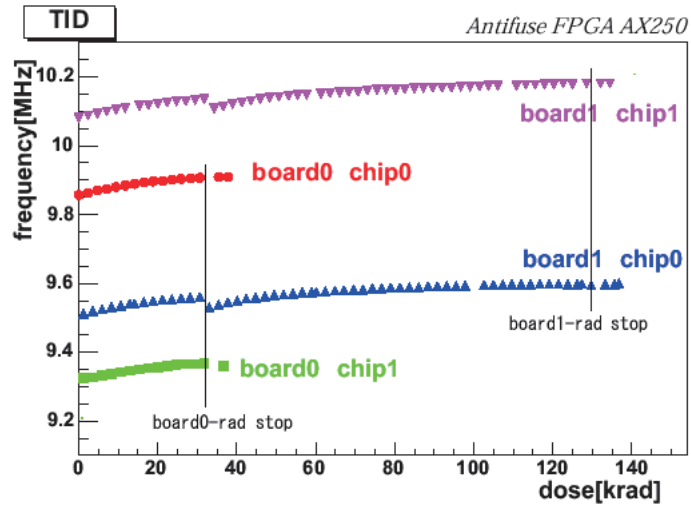


Figure 4.42: Frequencies of Ring Oscillator on AX250 for  $\gamma$ -ray irradiation. (1 krad = 10 Gy)

saw-toothed structure in the graph. The frequency of the ring oscillator versus the dose is shown in Figure 4.40. In the current measurement, we observed two different currents per chip, one is observed in the I/O cell which needs 3.3 V power, and the other one is for the core logic part which is operated with 1.5 V. From both plots, we found that neither significant current increase nor frequency change has been observed for all the four chips tested. Dynamic range of the change for both the leak current and the frequency in the Axcelerator series chips were smaller than one in the SX-A series ones. This may be due to that the Axcelerators were processed with more advanced technology of 0.15  $\mu\text{m}$  CMOS Anti-Fuse than SX-A ones.

#### 4.4.2 Test for Single Event Effect (SEE)

A Soft SEE (Single Event Effect) is phenomenon of radiation induced bit flip (non-permanent) or Single Event Upset (SEU). A hard SEE is also the same as the soft SEE but a destructive SEE produces permanent short circuits in a chip, like a latch-up. Whatever effect is concerned, any SEE rate for a chip can be determined from the SEE test as follows;

$$SEERate = (\sigma_{SEE}) \times N_{bits} \times SRL_{see} \times SF_{sim}$$

where  $\sigma_{SEE}$  is the cross section of either SEU or hard SEE for a chip in the location it will be installed ( $\text{cm}^2/\text{bit}$ ),  $N_{bits}$  is the number of bits affected by SEE,  $SRL_{see}$  is the simulated Radiation Level at the location in a second ( $\text{hadrons}/\text{cm}^2/\text{s}$ ), and  $SF_{sim}$  is the safety factor of the simulation, and is set as '5'.

The maximum value of the  $SRL_{see}$  of the PP ASIC or SLB ASIC is seen on the electronics module at the most inner part of the ATLAS ENDCAP region ( $r=775$  cm and  $z=1250$  cm) and is estimated as  $2.11 \times 10^2$   $\text{hadrons}/\text{cm}^2/\text{s}$  (for hadrons energy  $>20\text{MeV}$ ). The  $SRL_{see}$  for the position where High- $p_T$  ASICs are placed is estimated to be  $1.42 \times 10^2$   $\text{hadrons}/\text{cm}^2/\text{s}$ . These values are taken from a simulation done by the ATLAS radiation hardness assurance group [12] [14].

In order to estimate the SEE rate for any particular chip in a test, we must count occurrence of SEUs for certain amount of time, estimate integrated proton intensity into the chip, and derive  $\sigma_{SEU}$  from them.

For the estimation of the proton intensity for a chip in a test, we made dosimetry measurement for a Cu-foil. Thickness of the Cu foil is 0.125 mm and its purity is 99.99+%.

The size of the Cu-foil is 25 mm  $\times$  25 mm and attached on top of the chip just being tested. After one hour a run of the SEE test,  $\gamma$ -ray spectrum from activated radioisotopes was measured for 1,000 sec with a Ge detector.

We can estimate the number of nucleus generated ( $N$ ) in the irradiation for period  $T_i$  seconds from the number of  $\gamma_s$  observed ( $C_\gamma$ ) in the dosimetry measurement. Then if we know the effective cross section of proton and Cu, and number of Cu atoms in the target, we can

deduce the integrated proton intensity (number of protons/cm<sup>2</sup>). Furthermore, in order to estimate actual integrated proton intensity in the die of a chip ( $F$ ) in the irradiation period, beam profiles were measured. For the beam profile measurement, we exposed the irradiated Cu-foil on an Imaging Plate (IP) [42] after Ge detector measurement, and scan the intensity of the exposed Imaging Plate with a IP Reader (FUJIFILM BAS-1000). The unit of  $F$  is given as proton/cm<sup>2</sup>. Then  $\sigma_{SEU}$  is given with a following relation,

$$\sigma_{SEU} = (\text{number of SEE counted})/F/N_{bits}.$$

#### 4.4.2.1 SEE Test Procedure

For the SEE test, we have used an AVF cyclotron at the Cyclotron and Radioisotope Center (CYRIC) of the Tohoku University, Japan. The Cyclotron was recently upgraded and has maximum proton energy of 90 MeV. 70 MeV proton beam was extracted through a Ti foil of 20 mm $\phi$  and 100  $\mu$ m thickness into air and was impinged to a DUT.

Figure 4.43 and Figure 4.44 shows the experiment setup. A target board and a ZnS fluorescence screen were mounted on an X-Y stage. The beam position was first monitored by the fluorescence screen and then the target board was moved to the beam position (The beam was stopped with a beam stopper during the X-Y stage was moving.). Actual beam profile and beam intensity were measured, individually for each chip with dosimetry of a 100  $\mu$ m thick Cu foil placed in front of the DUT. The beam intensity at the final beam stopper was around 2 - 4 nA. The beam was intentionally broadened up to the size of around 20 mm $\phi$ .

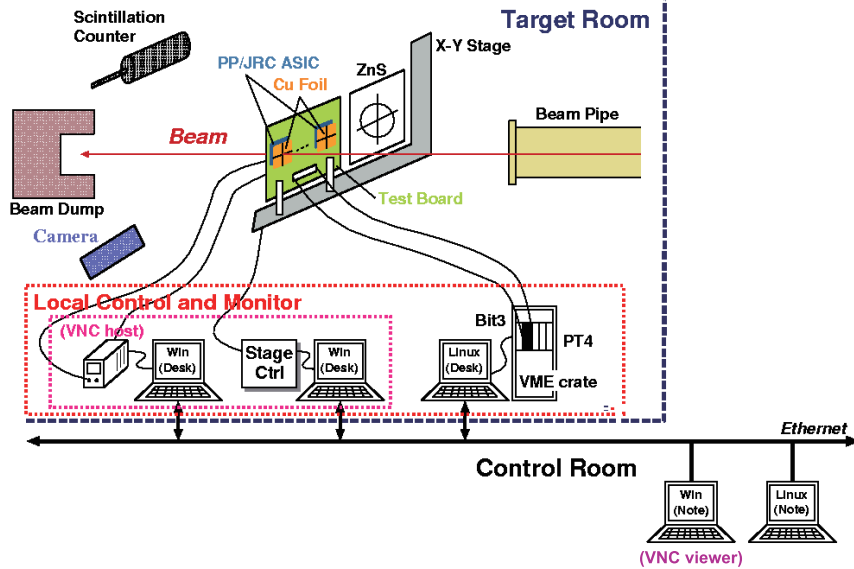


Figure 4.43: Schematic of proton beam test setup.

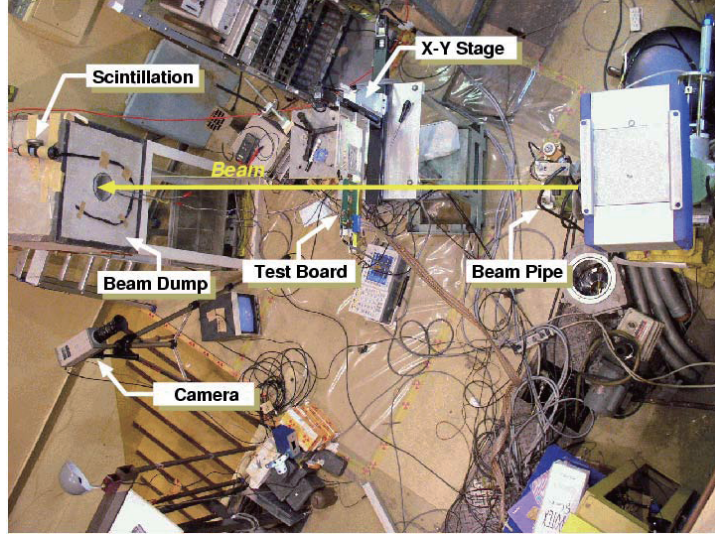


Figure 4.44: Picture of proton beam test setup.

#### 4.4.2.2 SEE cross sections for individual chips

##### 1. CMOS ASIC

We have processed a 4 bit 256 stage shift register into an independent ASIC chip in order to evaluate  $\sigma_{\text{SEU}}$  for Rohm 0.35  $\mu\text{m}$  CMOS ASICs. We have produced four chips of this shift register ASIC for  $\sigma_{\text{SEU}}$  estimation. We then took the value as  $\sigma_{\text{SEU}}$  for PP and SLB ASICs commonly. In the SEE test of this special ASIC, we have observed total 185 times of soft SEE for four chips with  $6.3 \times 10^{12}$  protons/ $\text{cm}^2$  of the total integrated proton intensity injected (i.e. fluence). Thus the  $\sigma_{\text{SEU}}$  is estimated as  $2.8 \times 10^{-14}$   $\text{cm}^2/\text{bit}$ .

In the High- $p_{\text{T}}$  ASIC, because all the registers are implemented by the voting logic circuit, only Boundary-Scan Registers (BSR) were examined by writing arbitrary data and reading/verifying via the JTAG protocol. The number of bits in the BSR observed was 92. The speed of the JTAG clock (TCK) was around 100 kHz. No SEE has been observed with the fluence of  $5.6 \times 10^{12}$  protons/ $\text{cm}^2$ . Then  $\sigma_{\text{SEU}}$  is estimated for High- $p_{\text{T}}$  ASIC as  $< 4.7 \times 10^{-15}$   $\text{cm}^2/\text{bit}$  with 90% confidence level. Even one single event latch-up has been observed neither in Rohm CMOS devices nor Hitachi gate array devices.

##### 2. Actel Anti-Fuse type FPGAs

- SX-A Series

We have installed a four bit shift register of 256 stages (1024 bit), and read and verified the data outputted. No SEE has been observed with the fluence of  $2.6 \times 10^{12}$  protons/ $\text{cm}^2$ .  $\sigma_{\text{SEU}}$  is estimated, therefore, as  $< 1.5 \times 10^{-15}$   $\text{cm}^2/\text{bit}$  with 90% confidence level.

- Axcelerator Series

We have installed a four bit shift register of 345 stages (total 1380 bit). We have applied the SEE test also to the embedded memory whose size is 54 Kbit. Since the memory is configured as dual port memory, regularly we inputted a bit pattern to the memory, and compared it with the output bit pattern from the memory for verification. We have observed 32 SEEs in the R-cell FF and 3869 in the embedded memory with  $1.4 \times 10^{12}$  protons/cm<sup>2</sup> of the proton fluence.  $\sigma_{\text{SEU}}$  for R-cell (Flip-Flop cells in FPGA) is estimated as  $1.6 \times 10^{-14}$  cm<sup>2</sup>/bit, and  $\sigma_{\text{SEU}}$  for the Memory is  $4.9 \times 10^{-14}$  cm<sup>2</sup>/bit.

No single event latch-up has been observed in Actel Anti-Fuse type FPGAs.

#### 4.4.3 Summary of the irradiation tests

From the TID tests, we could conclude that Rohm CMOS 0.35  $\mu\text{m}$  ASICs will work fine for Total absorbed dose of 800 Gy, and Hitachi Gate Array will be fine till 300 Gy where we stopped irradiation. The series SX-A (Axcelerator) of Actel Anti-Fuse type FPGA will work fine till 600 (1000) Gy.

The SEE test results can be summarized in Table 4.3.

Table 4.3: Compilation of the SEE test results.

Technology	Proton fluence (protons/cm <sup>2</sup> )	$\sigma_{\text{SEU}}$ (/cm <sup>2</sup> /bit)
Rohm CMOS 0.35 $\mu\text{m}$	$6.3 \times 10^{12}$	$2.8 \times 10^{-14}$
Hitachi CMOS 0.35 $\mu\text{m}$ Gate Array	$5.3 \times 10^{12}$	$< 4.7 \times 10^{-15}$
Actel FPGA SX-A	$2.6 \times 10^{12}$	$< 1.5 \times 10^{-15}$
Actel FPGA Axcelerator (R-Cell)	$1.4 \times 10^{12}$	$1.6 \times 10^{-14}$
Actel FPGA Axcelerator (Memory)	$1.4 \times 10^{12}$	$4.9 \times 10^{-14}$

## Chapter 5

# Summary and Conclusions

In the ATLAS Experiment, events with important and/or interesting physics processes are buried in a large amount of backgrounds originated from QCD soft collision processes. Event triggering system plays an important role to find out such interesting events, and will be a key for success in the experiment. Since muons exist in the final states of various important physics processes, trigger systems with muon activities is especially important in this experiment.<sup>1</sup>

The author developed two the key devices for the Endcap muon Trigger of the Level-1 Trigger system; TGC Trigger system.

The TGC Trigger electronics is required to handle about  $3 \times 10^5$  chamber signals, to operate in synchronous with 40.08 MHz LHC clock and to have dead-time less architecture (pipe-line processing). To realize the functionalities, various new technologies were tested and introduced to the trigger system. Followings were accomplished in this studies :

1. Development of the front-end circuits with ASICs (Slave Board ASICs) :

In SLB ASIC, five types of low- $p_T$  decision circuits are implemented in one device. It also has pipeline memories to realize dead-time-less data acquisition (pipeline processing) and queuing buffers for signal readout. We implemented the circuits in a custom IC device (Rohm 0.35  $\mu\text{m}$  process with 9.86 mm squared die), where a total number of  $\sim 10^6$  CMOS gates were placed. The author also confirmed the validity of the fabricated ASICs. The ASICs worked with a clock frequency up to 69 MHz (i.e. There is 10.5 ns timing margin at normal 40.08 MHz operation.). The mass-production had done.

2. Development of the  $(R, \phi)$  coordinate integration logic (Sector Logic) :

The Sector Logic integrates  $R$  and  $\phi$  coordinate information and finds muons with high transverse momentum. To remain a flexibility for detection of various types of the physics events, the Look-Up Table (LUT) algorithm is implemented in FPGA (programmable) devices. In the Sector Logic, muons are classified into six groups based on the momentum

---

<sup>1</sup>Note that muons, which punch-through the calorimeters, make signals in the outer tracker devices. Hits in the tracker are important as clean trigger sources rather than the hits observed in the inner tracking systems where a large amount of pile-up is seen.

with the programmable thresholds. The author started from a preliminary designing process of the algorithm, and by completing the design verification, module prototyping for the validity check, then, in final, established the final design for the fabrication. With the prototyping module, the author confirmed that the module worked with a clock frequency up to 54 MHz. It was found that the signal processing worked enough fast and provided 6.5 ns margin at normal 40.08 MHz operation.

### 3. Tests for radiation tolerance :

Electronics systems, which will be installed in the experimental hall, are required to be radiation-tolerant. According the latest ATLAS policy [14], the electronics devices mounted around the TGC should be tolerant to 210 Gy for TID and  $2.1 \times 10^{10}$  hadrons/cm<sup>2</sup> for SEE.

- Tests for total ionization doze (TID) effects; caused by  $\gamma$ -rays :

We measured variations of the characteristics of the ASICs (Rohm 0.35  $\mu$ m CMOS process, Hitachi 0.35  $\mu$ m Gate Array CMOS process) and two Actel Anti-Fuse type FPGAs as a function of total radiation dose. The leakage current does not increase until the radiation exposure of 210 Gy, which is the Radiation Tolerance Criteria (RTC) value. Note that this RTC value contains safety factor 70 to the simulated radiation level in worst case for 10 years operation. And any fatal phenomena were occurred. Hence, it can be concluded that this device can be used for ATLAS Experiment without any TID problem.

- Tests for single event effects (SEE); caused by energetic hadron ( $> 20$  MeV):

We have measured the rates of single event upset (SEU) for the ICs with protons (70 MeV) provided from the AVF-Cyclotron at CYRIC in Tohoku University. The SEU cross-section of Rohm 0.35  $\mu$ m CMOS process measured from this experiment is  $\sigma_{\text{SEU}} = 2.8 \times 10^{-14}$  cm<sup>2</sup>/bit. Since the estimated SEU rate in the whole TGC electronics system is small enough, we can overcome it by introducing the Voting Logic structure.

# Bibliography

- [1] ATLAS Collaboration, “Technical Proposal for a General-Purpose pp Experiment at the Large Hadron Collider at CERN”, CERN/LHCC/94-43, December 15, 1994.
- [2] O.Brüning et. al., “LHC Design Report Volume I The LHC Main Ring”, CERN-2004-003, June 4, 2004.
- [3] The ATLAS and CMS Collaborations, “High Transverse Momentum Physics at the Large Hadron Collider”, BNL-HET-01/33.
- [4] RD12 Collaboration, “RD12 Status Report”, CERN/LHCC/97-29, April 1997.
- [5] ATLAS Collaboration, “ATLAS Detector and Performance Technical Design Report”, CERN/LHCC/99-14,15 (1999)
- [6] ATLAS Collaboration, “ATLAS Level-1 Trigger Technical Design Report”, CERN/LHCC/98-14, June 1998.
- [7] ATLAS Collaboration, “ATLAS Muon Spectrometer Technical Design Report”, CERN/LHCC/97-22, May 1997.
- [8] ATLAS Collaboration, “ATLAS Liquid Argon Calorimeter Technical Design Report”, CERN/LHCC/96-41, December 1996.
- [9] ATLAS Collaboration, “ATLAS Tile Calorimeter Technical Design Report”, CERN/LHCC/96-42, December 1996.
- [10] ATLAS Collaboration, “ATLAS Trigger Performance Status Report”, CERN/LHCC/98-15, June 1998.
- [11] P.Igo-Kemenes, “report to the LEPC”, November 2000.
- [12] O.Sasaki, “Official Radiation Levels and Radiation Tolerance Criteria in TGC Boards”, [http://www-online.kek.jp/~sosamu/radiation/radiationtolerancecriteria\\_tgc.doc](http://www-online.kek.jp/~sosamu/radiation/radiationtolerancecriteria_tgc.doc)
- [13] Level-1 muon trigger group, “Improvement to the Level-1 muon trigger giving increased robustness against backgrounds”, ATLAS-DAQ-99-008 (ATLAS-COM-DAQ-99-

- 011), June 1, 1999.  
[http://atlas.web.cern.ch/Atlas/project/TGC/www/doc/com-daq-99-011\\_ps.gz](http://atlas.web.cern.ch/Atlas/project/TGC/www/doc/com-daq-99-011_ps.gz)
- [14] Radiation Hardness Assurance Working Group, “ATLAS policy on radiation tolerant electronics”, ATLAS working document.  
<http://www.cern.ch/Atlas/GROUPS/FRONTEND/WWW/radtol2.ps>
  - [15] ATLAS Radiation Background Taskforce, “Estimation of Radiation Background, Impact on Detectors, Activation and Shielding Optimization in ATLAS”, ATL-GEN-2005-001, January 13, 2005.  
<http://atlas.web.cern.ch/Atlas/GROUPS/PHYSICS/RADIATION/gen-2005-001-feb05.pdf>
  - [16] Ph.Farthouat, “Interfaces and overlaps in the level-1 muon trigger system, Revision 11”, January 17, 2006. <https://edms.cern.ch/document/114604/5>
  - [17] R.Ichimiya, “HPT Board g-link connection table (rev-12)”, ATL-DA-EN-0002, July 29, 2005, <https://edms.cern.ch/document/700560/>
  - [18] R.Ichimiya et. al., “Sector Logic Implementation for the ATLAS Endcap Level-1 Muon Trigger”, *Proceedings of the Eighth Workshop on Electronics for LHC Experiments, Colmar, France*, 9-13 September 2002, CERN 2002-003, pp. 236-240.
  - [19] R.Ichimiya et. al., “Report on the Integration Test between the Endcap Muon Trigger Sector Logic and the Muon-CTP-Interface”, ATL-DA-TR-0004, January 10, 2002.
  - [20] R.Ichimiya et.al., “Radiation Qualification of Electronics Components used for the ATLAS Level-1 Muon Endcap Trigger System”, *IEEE Transaction on Nuclear Science*, Vol.52, issue 4, August 2005, pp.1061-1066.  
<http://cdsweb.cern.ch/search.py?recid=812814&ln=en>
  - [21] R.Ichimiya et. al., “Irradiation tests of ROHM 0.35um ASIC and Actel Anti-fuse FPGA for the ATLAS Muon Endcap Level-1 Trigger System”, *Proceedings of the Tenth Workshop on Electronics for LHC Experiments, Boston, MA, USA*, 13-17 September, 2004, CERN 2004-010, pp. 117-121.  
<http://cdsweb.cern.ch/search.py?recid=812812&ln=en>
  - [22] R.Ichimiya et. al., “Radiation qualification of Commercial-Off-The-Shelf LVDS and G-link serializers and deserializers for the ATLAS endcap muon level-1 trigger System”, *Proceedings of the Tenth Workshop on Electronics for LHC Experiments, Boston, MA, USA*, 13-17 September 2004, CERN 2004-010, pp. 389-393.  
<http://cdsweb.cern.ch/search.py?recid=812813&ln=en>

- [23] O.Sasaki, “ATLAS Thin Gap Chamber Amplifier-Shaper-Discriminator ICs and ASD Boards”, ASD PRR document, ATL-MT-ER-0001, October, 1999.  
<https://edms.cern.ch/file/325796/1/asd-prr.pdf>
- [24] O.Sasaki and M.Yoshida, “ASD IC for the thin gap chamber in the ATLAS experiment”, *IEEE Transaction on Nuclear Science*, Vol.46 (1999) pp. 1871-1875.
- [25] The TGC Excel Parameter Book.  
<http://atlas.web.cern.ch/Atlas/project/TGC/design/tgc.xls>
- [26] H.Kano et. al., “Custom chips developed for the trigger/readout system of the ATLAS endcap muon chambers”, *Proceedings of the Sixth Workshop on Electronics for LHC Experiments*, Cracow, Poland, 11-15 September 2002, CERN 2000-010, pp. 486-490.
- [27] H.Sakamoto et. al., “Readout system for the ATLAS end cap muon trigger chamber”, Prepared for *7th International Conference on Instrumentation for Colliding Beam Physics (INSTR99)*, Hamamatsu, Japan, 15-19 November, 1999. Published in *Nuclear Instruments and Methods in Physics Research Section A*, Vol.453, Issues 1-2, 11 October 2000, pp. 430-432.
- [28] K.Hasuko et. al., “A remote control system for FPGA-embedded modules in radiation Environments”, *IEEE transactions on Nuclear Science*, vol49 (2002), issue 2, pp. 501-506.
- [29] K.Hasuko et. al., “The first integration test of the ATLAS end-cap muon level1 Trigger system”, Prepared for *IEEE 2002 Nuclear Science Symposium (NSS) and Medical Imaging Conference (MIC) and Symposium on Nuclear Power Systems*, Norfolk, Virginia, 10-16 November 2002. Published in *IEEE Transaction on Nuclear Science*, Vol.50 (2003) pp. 864-868.
- [30] T.Maeno et. al., “Test Beam results on the ATLAS First Level-1 Endcap Muon Trigger System”, Published in *Como 2003, Astroparticle, particle and space physics, detectors and Medical physics applications*, pp. 265-269.
- [31] C.Fukunaga et. al., “Beam test of the ATLAS End-cap Muon Level1 Trigger System”, *Proceedings of the Ninth Workshop on Electronics for LHC Experiments*, Amsterdam Netherlands, Sep. 2003.
- [32] The LVDS (Low Voltage Differential Signaling) Standard, ANSI/TIA/EIA-644.
- [33] National Semiconductor, “LVDS Owner’s Manual and Design Guide”.  
<http://www.national.com/appinfo/lvds/lvdstotal.pdf>
- [34] IEEE, “IEEE Standard Test Access Port and Boundary-Scan Architecture”, IEEE Std. 1149.1-1990.

- [35] IEEE, “Supplement to IEEE Std. 1149.1-1990, IEEE Standard Test Access Port and Boundary-Scan Architecture”, IEEE Std. 1149.1b-1994.
- [36] JTAG Technologies web page, <http://www.jtag.com>
- [37] Xilinx Inc., 2100 Logic Drive San Jose, CA 95124 USA.  
<http://www.xilinx.com/>
- [38] Actel Corporation, Mountain View, CA 94043-4655 USA.  
<http://www.actel.com/>
- [39] A.H.Johnston, “Radiation Damage of Electronic and Optoelectronic Devices in Space”, *Proceedings of the 4th International Workshop on Radiation Effects on Semiconductor Devices for Space Application*.  
[http://parts.jpl.nasa.gov/docs/Dmg\\_Space-00.pdf](http://parts.jpl.nasa.gov/docs/Dmg_Space-00.pdf)
- [40] T.Miyahira and G.Swift, “Evaluation of Radiation Effects in Flash Memories”, *Proceedings of 1998 Military and Aerospace Applications of Programmable Devices and Technologies Conference*.  
<http://klabs.org/richcontent/MAPLDCon98/Abstracts/c4.htm>
- [41] D.R.Roth et. al., “SEU and TID testing of the Samsung 128 Mbit and the Toshiba 256 Mbit Flash memory”, *2000 IEEE Radiation Effect Data Workshop*, pp. 96-99.
- [42] Fuji Photo Film Co., Ltd.  
See [http://home.fujifilm.com/products/science/img\\_plate/img\\_plate.html](http://home.fujifilm.com/products/science/img_plate/img_plate.html)